The Utility of Patient-Specific CT Dose Estimation Maps

Carla M. Thompson

Bachelor of Science in Biomedical Engineering

Marquette University

May 2007

Master of Science in Biomedical Engineering

Wright State University

June 2009

Submitted in partial fulfillment of the requirement for the degree of

DOCTOR OF ENGINEERING IN APPLIED BIOMEDICAL ENGINEERING

at the
CLEVELAND STATE UNIVERSITY

August 2015

We hereby approve the dissertation

of

Carla M. Thompson

Candidate for the Doctor of Engineering degree.

This dissertation has been approved for the Department

of

__ _ Chemical and Biomedical Engineering_____

and CLEVELAND STATE UNIVERSITY
College of Graduate Studies by

____

Sandra S. Halliburton, Chairperson, Dept. of Chemical & Biomedical Engineering

____

Date

____

George Chatzimavroudis, Dept. of Chemical & Biomedical Engineering

____

Date

____

Miron Kaufman, Physics Department

____

Date

____

Frank Dong, Dept. of Chemical & Biomedical Engineering

____

Date

____

Paul Schoenhagen, Dept. of Chemical & Biomedical Engineering

____

Date

____

Student's Date of Defense

This student has fulfilled all requirements for the Doctor of Engineering degree.

____

Dan Simon, Doctoral Program Director

ACKNOWLEDGEMENTS

I wish to acknowledge a few people whose support was critical to my success in completing this dissertation. I would like to express my sincere thanks to my advisor, Dr. Sandra Halliburton, for her expertise, continuous support, and patience with guiding my research and editing manuscripts. I appreciate the time she invested in me because my doctoral studies would not be possible without the opportunity she provided me to study and learn cardiac CT imaging.

A warm thank you is due to my committee members, Dr. Paul Schoenhagen, Dr. George Chatzimavroudis, Dr. Frank Dong, and Dr. Miron Kaufman for helping me with their insightful comments and guidance. A special thanks to Dr. Schoenhagen for helping me with organ segmentation and providing valuable input for my manuscripts. Thank you, Dr. Chatzimavroudis for agreeing to stay on my committee despite your demanding administrative commitment.

I would like to thank Philips Healthcare, Cleveland, Ohio for providing financial assistance for this research. I am grateful to Dr. Jens Wiegert and Dr. Jeffrey Yanof for their stimulating conversation and guidance. I appreciate all the assistance Tom Ivanc provided as well. I would like to thank current and pass CT technologists: Stacie Kuzmiak, Mike Kral, and Julia Hart for their knowledge and patience in answering my countless questions and helping me with phantom scans. My gratitude also extends to my previous lab mates, Xiaopeng, Uma, and Mitya for their helpful advice, thoughtful discussions on CT imaging and the fun times. A special thanks to MRI technologist, Angel Houston for being a kind friend, providing encouraging words and tremendous support during the critical stages of completing my dissertation. Many thanks to Dr. Michael Bolen, for our fun off-topic conversations!

I would like to thank the friends I've made in Cleveland especially Sahadeo, Tony, Johnny, Travis and Ramone. The friendship, support, and countless hours of laughter and good times you provided really helped to balance out the long nights at the clinic to keep me grounded.

To my very close and dearest friends, Astin Hayes and DeAngelo Trotter who have been there to help, listen to me vent, guide, and provide the encouragement that I needed to finish my dissertation! Thank you!

I especially thank my family for their unconditional love and support. A special thanks to my father, Charles Thompson for igniting my STEM interest in high school. Biomedical Engineering has truly been a perfect fit for me. I appreciate all of the encouraging words from Father Thompson and especially my Aunt, Allie Thompson who always checks to see if I need anything. Thank you!!

Lastly, I am very thankful for the church community at New Community Bible Fellowship I joined while working on my doctoral degree. The life group and bible fellowship classes have been instrumental in helping me deal with obstacles and challenging personalities that I had to encounter while working on my degree. This chapter of my life has certainly allowed me to grow closer to God.

The Utility of Patient-Specific CT Dose Estimation Map

Carla M. Thompson

ABSTRACT

Publicized radiation overdoses in computed tomography (CT) imaging sparked concern for the amount of radiation patients receive from CT examinations. Limitations exist with accurately estimating patient radiation dose from CT. However, traditional dose descriptors do not take into account patient-specific anatomy and are therefore limited in providing accurate dose estimates for individual patients. This dissertation describes the development and validation of patient-specific dose maps which display pixel values equal to the dose absorbed by corresponding tissue voxels and the potential utility of dose maps over standard dose estimation methods.

Patient-specific virtual phantoms were created from the patient's own CT images by classifying each voxel as a specific material type based on fixed Hounsfield Unit threshold values. Using a customized Monte Carlo (MC) tool; x-ray photon interactions with the materials were modeled based on specific scanner characteristics.

Dose maps were validated by comparing radiation dose measurements from metal-oxide semiconductor field-effect transistors (MOSFETs) placed in anthropomorphic phantoms during CT scanning to simulate dose map dose values. Results showed that radiation dose estimated using MC methods were strongly correlated with MOSFET measurements.

Dose maps were created from the CT images of 21 obese patients referred for the evaluation of cardiovascular disease. Effective dose (E) determined from the standard dose-length product conversion method was compared to E determined from dose maps using International Commission of Radiological Protection publication 60. Dose maps derived from patient CT images yielded lower E estimates than DLP conversion methods.

The influence of iodinated contrast, routinely injected prior to CT data acquisition, on absorbed radiation dose was explored in a separate patient cohort. Dose maps were created to compare organ doses with CT image acquisition before and after intravenous contrast media administration. Results showed that absorbed radiation dose from CT scanning was higher in the presence of contrast.

This work demonstrated that dose maps provide more accurate dose estimates that account for patient size, individual organ sizes, differences in body composition, and the presence of iodinated contrast. Wide-spread availability of simulation tools for all scanner platforms would enable more patient-specific dose estimation than traditional, patient-generic metrics.

TABLE OF CONTENTS

LIST OF TABLES

Table **Page**

LIST OF FIGURES

CHAPTER I

INTRODUCTION

Although millions of people have benefited from computed tomography (CT) exams, the risk from radiation exposure is a concern especially when radiosensitive organs like the breast and lungs are in the scan range [1]. Accurate estimation of radiation dose to patients during CT scanning is currently limited. Traditional methods for estimating dose are plagued with inherent errors stemming from the use of physical, cylindrical phantoms to represent patients during actual CT scanning. Sophisticated Monte Carlo (MC) methods have been used to combat the limitations of physical phantoms by modelling computational phantoms that better represent the human body. However, a 70 kg reference computational phantom is typically used which does not represent all patients well. Radiation dose to a specific patient will be either over- or underestimated for those individuals whose body size differs from the reference size phantom.

Differences in overall patient size, individual organ sizes, and body composition should be considered to help improve the accuracy of dose estimation methods. The American Association of Physicists in Medicine (AAPM) attempts to address this need by suggesting patient size-based modification of scanner-provided volume CT dose index ($CTDI_{vol}$) values [2]. The report provided correction factors based on a patient's estimated effective diameter that can be used to determine a size-specific dose estimate (SSDE) [2].

Patient-specific 3D anatomical dose maps have the potential to provide more accurate organ dose and effective dose (E) estimates. Patient-specific dose maps capture the variations in human anatomy and body size. Anatomical dose maps are generated by performing MC simulations on virtual phantoms created from patient CT data rather than a standard reference phantom or anthropomorphic phantom. CT radiation exposure can be simulated for a specific patient and scan protocol.

In addition to neglecting patient-specificity, dose descriptors (CTDI, SSDE, dose-length product (DLP), E derived from the DLP conversion method ($E_{DLP)}$) also fail to account for the effect of iodinated contrast on organ dose. The effect of the presence of iodinated contrast agent in the vessels during scanning on radiation dose to the organs is not well understood. Additional radiation could be absorbed by blood due to the increased attenuation of x-rays by iodine thereby sparing dose to the organs. Alternatively, the increased attenuation of x-rays by blood could lead to increased energy deposits in the organs. The extent of iodine uptake by the organs at the time of scanning also influences radiation dose [3, 4].

The goal of this work is to explore the utility of patient-specific cardiovascular CT dose maps. Specific Aim 1: To evaluate the hypothesis that MC methods performed on CT images of an anthropomorphic phantom can accurately estimate organ dose to the phantom. Specific Aim 2a: To evaluate the hypothesis that patient-specific CT dose maps characterize variability in breast and lung dose of obese patients. Specific Aim 2b: To evaluate the hypothesis that CT E is overestimated for obese patients when standard dose estimation methods are employed. Specific Aim 3: To evaluate the hypothesis that dose maps have the ability to quantify radiation dose in the presence of iodinated contrast.

This dissertation is organized as background (chapters 2-7), preliminary work (chapter 8) and the results of specific aims (chapter 9-11). Chapter II explains the formation of x-rays and x-ray interactions. Chapter III introduces computed tomography along with data acquisition and the components of image reconstruction. Chapter IV describes standard dose descriptors used in a clinical setting. The types of computational phantoms are explained in chapter V. Three types of dose detectors are discussed in chapter VI. Chapter VII introduces Monte Carlo methods and highlights three types of Monte-Carlo based dose calculators.

Chapter VIII describes the details of the preliminary studies to validate MOSFET technology and compute calibration factors for eventual validation of dose maps. This chapter also presents initial work on the creation and characterization of dose maps. Segmentation of organs and evaluation of breast and lung dose is also discussed. Finally, the determination of E from dose maps is described in detail and initial comparisons to E derived using traditional methods are made.

Chapter IX describes the validation process of dose maps using metal-oxide semiconductor field resistor transistors (MOSFET) technology. The experimental methods, results, and discussion based on the findings are included in this chapter.

Chapter X describes the utility of patient-specific dose maps by characterizing the variability in breast and lung dose of obese patients and the examination of calculating E for obese patient using both the dose map method and standard dose estimation methods.

Chapter XI explores how radiation dose to a patient is affected by the injection of iodine-based contrast media. A new classification scheme that increases the sensitivity of dose maps to the amount of contrast agent present during scanning is described. The methods, experiments, and preliminary results from a comparison study of the radiation dose patients received during non-contrast and contrast-enhanced scans are detailed in this chapter.

This dissertation concludes with a brief summary of the findings and relevance to dose estimation methods using patient-specific dose maps.

CHAPTER II

X-RAY BASICS

2.1 Radiation

Radiation is energy in motion capable of traveling through space or matter. Electromagnetic (EM) radiation is a type of radiation used in diagnostic imaging. X-rays are a form of EM radiation, produced outside of the nucleus [5]. Nonionizing radiation carries low energy (visible light, radio waves, and microwaves) that can excite electrons to a higher energy state without displacing them [6]. Ionizing radiation carries high energy (ultraviolet, x-rays, and gamma rays) that are capable of removing an orbital electron from an atom. This type of radiation can potentially alter deoxyribonucleic acid (DNA).

2.1.1 Creation of X-rays

Inside of an enclosed vacuum, x-rays are produced when a high voltage is applied between two electrodes (cathode and anode). The acceleration of electrons from the cathode (negatively charged) to the anode (positively charged) is due to the electrical potential difference. Tungsten is a popular anode material because of its high atomic number and high melting point which allows efficient x-ray production [5]. This material can also handle high amount of deposited heat. When electrons hit the target material, the majority of kinetic energy (KE) of the electrons is converted into heat and a small percentage is converted into x-rays [5]. Depending on the chosen target material, the electron shell that exist around the nucleus corresponds to different energy levels (K shell, L shell, and M shell) [5, 6]. The target material with a high atomic number increases the probability of electron interactions to produce higher energy x-rays [5]. Therefore the chosen target material will determine energy of the x-rays produced.

2.1.1.1 Tube Potential

Tube potential, in units of kilovoltage (kVp), is the electrical potential difference applied between the cathode (source) and anode (target) in an x-ray tube allowing the flow of electrons from the source to the target. Tube potential determines the energy of the x-ray beam. Therefore, increasing the tube potential also increases the energy of x-rays which allows for easier penetration of tissues and a reduction of noise in the image. Increasing the tube potential also increases radiation dose; dose is proportional to the square of the tube potential [7]. A selection of discrete tube potentials available on a CT scanner includes these typical values: 70, 80, 100, 120, and 135.

2.1.1.2 Tube Current

Tube current, in units of milliampere (mA), is the number of electrons flowing from the cathode to the anode per unit of time. The product of tube current and x-ray on time is the tube current-time product expressed in unis of millimpere-seconds (mAs). Tube current and tube current-time product are directly related to the amount of radiation delivered to a patient. By lowering the tube current (keeping other parameters constant) radiation dose will be decreased but noise will increase since fewer x-rays will be produced and reach the detector.

2.2 Generation of X-rays

X-rays are generated through two electron interactions processes: bremsstrahlung radiation and characteristic radiation.

2.2.1 Bremsttrahlung Radiation

Bremsttrahlung radiation is characterized as a series of electron interactions with the atomic nucleus of the target material. Most x-rays are created by this method. The Coulombic attraction between the nucleus and the electron causes the electron to decelerate and change direction [5]. A close interaction will yield a higher energy x-ray whereas an interaction at a greater distance from the nucleus will yield lower energy x-rays. High energy x-rays are the result of the electron directly striking the nucleus and a loss of electron's KE. A large distance from the electron to nucleus results in a weak Coulombic force, hence a low energy x-ray. Coulombic forces acting on the electron increases when the distance to the nucleus is close causing a shift in the electron's direction and producing a higher energy x-ray (larger loss of KE) [5]. When multiple electrons undergo Bremsstrahlung interactions, the result is a continuous spectrum of x-ray energies.

The majority of the x-rays produced in Bremsstrahlung are low energy x-rays because the majority of interactions take place at a greater distance from the target nucleus. The unfiltered Bremsstrahlung spectrum shows a linear decrease in the production of x-rays with increasing energy up to a maximum energy determined by the peak tube potential applied to accelerate electrons toward the target. The lowest energy x-rays and the average x-ray energy varies from one-third to one-half of the maximum x-ray energy [5].

2.2.2 Characteristic Radiation

Characteristic radiation occurs when an accelerated electron causes the removal of an electron (ionization) from the K shell (innermost shell). This causes a vacancy that has to be filled from an electron residing in another shell (L or M) because an unfilled shell is unstable. Each electron in the target atom has a binding energy that depends on the shell in which it resides. The K shell (closest to the nucleus) has the highest binding energy followed by L, M and so forth. The chosen target material will determine the specific electron binding energies of the electron shell, hence the emitted x-rays will have discrete energies characteristic of the anode material [5, 6]. Excess energy is released as a characteristic x-ray when the electron moves to a lower energy level. This process results in production of an x-ray photon with energy equal to the difference between the two electron shells [5, 6].

As electrons move from higher to lower energy levels to fill a vacancy, several discrete energy peaks are superimposed on the continuous Bremsstrahlung spectrum. The energy level that receives the electron is designated by a characteristic x-ray with a subscript alpha (α) or beta (β) where α indicates adjacent transition and β indicates a nonadjacent transition [5]. For example, Kα implies that the electron moved from L to the K shell and Kβ implies that the electron moved from M, N, or O shell to K shell [5].

Characteristic K x-rays are emitted only when the electrons colliding with the target exceed the binding energy of a K shell electron. The tungsten target produces a K characteristic x-ray when the acceleration potential is greater than 69.5 kVp [5]. Characteristic x-ray production is described as an electron-electron interaction whereas Bremsstrahlung is an atom-electron interaction.

2.3 X-ray Interaction with Matter

X-rays interact with matter in three primary ways: Rayleigh scattering, Compton scattering, and photoelectric absorption. These interactions will determine the path of the x-ray photon.

2.3.1 Rayleigh Scattering

Rayleigh scattering occurs mainly when very low energy x-rays interact with and excite the total atom causing electrons to vibrate in phase. The lower energy electron returns to its previous energy level by emitting a photon of the same energy but in a slightly different direction. In this interaction, no absorption of energy occurs (ionization does not occur) and the majority of the x-ray photons are scattered at a small angle [5, 8]. The probability of this type of scattering occurring is low, about 5% because of the low effective atomic number of soft tissues [8]. The probability increases as the atomic number increases and the x-ray energy decreases.

2.3.2 Compton Scattering

Compton scattering occurs when a high energy incident photon (E_O) causes the ejection of valence electron from the outer orbital shell and the electron is scattered with some energy (E_{e-}). Simultaneously, a photon is scattered (Esc) with reduced energy. The conservation of energy is preserved when the energy of the incident photon is distributed as the sum of KE of the ejected electron and the energy of scattered photon [5].

$$E_O = E_{e-} + Esc \tag{2-1}$$

Momentum is also conserved in this collision and it can be shown that the wavelength of the scattered photon (λ′) is related to the wavelength of the incident photon (λ), where m_e is the mass of the electron and h is Planck's constant.

$$\lambda' - \lambda = \frac{h}{m_e c}(1 - cos\ \theta) \tag{2-2}$$

$$\lambda_{Comptom} = \frac{h}{m_e c} = 2.4x10^{-12}\, m \tag{2-3}$$

Therefore, this type of scattering results in the ionization of the atom and the loss of KE via excitation and removal of electron. An increase in energy of the incident photon will increase the scattering of both the scattered photon and electron. The majority of the energy is transferred to the scattered electron when high energy incident photons interact with a valence electron. At most diagnostic photon energies, Compton will dominate in materials of lower atomic number such as soft tissue and air.

2.3.3 Photoelectric Effect

Photoelectric effect occurs when the incident photon energy is transferred to an inner shell electron resulting in the ejection of an electron (Ee-) where KE is equal to difference of the incident photon energy (E_O) and the electron binding energy (E_b). The inner shell electron has a binding energy similar to but less than the energy of the incident photon [5, 8].

$$E_e = E_O - E_b \tag{2-4}$$

The ionization of the atom creates a vacancy in which an electron from a higher energy level fills the lower level vacancy but creates another vacancy in the process. This vacancy is also filled from another higher binding energy shell. This process leads to an electron cascade where electrons transition between different energy shells. The result of a photoelectric interaction is the production of a photoelectron, positively charged ion (atom lacks an electron), and characteristic x-rays from lower energies [8]. An increase in the photon's energy decreases the probability of photoelectric effect occurring. Image contrast is improved with photoelectric interaction because the process amplifies differences in attenuation between tissues with different atomic numbers [5, 8]. For example, this process dominates when lower energy photon (i.e., tissue) interact with high atomic (Z) materials (i.e., iodine).

2.4 Attenuation

Attenuation is the removal of photons from an x-ray beam as it passes through matter. This is due to absorption and scattering of photons.

2.4.1 Linear Attenuation Coefficient

Linear attenuation coefficient (μ) is defined by the portion of photons removed from a monoenergetic beam of x-rays per unit thickness of a material expressed in units of (cm^{-1}). An exponential relationship exists between the number of incident photons (N_0) and those that are transmitted (N) through a thickness of material (x) for a monoenergetic beam of photons:

$$N = N_0 e^{-\mu x} \tag{2-5}$$

The linear attenuation coefficient is the sum of the individual linear attenuation coefficients based on different type of interactions of x-rays with matter:

$$\mu = \mu_{\text{Rayleigh}} + \mu_{\text{Photoelectric effect}} + \mu_{\text{Compton scatter}} + \mu_{\text{pair production}} \quad (2\text{-}6)$$

The linear attenuation coefficient is dependent on the incident x-rays that is traveling through the thickness of a material and the density of the material [5, 8].

2.4.2 Mass Attenuation Coefficient

Mass attenuation coefficient is defined as the linear attenuation coefficient per density (ρ) expressed as (μ/ρ). Mass attenuation coefficient is independent of density of the material. The linear attenuation coefficient varies for the same material if it has different physical densities whereas; the mass attenuation coefficient stays the same for a material in different states. [8]. For example, water, vapor, and ice have the same mass attenuation coefficient because it normalizes the linear attenuation coefficient by the density of the material [8].

CHAPTER III

Computed Tomography Basics

3.1 Computed Tomography

Computed tomography (CT) is one of the medical imaging modalities that require ionizing radiation to image patients. An x-ray source and detector rotate around the patient generating cross-sectional images. The rotating x-ray tube allows for multiple x-ray projections taken at different angles. Each table position allows a different slice of tissue in the path of the x-ray beam to be captured for acquisition.

Multi-detector row CT (MDCT) scanners have multiple detector rows in the longitudinal (z-axis) direction enabling acquisition of multiple images with a single gantry rotation. The most modern scanners have 64, 128, 256, or 320 detector rows.

3.1.1 Data Acquisition

MDCT data are acquired with either a sequential (axial or step-and-shoot) or spiral (helical) scanning mode. In axial mode, the gantry rotates around the patient (360 degrees) while the patient table is stationary and then the patient table is incremented (in z-direction) to the next position. This process is repeated until the entire anatomy of interest is scanned.

In helical mode, the gantry continuously rotates around the patient with simultaneous movement of the patient table. The creation of slip ring technology allowed continuous rotation without having to stop gantry rotation. During helical scanning, attenuated photons pass through any given slice of the patient's body striking each detector row in succession as the patient table moves through the gantry. Pitch is only associated with helical scanning and it is defined as the ratio of table travel (mm) per gantry rotation to total nominal beam width (mm) [9]. An increase in pitch (1>) will result in less overlap in data acquisition in the z-direction, whereas a decrease in pitch (<1) will results in more overlap in data acquisition [9].

3.1.2 Image Reconstruction

Attenuation is the removal of photons from an x-ray beam due to absorption and scattering of photons. Each attenuated x-ray that is acquired in CT travels through the patient along a line between the source and the detector. The detector measures the x-ray intensity (I) from each attenuated and unattenuated x-ray. The intensity of x-rays that are unattenuated, I_o, are measured by a reference detector and the following equation shows the relationship between I and I_o:

$$I = I_o\, e^{-\mu x} \tag{3-1}$$

where x is the thickness of the patient along the ray (in centimeters) and μ is the average linear attenuation coefficient along the ray (in cm^{-1}). This data is used to calculate the projection data, P(x) which is independent of the intensity of the x-ray beam.

$$P(x) = \ln\left(\frac{I_o}{I}\right) \qquad (3\text{-}2)$$

Combined results characterized as

$$l\text{n}\ (I_o/I) = \mu x \qquad (3\text{-}3)$$

$$P(x) = \mu x \qquad (3\text{-}4)$$

Taking the logarithm provides a signal that is linearly related to the characteristic of the material being measured. X-rays decrease in intensity exponentially as they pass through material. The linear attenuation coefficient is determined by composition and density of the tissue inside of each voxel in the patient and is the total attenuation coefficient for each x-ray summarized as

$$\mu x = \mu_1\Delta x + \mu_2\Delta x + \mu_3\Delta x + \ldots + \mu_n\Delta x \qquad (3\text{-}5)$$

where Δx is the small path length, which factors out from the above equation:

$$\mu x = \mu_1 + \mu_2 + \mu_3 + \ldots + \mu_n \qquad (3\text{-}6)$$

The reconstructed value in each pixel is the linear attenuation coefficient for the corresponding voxel where μx is the sum of attenuation coefficients μ_j of all materials along a single x-ray.

3.1.2.1 Filtered Back Projection

After preprocessing of the raw data, a CT reconstruction algorithm is used to produce CT images. Back projection (BP) is the most widely used reconstruction algorithm in clinical CT scanners. BP utilizes a mathematical process to reverse the image acquisition by smearing each projection back across the reconstructed image. The algorithm knows the acquisition angle and position in the detector array corresponding to each ray. This process produces blurred images and the data requires a filter before reconstruction. Filtering is used during the image reconstruction process. The process of using a filter to correct for blurring before reconstruction is known as filtered back projection (FBP). Different filters can be applied depending on the diagnostic purpose. A smooth filter is helpful for viewing soft tissues and a sharp filter is ideal for higher attenuating tissues.

Fourier Transform (FT) converts projection data in the spatial domain into the frequency domain. Frequency domain data is multiplied by a filter function (K(f)) and then transformed back into the spatial domain using the Inverse Fourier transform (FT^{-1}). This relationship is represented as

$$p'(x) = FT^{-1}\,[FT[p(x) * K(f)]] \qquad (3\text{-}7)$$

where p(x) is the unfiltered data in the spatial domain and p'(x) is the filtered data in spatial domain. Once the data is filtered, it is ready to be backprojected allowing for recreation of the object scanned. An image matrix is obtained of the scanned volume and a numerical value (between 0 and 1) is assigned to each pixel in the image. This value indicates the average of all the attenuation values contained within the corresponding tissue voxel.

3.1.2.2 Iterative Reconstruction

Iterative reconstruction (IR) is an increasingly prevalent CT image reconstruction method that assumes an initial attenuation coefficient for all voxels and uses these coefficients to predict projection data. This predicted projection data is compared with the actual measured data and an updated image is computed. Voxel attenuation values are repeatedly modified until the error between the estimated and measured projection data is acceptable. This method is more computationally intensive but has been shown to significantly improve image quality in comparison to FBP at a given radiation dose.

3.1.3 Image Display

After CT reconstruction, pixel values are scaled to an integer (see equation below) and compared to the attenuation coefficient of water [5]. The CT number of a material is the end result in clinical CT images. The attenuation coefficient (µ) values are scaled to that of water to compute the CT number and multiplied by a scalar. When the scalar is equal to 1000, the CT Number is called a Hounsfield Unit (HU).

$$Hounsfield\ Unit = \frac{\mu_{tissue-}\ \mu_{water}}{\mu_{water}} \times 1000 \qquad (3\text{-}8)$$

The range of Hounsfield Units is from +1000 to -1000 for naturally occurring tissues in the body (Table 1) [10] . Hounsfield Units are represented on a gray scale [11]. Bone is represented by the brightest white color and air is represented by black while tissues in between are assigned various shades of gray.

Tissue Type	HU
Bone	1000
Soft Tissue	5 to 40
Blood	50 to 60
Water	0
Fat	-200 to -5
Lung	-930 to -200
Air	-1000

Table 3.1: Various tissues are represented by attenuation in HU.

The appearance of the image can vary by modifying the window width (WW) and window level (WL). WW defines the range of grayscale values over which the CT numbers are spread. The WL defines the center of the range of grayscale values.

Changing the WW affects image contrast and changing the WL affects the brightness/darkness of an image [11]. Increasing the WW spreads image CT numbers over a larger range of grayscale values producing an image with highlighted bony structures but poor tissue differentiation. Decreasing the WW increases the image contrast among tissues. The choices of WW and WL will depend on the clinical need.

3.1.4 ECG Synchronization with CT

Electrocardiographic (ECG) synchronization is necessary for most cardiac CT scanning to restrict image data to a desired cardiac phase and is accomplished by using the patient's ECG signal to either prospectively trigger data acquisition or retrospectively gate image reconstruction [9, 12]. A slower heart rate allows a longer diastolic window of minimal cardiac motion avoiding motion artifacts and improving image quality which is important when examining small structures (coronary arteries). Standard CT image reconstruction algorithms require 360 degrees of projection data to generate images. Special algorithms exist for cardiac imaging requiring only approximately 180 degrees of projection data. This means cardiac data can be acquired in less time yielding images with better temporal resolution.

Prospective ECG-triggered axial scanning is often used for cardiac imaging. The patient's ECG signal is synchronized with data acquisition. Detection of the R peak of the ECG signal initiates scanning while the table is stationary, then the table is moved to the next z-axis position while x-ray emission is stopped; data acquisition is resumed once the table is stationary [9, 12]. This process of table movement/data acquisition is repeated until the area of interest is scanned.

Retrospective ECG-gated helical scanning is a higher dose approach in comparison to prospective ECG-triggered axial scanning but preferred for patients with high or irregular heart rates. The patient's ECG signal is simultaneously recorded as data is acquired throughout the cardiac cycle with continuous rotation of the gantry and table movement until the entire scan length is covered [9, 12]. This allows reconstruction of overlapping images at arbitrary z-positions during any heart phase. CT data is retrospectively referenced to the recorded ECG signal and images are reconstructed at desired time points within each cardiac cycle [9, 12]. This technique has an increase in radiation dose because of a requirement for low pitch imaging (slow table movement).

3.1.5 Contrast Administration with CT

Most CT imaging protocols require intravenous iodinated contrast agents to enhance cardiovascular tissues and organs. These water-soluble agents are iodine-based soluble compounds with low toxicity, which are classified as ionic or non-ionic compounds [13]. The use of iodine (atomic number = 53) enhances x-ray attenuation [5]. The high atomic number of iodine allows for greater absorption and scattering of x-rays [13, 14].

Iodine can accumulate in tissues and organs at different concentrations when injected in the body. Contrast enhancement is directly related to the amount of iodine and the x-ray energy (governed by the peak tube potential) [14]. A lower potential results in a stronger contrast enhancement per iodine concentration. The radiation dose absorbed by an organ is dependent on the quantity of iodine accumulated in the organ at the time of scan, organ shape, organ volume, and organ position inside of the body [3, 4].

CHAPTER IV

CT DOSE DESCRIPTORS

4.1 Dose Descriptors

There are four types of dose descriptors that are used to estimate dose: volumetric computed tomography dose index ($CTDI_{vol}$), dose-length product (DLP), effective dose (E), and size-specific dose estimate (SSDE).

4.1.1 Computed Tomography Dose Index

Most clinical CT exams involve multiple gantry rotations. As the x-ray source rotates, dose to the irradiated volume is accumulated dose from adjacent scans [15]. Multiple scan average dose (MSAD) is the accumulated dose from multiple scan examinations averaged over one scan interval in the central region [15, 16]. In 1981, computed tomography dose index (CTDI) was introduced to correct for scan spacing and estimate MSAD in a standardized method [15, 17, 18]. $CTDI_{100}$ is defined as dose measured during a single axial rotation of the scanner with a 100-mm pencil ionization chamber inserted in a standard cylindrical, Plexiglas (polymethyl methacrylate or PMMA) phantom (32 cm and 16 cm diameter) [19, 20].

$CTDI_{100}$ is calculated by dividing the integrated absorbed dose from a single axial scan at a fixed table position by the radiation beam width [21-24],

$$CTDI_{100} = \frac{1}{NxT}\int_{-50}^{+50} D(z)dz, \tag{4-1}$$

where N is the number of image sections, each with the nominal thickness T (mm), from a single rotation and D(z) is the dose as a function of position along the z axis (axis of rotation). Absorbed dose, in units of milligray (mGy), is the amount of energy absorbed per unit mass [19, 25].

The 16 cm diameter head phantom is used to determine CTDI for children and adult head protocols. The 32 cm diameter body phantom is used to determine CTDI for adult protocols. The 32 cm diameter phantom used to represent adults is actually much smaller than many adult patients.

Many other CT dose descriptors are derived from $CTDI_{100}$. The subscript 100 denotes the measurement length of the pencil ion chamber where measurements are taken at the center (c) and 10 mm below the surface (p) of a phantom [24]. When imaging an object, CTDI varies across an axial field of view and generally is a factor of two higher at the surface than at the center of the field of view [23]. Weighted CTDI ($CTDI_w$) provides an estimate of the $CTDI_{100}$ averaged across the field of view [15, 26]:

$$CTDI_w = \frac{2}{3} * CTDI_{100,periphery} + \frac{1}{3} * CTDI_{100,center} \tag{4-2}$$

where $CTDI_{100,periphery}$ represents an average of measurements at four equally-spaced locations around the periphery of the phantom and $CTDI_{100,center}$ represents the measurement taken at the center of the phantom.

Volumetric CT dose index ($CTDI_{vol}$) represents dose for a specific exam protocol and accounts for any gaps or overlaps between the radiation dose profiles from consecutive rotations of the x-ray source [15, 23]. $CTDI_w$ represents the average radiation dose over the x and y direction whereas $CTDI_{vol}$ represents the average radiation dose over all directions (x, y, z) where N is the number of simultaneous axial scans per rotation, T is the thickness of one axial scan and I is the table increment per axial scan [23, 27]:

$$CTDI_{vol} = \frac{N \times T}{I} \times CTDI_w \qquad (4\text{-}3)$$

The $CTDI_{vol}$ is fixed and independent of patient size and scan length thus, $CTDI_{vol}$ does not quantify dose to a patient but rather indicates the radiation intensity that is directed to patients [28].

4.1.2 Dose-length product

Dose-length product (DLP) is determined by multiplying the $CTDI_{vol}$ with the irradiated scan length[22]. DLP reflects the total energy absorbed in a complete scan acquisition [27].

$$DLP = \ CTDI_{vol} x \ L, \qquad (4\text{-}4)$$

where L is the scan length (cm) and $CTDI_{vol}$ is retrieved from the CT scanner.

The $CTDI_{vol}$ and DLP are standardized values provided by the CT scanner to estimate and compare dose between protocols on the same scanner or across different scanners. Using these standard dose descriptors can underestimate or overestimate dose to a patient if the patient size is smaller or larger, respectively, than either the 32 cm diameter (body) or 16 cm diameter (head) cylindrical Plexiglas phantoms used to estimate CTDI_{100} [17].

It is important to note that dose distribution is non-uniform both within an individual CT slice and along a patient [29] which is not captured using an uniform phantom to model a patient. Unlike a uniform phantom, a patient has organs and tissues that affect dose distribution.

4.1.3 Effective Dose

Effective dose (E), in units of millisieverts (mSv), is a dose descriptor that reflects the biological sensitivity of irradiated organs and tissues. E facilitates the comparison of biological risk among different types of imaging examinations [23]. E is intended to estimate radiation dose for a population and not for an individual [30], however caregivers commonly use E to communicate to patients and each other the amount of radiation dose to an individual patient from a specific CT scan [31]. E can be derived from organ and tissue absorbed doses or estimated from other CT dose indicators such as DLP or CTDI [32].

In the clinical setting, E is estimated using the DLP method (E_{DLP}) by multiplying a standard conversion factor (k) in units of $\mathrm{mSv} \times \mathrm{mGy}^{-1} \times \mathrm{cm}^{-1}$ for a particular region of the body by the scanner-provided DLP [19] :

$$E_{DLP} = DLP \times k \qquad (4\text{-}5)$$

Traditionally, E has been computed for CT scans using pre-tabulated MC simulations based on an adult reference phantom. The International Commission on

Radiological Protection (ICRP) defines a reference adult as a Caucasian man that is an inhabitant of Western Europe or North America weighing 70 kg with a height of 170 cm[33]. The dimensions for reference man were obtained in the 1970s and 80s [34]. Measurements or simulations based on a patient model that utilizes the reference man dimensions or Plexiglas phantom with unrealistic anatomy are commonly used for estimating dose to radiosensitive organs during CT examinations [30].

Estimating E by dose map method ($E_{DoseMap}$) requires taking the sum of equivalent dose (EQ). EQ is calculated by multiplying absorbed dose (D) retrieved from dose maps for each organ, i with the appropriate tissue-weighting factor (w).

$$EQ_i = w_i * D_i \tag{4-6}$$

$$E_{DoseMap} = \sum_i EQ_i \tag{4-7}$$

Tissue-weighting factors are meant to represent the relative radiation sensitivity of each type of body tissue as determined from population averages over age and sex and are derived primarily from the atomic bomb survivors [22]. Since 1977, three different sets of tissue weighting factors have been defined by ICRP publications: ICRP 26, ICRP 60, and ICRP 103 [35]. The k factors currently used are based on ICRP 60.

4.1.4 Size Specific Dose Estimate

The American Association of Physicist in Medicine (AAPM) recently described the use of size-based conversion factors to determine a SSDE from scanner-reported $CTDI_{vol}$ [2]. Conversion factors were generated from studies by four independent research groups, which included MC-based dose measurements and physical dose measurements in phantoms. Factors were provided for a range of patient effective diameters (mm) for adjustment of $\mathrm{CTDI_{vol}}$ values obtained from standard 16- or 32-cm diameter PMMA cylindrical reference phantoms.

Effective diameter can be computed using lateral (LAT) and anterior-posterior (AP) patient dimensions:

$$\text{Effective diameter} = \sqrt{LAT \times AP}\,, \tag{4-8}$$

where LAT is the thickness of the patient from left to right and AP is the thickness of the patient from front to back. The conversion factor for conversion of $\mathrm{CTDI_{vol}}$ values obtained from a 32-cm diameter PMMA phantom is computed using the following equation:

$$\text{Conversion factor} = a \times e^{-b\,(effective\ diameter)}, \tag{4-9}$$

where a = 3.70 and b = 0.0367 [2]. The SSDE (mGy) for each patient is then computed by multiplying the conversion factor and the $\mathrm{CTDI_{vol}}$ (mGy):

$$\text{SSDE} = \text{conversion factor x } \mathrm{CTDI_{vol}}. \tag{4-10}$$

CHAPTER V

TYPES OF PHANTOMS

5.1 Plexiglas Phantoms

Plexiglas phantoms simulate the thickness of a patient and are the most commonly used phantoms for dose estimation. Usually these phantoms contain holes drilled along the central axis in addition to four or eight holes around the perimeter for insertion of dosimeters [36]. Limitations associated with using physical phantoms for dose estimation include a lack of sampling of age, gender, and patient size which vary in actual patient population [37].

5.1.1 Anthropomorphic Phantoms

Anthropomorphic phantoms are often made of human skeleton with tissue equivalent material simulating soft tissues and usually comprised of vertical stackable slices with small holes in each slice for dosimeter placement [37]. Anthropomorphic phantoms offer a direct advantage over Plexiglas phantoms by physically representing human anatomy with tissue-equivalent materials to account for different tissue interactions with radiation [38, 39]. Use of anthropomorphic phantoms permits measurement of organ doses in CT imaging as well as calculation of effective doses. Using standard phantoms allows for repeated experiments to make measurements of physical quantities using radiation detectors that have been placed on or within the object [34].

A well-known anthropomorphic dosimetry phantom called ATOM contains resins and polymers capable of simulating any tissue in the human body [38] (Fig 5.1). Photon attenuation values are within 1% of actual attenuation for soft tissue and bone substitutes and within 3% for lung [40].

Figure 5.1: Image of ATOM anthropomorphic phantom [41] [Permission granted for reprint]

5.2 Computational Phantoms

There are three types of computational phantoms: mathematical, voxel, and hybrid**.**

5.2.1 Mathematical Phantoms

Mathematical (stylized) phantoms (first generation) utilize 3D surface equations to characterize planes, spheres, cylinders, cones, and ellipsoids to represent body organs [34, 42] (Fig 5.2). Fisher and Snyder at the Oak Ridge National Laboratory (ORNL) developed a hermaphrodite (includes both male and female organs) phantom in 1966 [42]. This group revised the existing phantom to incorporate three different material compositions named Medical Internal Radiation Dose (MIRD 5)-type phantoms which is based on reference data of ICRP 23 [34, 43]. Another version of mathematical models used to represent male and female adults were called ADAM and EVA developed by Germany's National Research Center for Environment and Health (GSF) [44]. These phantoms were a modification of the hermaphrodite MIRD5 phantom [34, 43]. Cristy and Eckerman integrated the phantoms developed at ORNL and introduced a new series of stylized phantoms of various ages (1- year, 5-year, 10-year, 15-year, and an adult) based on ICRP publication 23 in 1980 [43].The majority of these phantom models represent an 'average or standard individual' defined by ICRP's data on the reference man which is not representative of Americans today [33, 45].

Mathematical phantoms are made simply and intended to represent whole populations instead of individual patients [46]. These equations do not accurately represent real human organ anatomy which can contribute to over- or underestimation of radiation dose. Yet, mathematical phantoms represent an advantage over cylindrical Plexiglas phantoms because they more closely resemble a patient and try to account for human organ anatomy.

5.2.2 Voxel Phantoms

Voxel (tomographic) phantoms (second generation) are computational models of human anatomy [45]. Pixel data from CT images are mapped to 3D volume elements (voxels) representative of the shape, volume, and composition of the human anatomy [34, 47, 48] (Fig 5.2). Each voxel is defined as a material type based on a fixed HU threshold value so that it is assigned and identified as belonging to a particular organ or tissue [34].

Using scanner-specific data and voxel-based computational models can improve the accuracy of organ doses derived from mathematical phantom models [45]. Voxel phantoms offer a more realistic approach than mathematical phantoms because voxel phantoms use the patient’s own CT images and anatomical uncertainties inherent in a computational model may be eliminated [45]. But voxel phantoms are less flexible regarding permitting changes in body posture and contour, internal organ shape, position and depth [49].

5.2.3 Hybrid Phantoms

Hybrid phantom (most recent generation of computational phantoms) incorporates the reference body dimensions and anatomy from an adult or pediatric CT image in compliance with the recommended organ and body dimensions from the ICRP [37, 50] (Fig 5.2). Hybrid phantoms use a combination of techniques such as non-uniform rational B-spline (NURBS) surfaces, boundary representation (BREP), polygon mesh models to make the phantom more realistic [32, 37]. These phantoms were introduced by researchers at University of Florida and the National Cancer Institute.

NURBS is a mathematical modeling technique commonly used for generating curves and surfaces in computer animation [49, 51]. NURBS surfaces provide the flexibility to describe and manipulate the boundaries of internal organs and exterior body surfaces which is helpful in describing complex tissues structures [49, 51]. Polygon mesh models are adapted to NURBS surfaces where 3D control points can be modified to permit organ reshaping and repositioning [47]. BREP modelling technique provides more anatomically realistic models that also allow deformation of surfaces, which is useful for organ motion or sizing and scaling for different body morphometrics [32]. The utility of this feature makes it more valuable because simulation of different organ volumes and body contours are possible.

Similar to mathematical phantoms, hybrid phantoms also include a newborn, 1, 5, 10, 15 year old, adult male and female [50]. The NURBS structures can be filled with voxels for any patient size resulting in a hybrid-voxel phantom hence taking advantage of both mathematical and voxel phantoms [47].

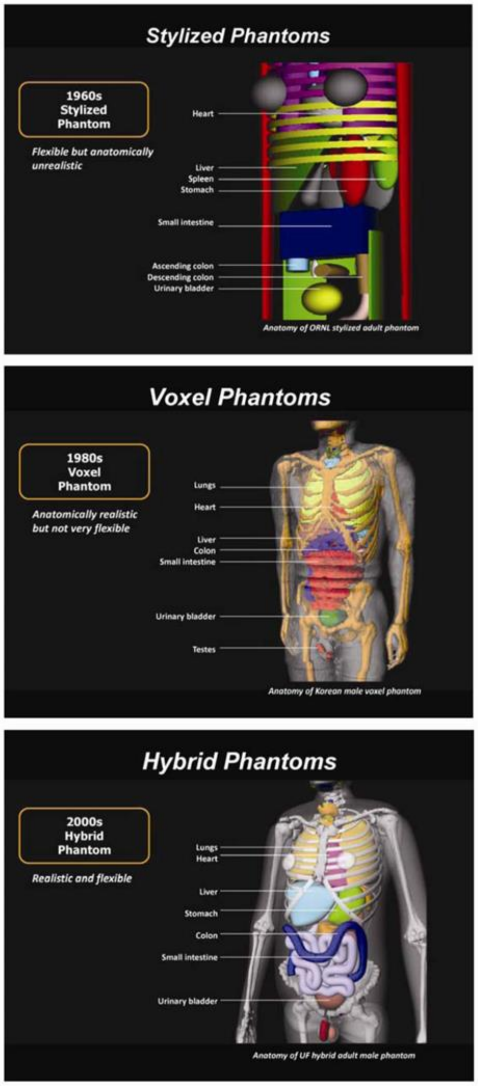

Stylized Phantoms

1960s
Stylized
Phantom

Flexible but anatomically unrealistic

Anatomy of ORNL stylized adult phantom

Voxel Phantoms

1980s
Voxel
Phantom

Anatomically realistic but not very flexible

Anatomy of Korean male voxel phantom

Hybrid Phantoms

2000s
Hybrid
Phantom

Realistic and flexible

Anatomy of UF hybrid adult male phantom

Figure 5.2: A comparison of computational phantoms: mathematical (stylized), voxel (tomographic), and hybrid phantoms [47] (Permission granted for reprint).

CHAPTER VI

RADIATION EXPOSURE AND DOSE DETECTORS

6.1 Dose Detectors

Organ doses cannot be measured directly in patients so physical anthropomorphic phantoms are used to simulate the human body. For direct organ dosimetry, measurements are performed by placing dosimeters in a physical anthropomorphic phantom. Dosimeter measurements can be laborious and time consuming but they provide information on dose distributions. Dose detectors include pencil ionization chambers, film, thermoluminescent dosimeters (TLDs), and metal-oxide semiconductor field effect transistors (MOSFETs).

Most commonly used dosimeters are TLDs and MOSFETs. Unfortunately, point dose measurements cannot accurately represent the average organ dose in cases of high dose gradients [37].

6.1.1 Pencil Ionization Chamber

The ion chamber pencil was developed to measure radiation exposure from a CT scan. It is a small-diameter, air-equivalent radiation detector with a varying length of 10-

15 centimeters (cm) [20]. Chamber readings give exposure in units of roentgens (R) or air kerma in units of Gray (Gy) [52]. Pencil ionization chambers are used to investigate and measure the shape of the radiation beam width in the z-direction [36]. A radiation dose profile produced from the measured radiation beam characterizes the variations along the length of the patient or phantom in the z-direction [53]. This measurement represents the amount of radiation for a given point in the x-y plane independent of the z-axis for a single axial image acquisition [54].

To achieve accurate readings, ion chambers require calibration to a standard reference value. Standard reference values are maintained at the National Institute of Standards and Technology (NIST) [52].

6.1.2 Film

Radiographic film consists of one or two layers of radiation sensitive emulsion. This emulsion comprised of silver halide (AgBr and AgI) grains are contained in a gelatin base [5]. Radiation interaction with silver halide forms a latent image in the film and the image becomes visible during processing [5]. Chemical solutions are used to process exposed film which converts the latent image into an image that is visible at different optical densities (shades of gray) [55]. The relationship between optical density and exposure (measured in milliroentgen) depends on characteristics of the film emulsion and the processing conditions.

A newer type of film, radiochromic is similar to radiographic film except it does not require chemical processing and it is self-developing. Polymerization occurs when the dye contained in radiochromic film is exposed to radiation [56]. A densitometer measures the transmission of the light through the film when the polymer absorbs light [56]. Using an organ volume dosimetry technique, Brady et al showed good agreement between radiochromic film and TLD measurements [57].

Film provides excellent spatial resolution and can measure exposure at many points simultaneously by wrapping the phantom surface which shows qualitative features of the surface dose distributions [54]. However, it can be challenging to maintain acceptable reproducibility of the entire process including chemical processing and uniform film sensitivity [52].

6.1.3 Thermoluminescent Dosimeters

Thermoluminescent dosimeters (TLDs) come in different forms: powder (crushed crystals), solid forms (chips or ribbons) or extruded and embedded in a matrix [52, 54]. The literature mostly describes the use of TLDs as crystals comprised primarily of lithium fluoride (LiF) [5, 36, 52]. The effective atomic number for LiF is close to that of human tissue making it an excellent material choice for phantom dosimetry [5].

Exposing TLDs to ionizing radiation causes electrons to become trapped in excited states [5, 52]. As the TLD is heated, electrons fall to their ground state and energy is released by emitting light [5, 52]. This light can be read by a photomultiplier which converts light into an electrical signal [5].

The TLD can be reused by annealing (baking in a high temperature oven). The annealing process for TLDs can affect dose measurements; therefore, using TLDs requires meticulous handing to ensure precision and repeatability in measurements [52]. TLDs are considered the gold standard for organ dosimetry [38, 57].

6.1.4 Metal-Oxide Semiconductor Field Effect Transistors

A metal-oxide semiconductor field effect transistor (MOSFET) is a layered device consisting of a source, drain, and a gate built on either n-type or p-type silicon (Si) semiconductor substrate [58-60]. The Si substrate is insulated by the polysilicon gate in the middle and the silicon dioxide (SiO_2) on opposite ends [58, 60].

Exposure to ionizing radiation generates a significant number of electron-hole pairs which become trapped at the Si-SiO_2 interface [58, 60]. The buildup of positive charges allows current to flow between the source and drain [58-60]. The voltage that initiated the current flow between the source and drain of the MOSFET is characterized as the threshold voltage [59, 60]. The difference in voltage shift (before and after the radiation exposure) is proportional to the total quantity of trapped charges [58]. The irradiation of MOSFETs causes a permanent shift in the threshold voltage. This shift is proportional to the absorbed radiation dose deposited in the Si-SiO_2 making MOSFETs useful for CT radiation dosimetry [59]. The magnitude of the difference in voltage shift must be calibrated to a known radiation quantity (usually measured with an ionization chamber) to ensure accurate dose measurements [58, 60].

MOSFETs possess excellent spatial resolution and offer little attenuation of the beam due to their small size (0.2 mm x 0.2 mm) which is advantageous for phantom dosimetry [61]. MOSFETs give point dose measurements and provide immediate dose readouts [58]. Newer developed MOSFETs with a high sensitivity bias supply provides an increased dose response suitable for diagnostic energy ranges [62]. Increasing the bias voltage could improve sensitivity at low dose measurements [62]. Yoshizumi et al [43, 45] used a 1.4 mGy for minimum dose detection with a 25% uncertainty. Use of MOSFETs for organ dosimetry has been shown to be in good agreement with TLD measurements [60, 61, 63].

CHAPTER VII

RADIATION EXPOSURE AND DOSE SIMULATION

7.1 Monte Carlo

Organ doses cannot be measured directly in patients so Monte Carlo (MC) methods are performed on a computational anthropomorphic phantoms to simulate the human body by taking into consideration CT source, filtration, tube current, and scanner geometry [64].

MC methods are used to determine specific organ doses by simulating the absorption and scattering of x-ray photons in various tissues during CT imaging [65, 66]. MC simulations are based on detailed information on the source distribution geometries (distance between source and center of rotation), x-ray beam shaping filter, x-ray spectra, and a computational (mathematical, voxelized, or hybrid) model of the human anatomy [67]. Radiation transport is modeled by using Monte Carlo codes incorporating Poisson statistics to track individual photon histories. Random distances which a photon travels between interactions such as from a source through a medium (i.e., skin) to the detector are generated [68, 69]. There are libraries of cross section data for the radiation interaction processes for all elements from which the cross section data for body tissues are then evaluated according to their elemental composition and density [46]. Using this physical input data, a photon is tracked from its point of creation in the x-ray tube, through the patient model. The random interactions of the photons are assigned probability functions based on the mass attenuation coefficients of the irradiated tissues [70], thus generating a statistically large number of particle histories [45, 68, 69]. The probability density is used to detail the particle history. The types of radiation processes considered inside of the human body for simulations in medical diagnostic radiology are photoelectric absorption and Compton scattering [46].

With photoelectric absorption, the entire energy of the photon is deposited in the voxel. For a Compton interaction, the energy of the scattered photon is absorbed at the site of interaction. This process continues until either the photon leaves the volume or its energy drops below a certain threshold which results in the photon counted as absorbed [70]. This makes it possible to predict properties of the radiation field such as the particle fluence, energy deposition, and energy spectrum at particular points [68, 69].

In the process, all energy depositions are tallied in a corresponding voxelized grid. A large number of photon histories are simulated in order to obtain a sufficiently precise estimate of the desired dose quantities of interest. Organ doses are determined by summing in each organ and tissue all energy depositions from primary and scattered photons and dividing by the organ mass.

MC methods are well-established for accurate CT dose estimation using physical phantoms [45, 67, 70, 71], mathematical models [42, 68, 72], voxel models [67, 70, 71, 73], and hybrid models [47, 74]. Schmidt and Kalender [73] developed and validated a fast voxel-based MC method that yielded dose values from voxelized CT images of anthropomorphic phantoms that differed less than 5% from CTDI results obtained with a standard MC-based program (EGS4) and published organ dose conversion factors. Researchers have validated this approach by comparing dose estimations from mathematical or voxel models to those from physical phantoms with MOSFETs or TLDs [70, 71]. DeMarco et al [71] showed good agreement between the dose estimated from MC methods applied to voxelized images of cylindrical and anthropomorphic phantoms compared with the dose determined from physical phantoms using MOSFETs. Deak et al [70] found that calculated dose values from 3D dose distributions of voxelized phantom images were within 10% of all phantom measurements (Alderson-Rando and cylindrical CTDI phantoms) using TLDs. It has been reported that using computer simulations for estimating dose offers a more reliable way to obtain accurate organ doses compared to using physical phantoms for dose estimation.[75]

MC methods have been shown to be extremely accurate as they are utilized in radiation therapy treatment planning [76]. Unlike DLP-derived dose estimates, MC simulation permits organ dose estimation and can account for the impact of iodine accumulation on dose [3, 4]. Individual organ dose contributes to the E value and can be used to assess radiation risk from diagnostic imaging procedures [77]. However, differences between human models and actual patients, as well as variations in scanner geometries and X-ray beam spectra, contribute to inaccuracies in organ dose estimation with MC methods [78],[74]. Statistical uncertainty is also inherent in the calculated doses, depending on the frequency and homogeneity of the random interaction events in an organ. Large organs within the beam are characterized by small uncertainties, whereas small organs outside the beam may have large statistical errors [48].

7.2 Monte Carlo-based Dose Calculators

In 1991, two comprehensive organ dose databases were developed; National Radiological Protection Board (NRPB) in London and National Research Center for Environment and Health (GSF) in Germany based on Monte Carlo simulations that exist in accordance to reference dimensions of the body and organs defined by the ICRP [37, 50]. NRPB published a report (NRPB-SR250) providing tables of organ dose coefficients, normalized to a free-in-air axial scanning of an adult mathematical phantom [24]. Additional software is required to manipulate data to estimate doses for various scanner protocols. The NRPB report provided 23 datasets with various exposure conditions relevant to 27 scanner models (5 manufacturers) that were current during the early 1990s [24]. The NRPB organ database was based on a hermaphrodite mathematical phantom whereas the GSF database was based on male and female mathematical phantoms called ADAM (weight=70 kg, height=170 cm) and EVA (weight=60 kg, height=160 cm) and two pediatric (8 week old classified as BABY and a 7 year old classified as CHILD) voxel phantoms [37, 78-80]. The NRPB database was later updated to include a complete family: 6 mathematical phantoms (newborn, 1 year, 5 year, 10 year, 15 years, and adult) [24, 68]. Meanwhile at GSF, a complete voxel family was also developed representing a range of patient sizes and ages from 8 weeks to 48 years of age including both male and female models [81]. Hence, both databases have been updated.

Both NRPB and GSF datasets provide organ absorbed dose data normalized to the CTDI measured in air at the isocenter ($CTDI_{air}$) of the CT scanner which are dependent on the type of scanner modelled in the MC simulation [82]. The NRPB dataset can be used to estimate average organ doses, ICRP values of organ masses, and E [44]. Graphical user interface software programs (CT-EXPO, CTDOSIMETRY, CTDOSE, WINDOSE, and IMPACT) are based on two organ databases (NRPB and GSF). Various MC-based dose calculators (ImPACT, CT-EXPO, ImpactDOSE) exist to estimate organ and effective doses for a reference person of standardized size and shape depending on the type of scanner used [32].

7.2.1 ImPACT

The Imaging Performance Assessment of CT scanners (ImPACT) group (London, England) developed a patient dosimetry calculator that uses ICRP 60 or 103 tissue weighting factors for adult patients undergoing CT exams to calculate E [79, 83] . IMPACT uses dosimetry data from NRPB. Modern scanners are handled using an ImPACT matching system of dosimetric characteristics of any new scanner to one of the available dosimetry data sets [32, 83]. This process combines ratios of phantom CTDI to the corresponding ‘in air’ CTDI, known as ImPACT factors [83].

7.2.2 CT-EXPO

CT-EXPO (Hannover, Germany) is software package based on GSF organ dose database which calculates age-and gender-specific dose values for a CT scan [50, 79].

GSF data set also uses ImPACT method to match new scanners to a set of scanner-specific correction factors which are related to the available data sets [32].

7.2.3 ImpactDOSE

ImpactDOSE (Erlangen, Germany) previously known as WinDose is a computer-based program that calculates organ and E values for various scanning parameters and anatomic ranges. Based on MC dose simulations performed with standard anthropomorphic phantoms, ImpactDose allows users to select scan parameters (tube potential, current, detector collimation width, and pitch) producing a protocol-specific dose calculation which takes into account overscanning and overbeaming [64]. The computational phantoms used in these calculations represent average males and females which differ from any individual patient. This leads to underestimations of E if the patient is smaller than the model and overestimation of E if the patient is larger than the model [64].

CHAPTER VIII

PRELIMINARY DATA

8.1 Validation of MOSFET Technology

Chapter VIII describes the use of MOSFET technology to evaluate the hypothesis that MC methods performed on CT images of an anthropomorphic phantom can accurately estimate radiation dose to the phantom. Preliminary work towards this evaluation included establishing the ability of MOSFET technology to characterize dose distribution from a CT scan using measurements from an ionization chamber placed in a CTDI phantom. Preliminary work also included the generation and characterization of dose maps.

8.1.1 Pencil Ion Chamber

A 10 cm ion chamber (10X6; 3CT; Accu-Dose 2186; Radcal, Monrovia, California) pencil along with an electrometer was used to measure radiation exposure from the CT scanner which was converted to dose in air. The ion chamber was calibrated to standard reference values.

A dose reading from the ion chamber represented the average exposure over the length (l) of the chamber (l= 100 mm) from a single axial radiation dose profile (Fig 8.1).

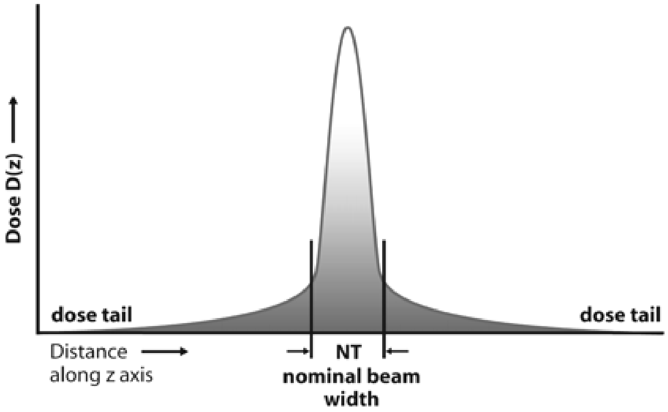

Figure 8.1: Radiation Dose Profile [15, 17] (Permission granted for reprint)

The ion chamber reading was expressed as:

$$I_{(z=0)} = \frac{1}{f*l}\int_{-\frac{l}{2}}^{\frac{l}{2}} D(z)dz, \tag{8-1}$$

where f (f-factor) is used to convert air kerma to dose in air, f=1 mGy/mGy [21] and *l* is the length of the ion chamber, *l* = 100 mm. D(z) represents the absorbed dose profile along the z- axis.

8.1.2 Calibration Method

Calibration of MOSFETs required a 32-cm diameter cylindrical polymethyl methacrylate (PMMA) phantom and a 100 mm pencil ionization chamber using a 256- slice CT scanner (iCT Brilliance, Philips Medical Systems, Cleveland, OH). The PMMA CTDI-phantom contained nine removable acrylic inserts of 1 cm diameter: one hole in the center, four at the periphery, and four holes in the inner portion (of 16-cm diameter) (Fig 8.2). The ion chamber pencil was inserted in each of the nine holes of the CTDI phantom. For a single axial acquisition, calibration was performed for three energy levels at 80, 100, and 120 kVp with a corresponding tube current of 920, 533, and 320 mA respectively. A reading was recorded after eight consecutive measurements were performed for each CTDI hole. These eight measurements allowed sampling of 360 degrees of the tube rotation since the starting tube position is unknown and changes for each scan.

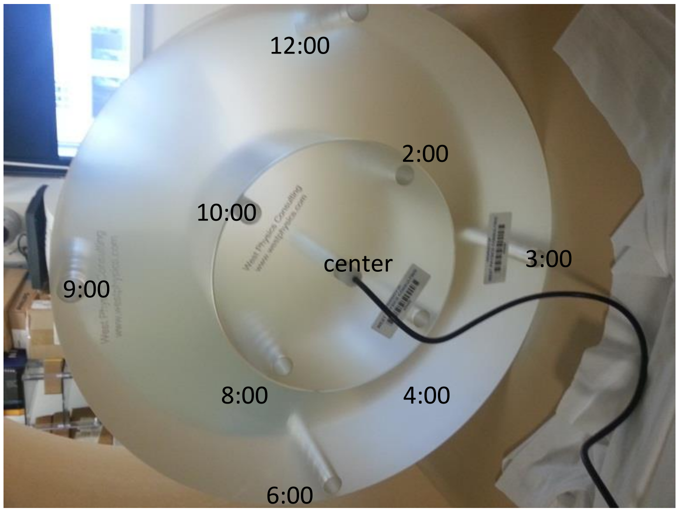

Figure 8.2: CTDI phantom with ionization pencil placed in the center

MOSFET dosimeters were calibrated to translate voltage readout to absorbed dose. Two mobile MOSFET readers were used with high sensitivity MOSFETs (TN-1002RD-H;

Best Medical, Ottawa, Canada). Five MOSFETs were attached to each reader. MOSFETs were placed inside of the PMMA holders marked with 5 mm increments.

The MOSFETs were measured when inserted in each of the nine holes (same protocol as ion chamber measurements). The beam width (10mm in the z-axis) used for calibration satisfied the minimum width required by the Nyquist criterion for MOSFET samples. A dose reading was recorded at each location as the MOSFETs were moved along the z-axis according to the 5 mm lines labeled on the holder. The MOSFET holder contained 21 marked line positions. The holder was moved 21 positions according to the lines marked in 5 mm increments which summed to a total of 100 mm. Identical to the ion chamber measurements, eight axial scans were performed for each position. A Bluetooth wireless device sent the voltage data from the MOSFET readers to a PC laptop.

An average MOSFET reading was calculated by integrating the dose under the curve and compared to an ion chamber reading. Integration was approximated using Riemann middle sum (equation 8-2). A calibration factor per hole (CF_h) was calculated for each of the 9 holes where M_k is a MOSFET reading for position k which corresponds to the lines on the holder, dx = 5mm, l = 100 mm and I_n is a single ion chamber reading for that hole:

$$CF_h = \frac{\sum_{k=2}^{20} M_k dx + \sum_{k=1,21} \frac{M_k dx}{2}}{l \sum_{n=1}^{5} I_n}, \tag{8-2}$$

Then CF_h was averaged for each energy level to cover the distribution in the z-axis. CF is the average for all nine holes:

$$CF = \frac{1}{9}\sum_{n=1}^{9} CF_h \tag{8-3}$$

8.1.3 Findings

MOSFET calibration yielded CFs for 3 different energies (80, 100, and 120 kVp). The CFs calculated for each energy level was close to 3mV/mGy (Table 8-1). Dose distributions' readings based on one CTDI hole position (12:00 position) for 21 different locations along the ion chamber length are shown in Figure 8.3. The voltage readings' profile showed a similar radiation dose profile as seen in Figure 8.1. The peak dose value represents the dose to the center of the ion chamber (z=0). There is a decline in the dose values to the left and right of the peak dose value which represents scattered radiation dose of the axial scan. A similar distribution was seen for the different CTDI phantom holes; some peaks were lower than the peak displayed in Fig. 8.1 which could be due to scattering.

Tube potential (kVp)	80	100	120
Calibration Factor (CF)	3.133	2.993	2.874

Table 8.1: Key parameters for axial scans used for ion chamber and metal-oxide semiconductor field effect transistors (MOSFET) measurements and calculated calibration factor

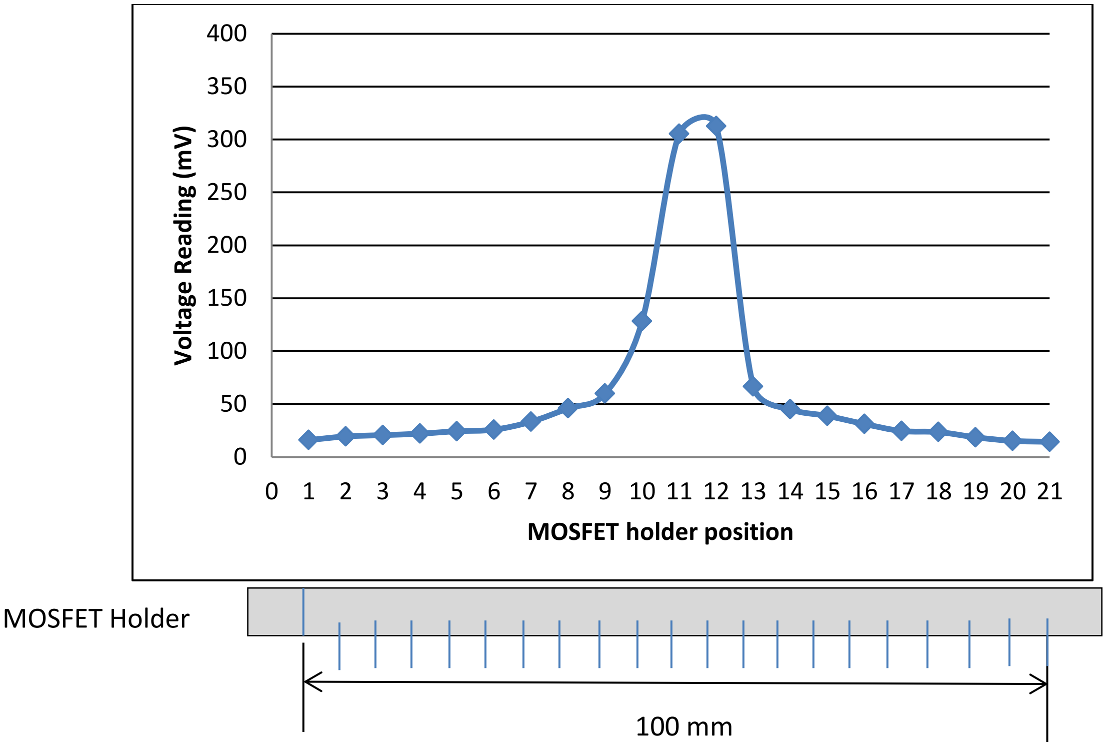

Figure 8.3: Voltage readings of dose distribution for one hole location in the CTDI phantom in the z-axis along the 100 mm length of the ion chamber for an axial 120 kVp scan.

8.1.4 Observations

The CF values were close to 3mV/mGy, which is in accordance with the expected range, as advised by the MOSFET manufacturer. Still, there were slight differences in CF values for the 3 different energies, consistent with the manufacturer's claim of MOSFET sensitivity to different energy levels. The dose profile showed that MOSFETs can characterize the dose distribution well considering heel effect (asymmetry in the dose distribution along the z-axis) and scatter. The measurements were similar to the expected dose profile of an axial scan, as depicted in the literature.

8.2 Creation of Dose Maps

Data from patients with cardiovascular disease were acquired using a 256-slice CT scanner (iCT Brilliance, Philips Medical Systems, Cleveland, Ohio). Patients were imaged clinically for a variety of indications including evaluation of the coronary arteries, pulmonary veins, or thoracic aorta. Data were acquired using either a prospectively ECG-triggered axial or a retrospectively ECG-gated helical technique depending on the clinical indication and the patient's heart rate. X-ray tube potential and tube current were chosen based on the patient size. This study was approved by our institutional review board with waiver of informed consent and was compliant with the Health Insurance Portability and Accountability Act.

Patient data were used to create dose map volumes displaying pixels as $CTDI_{vol}$-normalized absorbed dose values. Scanner configuration and acquisition parameters were extracted as input for the MC tool. This permitted modeling of scanner characteristics (CT scanner geometry, table geometry, beam collimation, bow-tie filter composition). A patient-specific virtual phantom was created by voxelizing each patient's image set (Fig 8.4). Tissues were classified into various classes (dependent on user) pre-selected from International Commission on Radiation Units and Measurements (ICRU) Report 44 in order to represent the patient's materials and their chemical stoichiometry. Each voxel was classified as one of five material types based on fixed Hounsfield unit (HU) threshold values: air (-1000 HU), lung (-930 HU), adipose tissue (-200 HU), soft tissue (+5 HU), and cortical bone (+400 HU). Each voxel was assigned a molecular formula and a mass density estimate based on its attenuation [84].

Figure 8.4: Voxelized image of a patient

A large number of photon histories were simulated to obtain precise estimates [85]. The energy deposited in each voxel was computed and tallied in a corresponding voxelized grid [85]. The energy imparted (Joules) was divided by the mass (kg) of the irradiated tissue to determine the $CTDI_{vol}$-normalized absorbed dose in each voxel. Normalized absorbed dose was multiplied by the scanner-provided $CTDI_{vol}$ (mGy) to obtain absorbed dose (mGy).

8.3 Characterization of Dose Maps

The impact of patient parameters (e.g. patient size), mode of data acquisition, and scan parameters on dose distribution were evaluated. A color scale was used to describe the dose levels of the CT data set. Regions of higher dose were designated in a red hue where regions of lower dose were designated in a blue hue. $CTDI_{vol}$-normalized absorbed dose values were displayed on the CT images.

These preliminary dose maps demonstrated differences in dose distribution reflecting differences in patient size and body region imaged as well as the scan protocol. Obese patients tended to have higher doses in the periphery compared to smaller patients who demonstrated an even distribution of dose throughout their anatomy (Fig 8.5). Dose maps showed that smaller patients absorbed a higher amount of radiation to critical organs than larger patients for equivalent exposures. Comparing dose distribution from two patients of different sizes showed the presence of additional adipose tissue affects the breast and lung dose (Fig 8.6). Tissues are exposed to entrance radiation as the tube rotates around the patient [53]. X-rays are attenuated by less tissue in smaller patients which leads to higher amount of dose in the center versus the periphery of the patient. For obese patients, exit radiation is much less intense because of the attenuation of x-rays through a greater amount of tissue which is why there is a higher amount of dose in the periphery [53].

Differences in dose distribution were also observed between helical and axial scans (Fig 8.7). Helical scans tended to have an even distribution of dose throughout the length of the scan. The amount of dose observed at each end of the scanned anatomy was less. However, there was an increase in dose where the axial scans overlapped slightly. The red circular lines in the last column indicate the approximately 400° rotation of the tube needed to complete each axial scan of the array of images on the right (Fig 8.7).

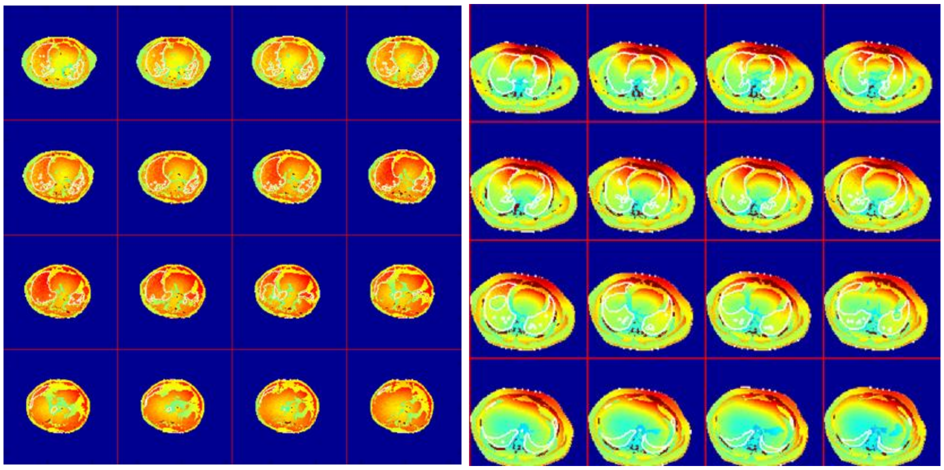

Figure 8.5: Two preliminary dose maps show cross-sectional slices through the chest of a slim patient (left) and an obese patient (right) where regions of higher dose are designated in a red hue and lower doses designated in a blue hue.

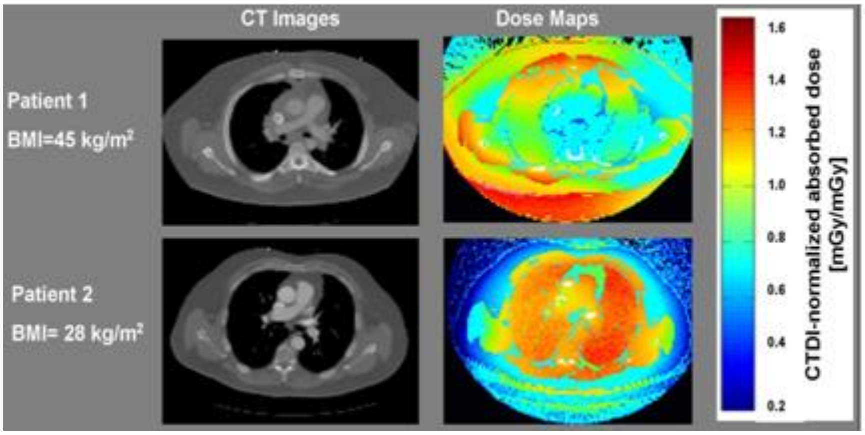

Figure 8.6: A comparison of dose distributions in two different-sized patients shows that patient 1 (BMI=45 kg/m^2) had higher dose in the periphery due to the presence of additional adipose tissue compared to patient 2 (BMI = 28kg/m^2) who had a higher dose in the lungs due to less adipose tissue.

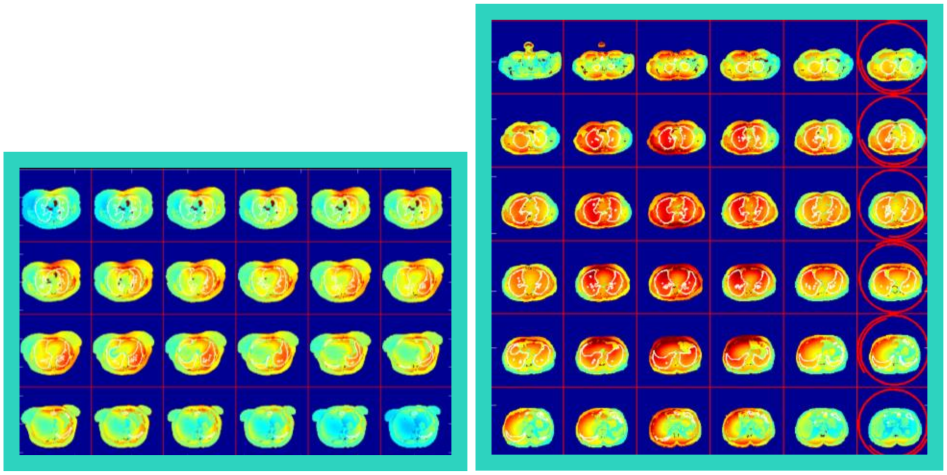

Figure 8.7: Two sets of preliminary dose maps show retrospectively electrocardiogram (ECG)-gated axial scans (left) and prospectively ECG-triggered scans (right) of the chest.

8.4 Approach for Segmenting Organs from Dose Maps

An approach was developed to segment organs on dose maps in order to evaluate individual organ doses and calculate E. A JAVA based program (ImageJ) was chosen to segment organs based on its ease of use. Dose maps were read using ImageJ with an image type ‘32-bit real’. Organs were manually segmented (Fig 8.8). Segmentation of organs completely contained within the scan field was straight forward. Partially irradiated organs (e.g, stomach and liver) were also considered because scattering occurs during CT exams. An innovative approach to the segmentation of these organs had to be developed.

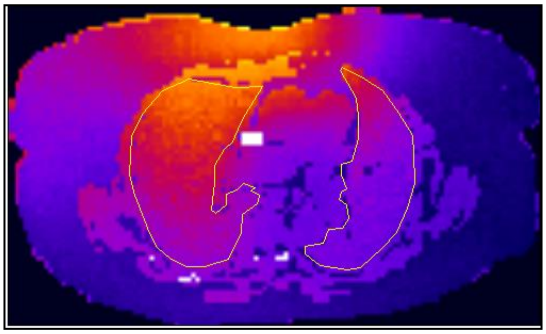

Figure 8.8: Segmented lungs for a patient with BMI = 32 kg/m^2

A correction factor was included for weighted average organ dose based on direct and indirect organ exposure of a partially irradiated organ. The weighting factor for each organ was linearly proportional to the length (cranial-caudal extent) of the directly and indirectly exposed regions (the length of the indirectly exposed region was based on estimates of overall organ length). To obtain whole organ doses, the average dose of the indirectly irradiated portion of the organ was determined by estimating the organ length and modeling the dose fall-off outside the scan range using an extrapolation model (Fig 8.9). Based on the data from dose simulations, the dose fall-off in the indirect dose region was modeled by a linear profile as a function of organ length with a fixed decreasing slope of 10% per centimeter relative to the dose in the directly irradiated portion of the organ. Indirect dose to the organ was then estimated as the average of the modeled doses at the beginning and end of the indirect dose region.

Let l be the total z extent of the organ. Then let p_r be the relative fraction of the organ length included within the directly irradiated region, and $1 - p_r$ the relative fraction within the indirectly irradiated region. Further, let D_r be the dose in the directly irradiated region determined from dose maps and let D_i be the average of doses at the beginning (D_r) and end (D_d) of the indirect radiation region determined from dose modeling. If the linear dose decline with slope m is described by $D_r \cdot (1 + l_d \cdot m)$ at a dose decline length (l_d), the average organ dose (D_o) can then be estimated as:

$$D_o = p_r \cdot D_r + (1 - p_r) \cdot D_i \,, \tag{8-4}$$

$$\text{where } D_i = \frac{D_r + D_r \cdot (1 + (1 - p_r) \cdot l \cdot m)}{2} \tag{8-5}$$

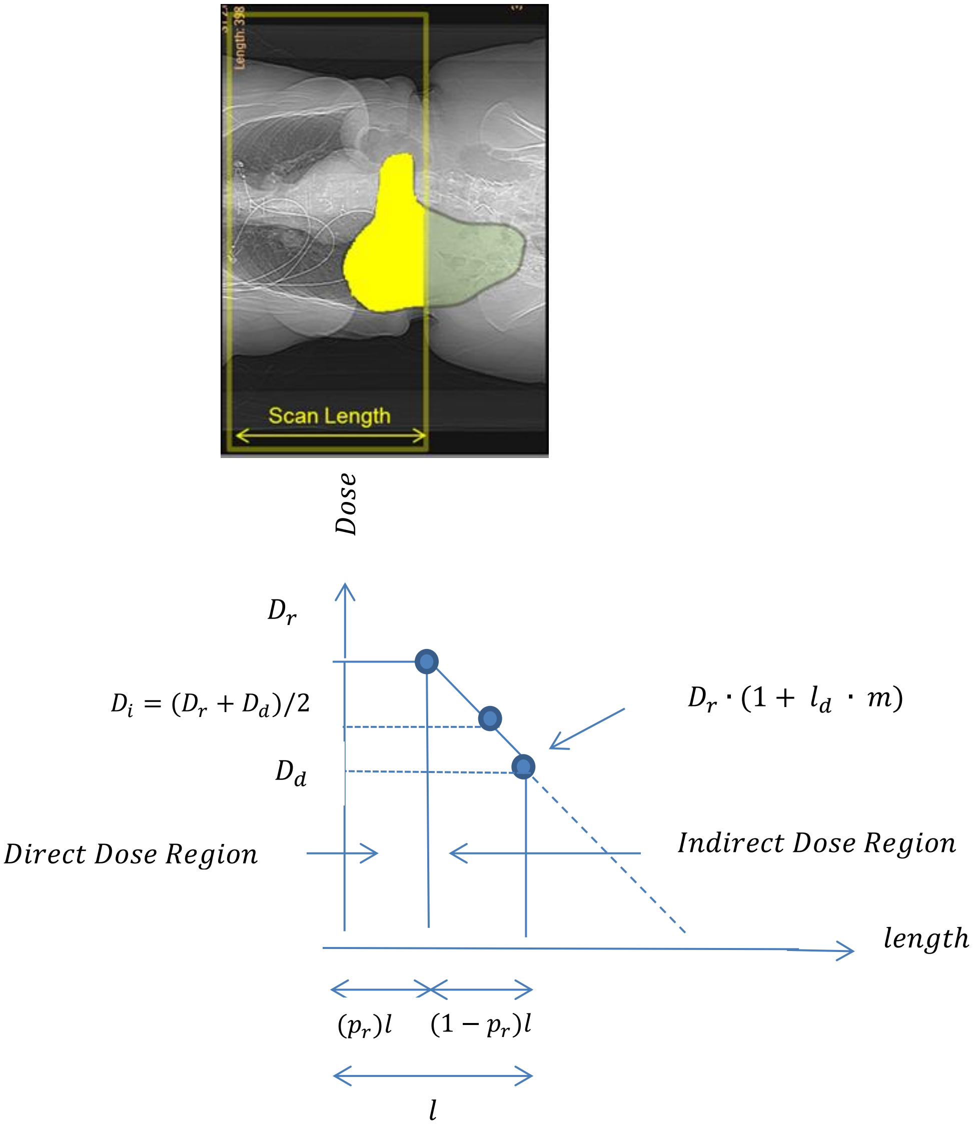

Figure 8.9: (Top) Only a portion of the liver is included in the scan range and directly irradiated (yellow). The remainder of the organ absorbs indirect radiation (green). (Bottom) A graphical representation of dose to the directly irradiated portion and indirectly irradiated portion of an organ is shown.

A $\mathrm{CTDI}_{\mathrm{vol}}$-normalized absorbed dose value was retrieved for each segmented organ. Normalized absorbed dose was multiplied by the scanner-provided $\mathrm{CTDI}_{\mathrm{vol}}$ (mGy) to obtain absorbed dose (mGy).

CHAPTER IX

DOSE MAP VALIDATION

9.1 Introduction

A strong motivation exists for improving the current methods of estimating radiation dose to patients who undergo CT examinations. MC methods provide a powerful computational tool to simulate radiation dose for wide range of applications including radiation therapy and CT scans [86]. MC techniques can generate dose distributions by simulating a large number of particle histories as they emerge from the source of radiation and multiple scattering interactions both inside and outside the patient. MC methods have been shown to be highly effective in estimating dose distributions.

Many multipurpose MC packages are used to simulate ionizing radiation for dosimetry in phantoms: Electron Gamma Shower (EGS), EGS national research council (EGSnrc), general Monte Carlo N-Particle transport code (MCNP), and Geometry and

Tracking (GEANT4) system. Most of the MC packages have freely available executable software but making any modifications to the software is limited [70]. Generally, MC simulations have only been validated for older single-slice CT scanners [32, 87]. Some MC tools have been used to simulate radiation dose from newer single-source, 64-slice scanners [71, 88, 89] but the accuracy of such tools for the newest CT scanners is largely unknown.

We evaluated the accuracy of dose calculations from MC simulations performed on an anthropomorphic phantom for a range of CT scan protocols using metal-oxide semiconductor field-effect transistor (MOSFET) dosimeters placed inside the phantom.

9.2 Materials and Methods

9.2.1 Anthropomorphic Phantoms

An adult phantom (ATOM 701; CIRS, Norfolk, VA) and a pediatric phantom (ATOM 704-D; CIRS, Norfolk, VA) containing tissue-equivalent polymers and resins capable of simulating any tissue in the human body was used. Phantom photon attenuation values are within 1% of actual attenuation for soft tissue and bone substitutes and within 3% for lung. Both phantoms are divided into 25 mm contiguous sections each containing 5 mm holes for MOSFET placement. Medium-size tissue equivalent breast attachments were added to the phantom to assess female adult dosimetry.

9.2.2 CT Scanning

All scanning was performed on a 256-slice CT scanner (Brilliance iCT, Philips Healthcare, Cleveland, OH). Scan protocols included standard brain, cardiac, chest, abdomen and chest-abdomen-pelvis protocols covering the appropriate phantom anatomy (Table 9.1). Each scan was repeated five times for each phantom.

9.2.3 MOSFET measurements

Ten mobile MOSFET readers were used with high sensitivity MOSFETs (TN-1002RD-H; Best Medical, Ottawa, Canada). Five MOSFETs were attached to each reader and MOSFETs were placed in 50 different locations in each phantom. MOSFET readings were recorded after each CT scan and averaged for each MOSFET location.

9.2.4 Monte Carlo simulations

MC simulations were implemented using Diagnostic Photon Simulations (DiPhos, Philips Research, Eindhoven, Netherlands) and performed for each CT scan. For each CT scan, 60 projections were simulated to keep simulation time manageable per tube rotation with approximately 10,000 photons generated per projection. Voxelized phantoms were created from reconstructed CT images with a voxel size of 3.9 x 3.9 x 4.1 mm^3 for the adult and 2.3 x 2.3 x 2.0 mm^3 for the pediatric phantom. Each voxel was classified as a material type based on the average attenuation value: air (-1000 to -930 HU), lung (-930 to -200 HU), adipose tissue (-200 to -5 HU), water (-5 to -5 HU**)**, soft tissue (+5 to +40 HU), skeletal muscle (+40 to + 400 HU), and cortical bone (> +400 HU) [84]. The

National Institute of Standards and Technology (NIST) database was used to characterize the properties of the material within each voxel based on interactions between x-ray photons and the voxelized phantom [90]. Dose was calculated by summing the energy deposited in each voxel over the duration of scanning and dividing by the mass of the voxel.

9.2.5 Comparison of MC simulation results to MOSFET measurements

A conversion factor was used to convert simulated MC results into voltage values to compare to MOSFET measurements. The conversion factor was determined by comparing MOSFET measurements in a CTDI phantom with MC simulations of the same CTDI phantom. MC doses were converted to voltages by multiplying the MC to MOSFET conversion factor. By comparing MC to MOSFET, a ratio was obtained.

Five measurements were averaged to obtain the voltage ratio (dose ratio) of MOSFET j for that set of measurements. The standard deviation of the ratio in the in-field region was estimated by taking the average ratio of MOSFET voltage and voltage from the MC simulation. The error estimate of the ratio in an in-field location was calculated by averaging the estimated error,

$$\sqrt{s_1^2\left(V_{\mathrm{MOSFET},j}/V_{\mathrm{MC},j}\right)}\ , \tag{9-3}$$

where s^2 is the variance of the voltage ratio between the voltage of all in-field MOSFETs (V_{MOSFET}) and the voltage of the MC (V_{MC}) for that particular protocol.

9.3 Results

A total of 26 scan protocols were evaluated and a list of measurement and simulation results are reported (Table 9.1). The average ratio of MOSFET dose and MC dose for the in-field region was close to 1 (range, 0.93 to 1.09; mean ± standard deviation, 0.99 ± 0.04) (Table 9.2).

For all scans except the female prospective ECG-triggered axial scans, the majority of the values for the standard deviation and the average estimated error closely matched each other, indicating that most variation is due to the MOSFET measurement error and that the scans were modeled accurately.

Table 9.1: A description of 26 scans performed on an adult (male and female) and pediatric phantom for different scan modes (helical, electrocardiogram (ECG)-gated helical, and non-gated axial) at varying tube potentials and scan lengths with scanner reported volumetric CT dose index ($CTDI_{vol}$) values.

Scan Series	**Phantom**	**Scan Region**	**Scan Mode**	**Peak Tube Potential (kVp)**	**$CTDI_{vol}$ per scan (mGy)**	**Scan Length (cm)**
1	Female	Chest	Helical	120	27	302.4
2	Male	Chest	Helical	120	27	302.4
3	Male	Chest	Helical	100	17.8	303.0
4	Male	Abdomen	Helical	120	27.0	420.8
5	Male	Brain	Helical	120	62.1	160.0
6	Male	Brain	Helical	100	42.0	160.0
7	Female	Chest	Helical	100	17.8	302.4
8	Female	abdomen	Helical	120	27.0	421.2
9	Female	Cardiac	Non-gated	120	29.5	140.4
10	Female	Cardiac	Non-gated	100	18.4	140.4
11	Female	Cardiac	Non-gated	80	8.2	140.4
12	Female	Cardiac	Non-gated	100	10.7	140.4
13	Female	Cardiac	ECG-gated	120	51.3	140.4
14	Female	Cardiac	ECG-gated	100	30.7	140.4
15	Female	cardiac	ECG-gated	120	51.3	140.4
16	Male	cardiac	Non-gated	120	29.5	140.4
17	Male	Cardiac	Non-gated	100	18.4	140.4
18	Male	Cardiac	Non-gated	80	8.2	140.4
19	Male	Cardiac	Non-gated	100	10.7	140.4
20	Male	Cardiac	ECG-gated	120	51.3	140.4
21	Male	Cardiac	ECG-gated	100	30.7	140.4
22	male	Cardiac	ECG-gated	120	51.3	140.4
23	Infant	Brain	Helical	100	24.9	120.0
24	Infant	Chest	Helical	100	17.6	180.0
25	Infant	Chest	Helical	100	17.6	180.0
26	infant	Chest abdomen pelvis	Helical	100	9.3	315.0

Table 9.2: Summary of results including the average ratio of metal-oxide semiconductor field effect transistors (MOSFETs) and voltage from Monte Carlo (MC) simulated in the in-field region with standard deviation and estimated error calculated for each adult (male and female) and pediatric phantom

Scan Number	**Phantom**	**Number of in-field MOSFETs**	**$<V_{MOSFET}/V_{MC}>$**	**Standard Deviation of the in-field ratio**	**Estimated Error for the ratio in the in-field region**
1	female	29	1.00	0.05	0.05
2	male	26	1.00	0.04	0.05
3	male	26	0.98	0.05	0.05
4	male	25	1.00	0.04	0.05
5	male	6	1.00	0.03	0.05
6	male	6	0.98	0.07	0.05
7	female	25	1.00	0.06	0.05
8	female	29	0.96	0.04	0.05
9	female	15	1.05	0.09	0.06
10	female	15	1.04	0.10	0.06
11	female	15	1.09	0.11	0.07
12	female	15	1.05	0.10	0.06
13	female	17	1.00	0.06	0.05
14	female	17	0.98	0.06	0.05
15	female	17	0.99	0.06	0.05
16	male	12	1.00	0.03	0.05
17	male	12	0.98	0.07	0.05
18	male	12	0.98	0.07	0.06
19	male	12	0.97	0.07	0.06
20	male	14	0.96	0.06	0.05
21	male	14	0.93	0.06	0.05
22	male	14	0.94	0.06	0.05
23	infant	7	0.98	0.05	0.05
24	infant	31	0.93	0.04	0.05
25	infant	33	0.93	0.06	0.05
26	infant	41	0.95	0.06	0.05

V_{MOSFET}/V_{MC} = the ratio of dose measured from MOSFETs and dose simulated from Monte Carlo methods.

9.4 Discussion

Radiation dose estimates using a MC method were strongly correlated with MOSFET measurements in a physical adult (male and female) and infant anthropomorphic phantoms for a wide range of scan protocols performed on a 256-slice CT scanner. MC simulation results were converted into voltage values for comparison to MOSFET measurements.

The standard deviation of the ratio in the in-field region, determined by estimation from the measurement results of that particular scan, indicated that if the estimated standard deviation was close to the estimated error then modeling of the scan was accurate. Although the average ratio of MC dose and MOSFET dose in the directly irradiated region was close to 1, MC results started to deviate from MOSFET measurements as distance from the edge of the direct radiation field increased which is consistent with previous studies [91].

Significant deviations occurred with female prospective ECG-triggered axial scans, male retrospective ECG-gated helical scans, and infant chest/abdomen non-gated helical scans. These deviations could be attributed to both measurement and calibration errors. The average ratio between MOSFET and MC results for female axial cardiac scans were about 5-10% higher than the expected value of 1.00. The standard deviation ratio was higher than the estimated error for these scans possibly indicating a problem with the MC simulations. The source of the error is not immediately known since we would expect to have a similar effect in the other simulations which is not the case. The average ratio was lower than expected for the male helical cardiac scans. This could be attributed to systematically low readings from one of the MOSFETS (leading to ratios below 0.9) used in all male cardiac scans but none of the other scans. For infant scans, average ratios were correct in the head and shoulder region but lower than expected in the chest/abdomen region. The source of this error requires further investigation.

9.5 Conclusion

In conclusion, the MC tool was tested for medical X-ray dose calculation against MOSFET measurements for a wide range of scan protocols for both adult men and women, and an infant. The test showed that the MC tool provides very accurate dose values in most cases.

CHAPTER X

OBESE PATIENT STUDY

A Pilot of Study of Patient-Specific Cardiovascular MDCT Dose Maps and Their Utility in Estimating Organ and Effective Doses in Obese Patients

10.1 Introduction

Recent reports of increased utilization of ionizing radiation-based medical imaging, particularly computed tomography (CT) [92], and concern about the associated potential health risks [93] have created a demand for improved estimation, reporting, and recording of radiation dose from CT. The effective dose (E), in units of millisieverts (mSv), is a dose descriptor reflecting the relative biological sensitivity of irradiated organs and tissues. E has traditionally been computed for CT radiological procedures using sophisticated Monte Carlo (MC) methods to simulate the transport of ionizing radiation through the body [35, 49, 72, 94] . Pretabulated Monte Carlo (MC) simulation data used by CT dose estimate tools such as the ImPACT patient dosimetry calculator, CT-Dose, and CT Expo are based on a 70-kg reference phantom [95] intended to represent the average-sized American adult [96]. Therefore, these tools do not account for overweight or obese patients [96-99]. The mathematical reference phantom used for MC simulations also includes organs that are characterized as simple geometric shapes: cylinders, ellipsoids, and cones [95]. Therefore, standard MC simulation methods for organ dose estimation in the adult population are largely patient generic because individual body habitus and organ sizes are not accounted for in the dosimetry phantom [100].

In the clinical setting, a more practical method for estimating E from a CT procedure uses scanner-provided dose-length product (DLP) values and published DLP conversion factors [101] for different body regions. DLP-derived E estimates, however, are not patient-size specific. DLP values are computed as the scanner-reported volume CT dose index ($\mathrm{CTDI}_{\mathrm{vol}}$) multiplied by irradiated scan length. $\mathrm{CTDI}_{\mathrm{vol}}$ is obtained from a 32-cm (adult body) or 16-cm (adult head, pediatric) cylindrical polymethyl methacrylate (PMMA) phantom and therefore provides only an indication of the amount of ionizing energy imparted to a phantom during a specific CT scan. Furthermore, standard mathematical phantoms used to generate the DLP conversion factors for adults ignore differences in sex, body habitus, and scanner type [72]. DLP-derived E estimates are least accurate for patients smaller (thin adults) or larger (overweight or obese adults) than the standard 32-cm phantom [49], highlighting the need for more patient-size specific dose estimates in these groups.

Patient-specific 3D anatomical dose maps have the potential to overcome some of the limitations of standard methods for estimating E, particularly DLP-based estimations. Dose maps are generated by performing MC simulations on virtual phantoms created from a patient’s own CT data rather than a standard adult reference phantom.

The primary aim of this study was to create patient-specific dose maps for estimating organ and effective doses ($E_{DoseMap}$) and compare these doses to those determined from standard DLP conversion methods (E_{DLP}) in obese adults undergoing cardiovascular CT.

10.2 Materials and Methods

This retrospective study was approved by our institutional review board with waiver of informed consent and was compliant with the Health Insurance Portability and Accountability Act. Patients were randomly selected from a database of cardiovascular CT patients to represent obese men and women over a range of body sizes. Patients with anatomy extending beyond the scanner's field of view were excluded from the study. Twenty-one obese patients (24-73 years, 10 women) with body mass index (BMI) ranging from 30 to 61 kg/m^2 were imaged for evaluation of the thoracic aorta (n = 9), pulmonary veins (n = 9), or coronary arteries (n = 3).

10.2.1 CT Imaging

For quality assurance of the CT scanner, CTDI is measured annually by a qualified medical physicist using two acrylic, cylindrical phantoms: head phantom with 16 cm diameter and body phantom with 32 cm diameter, both with a length of 14 cm. The measured CTDI is compared to the vendor-supplied CTDI displayed on the scanner console; the difference must be within a tolerance limit of +/-15%.

Data were acquired from patients after contrast injection (75-90 mL of 370 mgI/mL contrast agent [Ultravist 370, Berlex, Montville, NJ]) using prospectively electrocardiogram (ECG)-triggered axial techniques with a gantry rotation time of 280 ms on a 256-slice CT scanner (iCT, Philips Medical Systems, Cleveland, Ohio). Tube potential (100 or 120 kVp) and tube current-time product (80–295 mAs) were selected depending on patient size and imaging target (thoracic aorta, pulmonary veins, or coronary arteries). Data acquisition was prescribed at 75% of the RR interval for evaluation of the thoracic aorta and at 40% of the RR interval for evaluation of pulmonary veins. Images used for dose map creation were reconstructed with a full 500-mm field of view. $\mathrm{CTDI_{vol}}$ and DLP values, provided by the scanner and based on $\mathrm{CTDI_{vol}}$ and scan length, were recorded.

10.2.2 SSDE Determination

As previously described (in Chapter 4), AAPM described the use of size-based conversion factors to determine SSDE from the scanner-reported $\mathrm{CTDI_{vol}}$ [2]. SSDE was calculated for this study.

10.2.3 Dose Map Creation

Patient-specific dose maps displaying pixels with values representing the absorbed dose of corresponding tissue voxels were created from patient datasets using a previously validated MC simulation tool (Diagnostic Photon Simulation [DiPhoS], Philips Research, Eindhoven, Netherlands). The MC simulations were conducted on a computer (Linux) cluster with 20 CPUs and modeled the entire imaging chain including the generation of x-rays, modification of x-rays through processes such as beam shaping and filtering, and the propagation of x-ray photons through the body. Scanner configuration and acquisition parameters were extracted as input for the MC tool.

A patient-specific virtual phantom was created by voxelizing each patient's image set. Each voxel was classified as one of six material types based on fixed Hounsfield unit (HU) threshold values: air (–1000 HU), lung (–930 HU), adipose tissue (–200 HU), soft tissue (+5 HU), skeletal muscle (+40 HU), and cortical bone (+400 HU). Stoichiometry was used to compute the mass attenuation coefficient for each material type and the applied x-ray spectrum. Each voxel was assigned a mass density estimate based on its measured HU value and calculated mass attenuation coefficient [84]. The mass of tissue within a given voxel was then computed from the mass density and voxel size. A specific organ's mass was determined by integrating over all voxels contained within the organ.

A large number of photon histories (50×10^6 photons per view with 1000 views) were simulated per scan to obtain precise estimates [85]. The energy deposited in each voxel was computed and tallied in a corresponding voxelized grid [85]. The energy imparted (Joules) was divided by the mass (kg) of the irradiated tissue to determine the $\mathrm{CTDI}_{\mathrm{vol}}$-normalized absorbed dose in each voxel. Normalized absorbed dose was multiplied by the scanner-provided $\mathrm{CTDI}_{\mathrm{vol}}$ (mGy) to obtain absorbed dose (mGy).

10.2.4 Organ Segmentation

Radiosensitive organs in the scan range were manually segmented from dose maps by two consulting observers (C.T., K.Y.) to determine the average absorbed dose for each organ. Segmented organs included skin, lungs, breasts, stomach, liver, and esophagus. For organs partially exposed during a scan (e.g. stomach and liver) [81], organ dose was based on direct exposure to the portion of the organ within the scan range and indirect exposure from the tail of the dose profile to the portion of the organ outside the scan range.

10.2.5 Effective Dose Calculation

E was determined using the clinically accepted standard conversion factor (k) for the chest, 0.014 $\text{mSv} \times \text{mGy}^{-1} \times \text{cm}^{-1}$ [101]. This conversion factor was derived from organ weighting factors defined by the International Commission on Radiological Protection in publication 60 (ICRP 60) [102], multiplying k by the scanner-provided DLP then yielded: $E_{DLP} = DLP \times k$. For comparison, $E_{DoseMap\ 60}$ was determined by multiplying individual organ doses (OD) measured from dose maps by the appropriate tissue-weighting factor (w_{60}) from ICRP 60 and summing over all organs:

$$E_{DoseMap\ 60} = \Sigma OD_i \times w_{60i}. \qquad (10\text{-}4)$$

E values were also calculated on the basis of updated ICRP weighting factors from publication 103 (w_{103}) [103]. $E_{DLP\ 103}$ was determined by multiplying the scanner provided DLP by tube potential-specific conversion factors for the chest (0.0145 mSv ×

$\text{mGy}^{-1} \times \text{cm}^{-1}$ at 120 kVp and 0.0144 $\text{mSv} \times \text{mGy}^{-1} \times \text{cm}^{-1}$ at 100 kVp) proposed by Deak et al [72] using ICRP 103 tissue weighting factors. $E_{\text{Dosemap 103}}$ was determined by multiplying dose map measured organ doses by the appropriate tissue-weighting factor (w_{103}) from ICRP 103 and summing over all organs:

$$E_{\text{DoseMap 103}} = \Sigma OD_i \times w_{103i}. \qquad (10\text{-}5)$$

10.2.6 Statistical Analysis

Mean SSDE and CTDI_{vol} values were compared using a paired t-test. A significance level of 0.05 was applied. A linear regression model tested the difference between SSDE and CTDI_{vol} as a function of BMI.

A Pearson correlation coefficient was estimated to assess the linear correlation of CTDI-normalized absorbed dose for lung and breast tissues. A Bland-Altman plot was constructed to compare dose map-derived organ doses (mGy) using ICRP 103 tissue weighting factors to SSDEs.

A paired t-test was used to assess differences in $E_{\text{DLP 60}}$ and $E_{\text{DoseMap 60}}$. A significance level of 0.05 was applied. A simple linear regression model, with the difference between $E_{\text{DLP 60}}$ and $E_{\text{DoseMap 60}}$ as the dependent variable and BMI as the predictor, was used to assess the influence of BMI on the difference between these two estimation methods. The analyses were repeated to assess the difference between E values determined from $E_{\text{DLP 103}}$ and $E_{\text{DoseMap103}}$.

10.3 Results

Dose maps were created and used to determine organ and effective doses in 21 patients (Fig 10.1, Table 10.1). For each patient, dose map creation required about 3 hours using the computer cluster and segmentation of the organs required about 10 hours using a manual approach.

Table 10.1 Process of effective dose estimation for dose map method and dose-length product (DLP) conversion method in a sample patient

Dose Map Method

Organs	Absorbed Dose (mGy)	Weighting Factor $_{\text{ICRP 60}}$	Equivalent Dose $_{\text{ICRP 60}}$ (mSv)	**E $_{\text{DoseMap 60}}$ (mSv)**	Weighting Factor $_{\text{ICRP 103}}$	Equivalent Dose $_{\text{ICRP 103}}$ (mSv)	**E $_{\text{DoseMap 103}}$ (mSv)**
Lung	23.9	0.12	2.9	**8.1**	0.12	2.9	**9.3**
Breast	23.6	0.05	1.2		0.12	2.8	
Stomach	12.5	0.12	1.5		0.12	1.5	
Liver	27.0	0.05	1.4		0.04	1.1	

DLP Conversion Method

DLP (mGy x cm)	k for chest $_{\text{ICRP 60}}$ (mSv x mGy^{-1} x cm^{-1})	**E $_{\text{DLP 60}}$ (mSv)**	k for chest,120 kVp $_{\text{ICRP 103}}$ (mSv x mGy^{-1} x cm^{-1})	**E $_{\text{DLP 103}}$ (mSv)**
1018	0.014	**14.3**	0.0145	**14.8**

ICRP 60 = International Commission on Radiological Protection publication 60[19]
$E_{\text{DoseMap 60}}$ = Effective dose determined from dose maps using ICRP 60 weighting factors
ICRP 103 = International Commission on Radiological Protection publication 103 [20]
$E_{\text{DoseMap 103}}$ = Effective dose determined from dose maps using ICRP 103 weighting factors
$k_{\text{ICRP 60}}$ = Conversion factor based on weighting factors from ICRP 60[11]
$E_{\text{DLP 60}}$ = Effective dose determined from DLP conversion method using $k_{\text{ICRP 60}}$
$k_{\text{ICRP 103}}$ = Conversion factor based on ICRP 103 weighting factors[3]

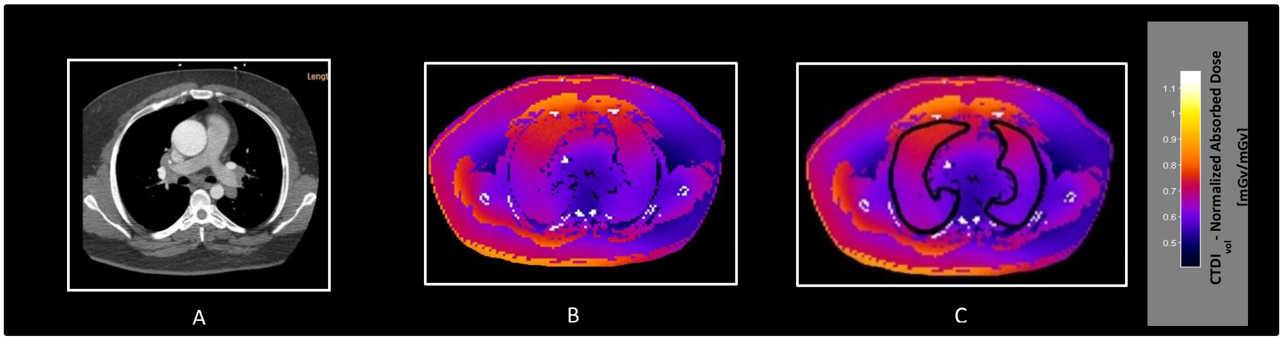

Figure 10.1: An example of an axial CT attenuation image (A), the corresponding dose map displaying volume CT dose index ($CTDI_{vol}$)-normalized absorbed dose values (mGy/mGy) (B), and dose map with lung segmentation indicated by black contours (C) for a male patient with a body mass index of 45 kg/m^2. The patient was imaged with a prospective electrocardiogram-triggered axial technique at a tube potential of 120 kV for evaluation of the thoracic aorta. The dose map shows nonuniformity (more dose accumulation on the patient's left side) because at this slice position, the x-ray tube was positioned such that x-rays entered that portion of the patient twice during the 400 degree rotation required for data acquisition.

The absolute difference between SSDE and $CTDI_{vol}$ values was < 6.4 mGy (Fig 10.2). The mean (± SD) SSDE was 20.1 (± 9.0), whereas the mean $CTDI_{vol}$ was 20.8 (± 9.4). This difference was not significant (95% CI: –1.84, 0.37; *P* = .180). The Pearson correlation coefficient (r = 0.966) indicated a strong relationship between SSDE and $CTDI_{vol}$, which was expected since $CTDI_{vol}$ was factored into the calculation. A linear regression characterized the absolute difference between SSDE and $CTDI_{vol}$ as a function of BMI. The slope estimate was small and statistically insignificant (estimate = 0.003;

95% CI: –0.12, 0.12; *P* = .965), indicating that the absolute difference between SSDE and $\mathrm{CTDI}_{\mathrm{vol}}$ was not affected by patient size.

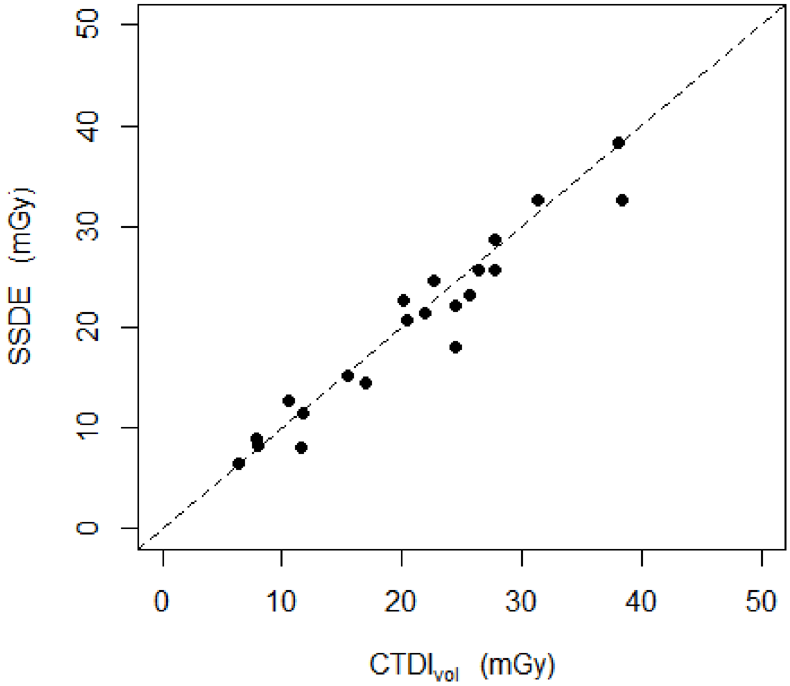

Figure 10.2: Size-specific dose estimate (SSDE) versus volume computed tomography dose index ($\mathrm{CTDI}_{\mathrm{vol}}$) with a line of symmetry showing the equivalency of these values

The observed variability of breast and lung CTDI-normalized absorbed doses among patients (Fig 10.3) was notable, as standard methods of dose estimation do not account for differences in organ dose. Normalized lung and breast doses varied by a factor of approximately 6, from 0.18 to 0.99 for the lung (between-patient SD, 0.28) and from 0.16 to 0.99 for the breast (between-patient SD, 0.26), indicating the dose maps' sensitivity to differences in organ size and tissue composition across patients. Patients' lung and breast normalized doses were correlated (r = 0.88; *P* < .001).

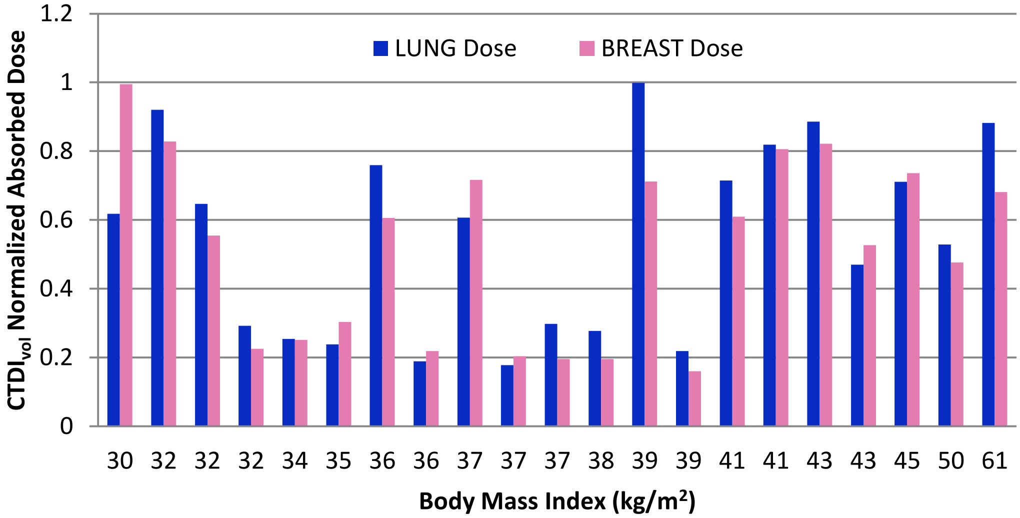

Figure 10.3: Volume computed tomography dose index (CTDI$_{vol}$)-normalized absorbed dose for lung and breast tissue plotted by body mass index demonstrates the variability in these organ doses with patient size

Comparison of dose map-derived breast and lung doses to SSDEs indicated that SSDEs were higher than the breast dose in 16 patients and higher than the lung dose in all 21 patients (Fig 10.4). The mean difference between SSDE and lung dose values was 9.10 mGy (95% CI: 5.88, 12.31; *P* < .001). The mean difference between SSDE and breast dose values was 4.07 mGy (95% CI: 0.08, 8.06; *P* = .046).

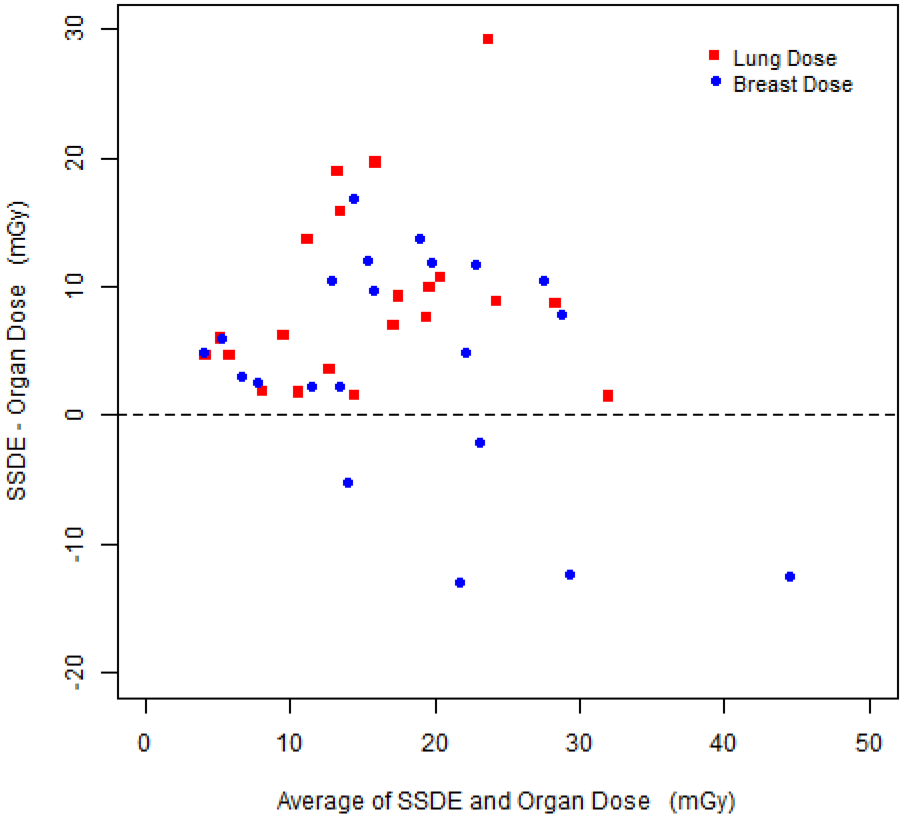

Figure 10.4: Bland-Altman plot showing lack of agreement between lung and breast absorbed doses derived from dose maps versus size-specific dose estimates (SSDEs). SSDEs tended to be higher

The DLP method provided higher doses compared to the dose map method (Fig 10.5). Mean $E_{\text{DoseMap } 60}$ was 3.4 (± 2.3) mSv, whereas mean $E_{\text{DLP } 60}$ was 5.7 (± 3.3) mSv (difference = 2.3 mSv; 95% CI: 1.2, 3.4; *P* < .001). A linear regression model did not suggest that this difference varies with BMI (slope estimate = 0.02; 95% CI: –0.15, 0.19; *P* = .825). The mean difference in E_{DLP} and E_{DoseMap} decreased slightly when estimates were based on ICRP 103 but was still differed from 0: mean $E_{DoseMap\ 103}$ was 4.0 (±2.7) mSv, whereas mean $E_{DLP\ 103}$ was 5.9 (±3.5) mSv (difference = 1.93 mSv; 95% Cl: 0.78-3.09; p=0.002). Again, a linear regression model did not suggest this difference varies with BMI (slope estimate = 0.01; 95% Cl:-0.16, 0.18; P = 0.911).

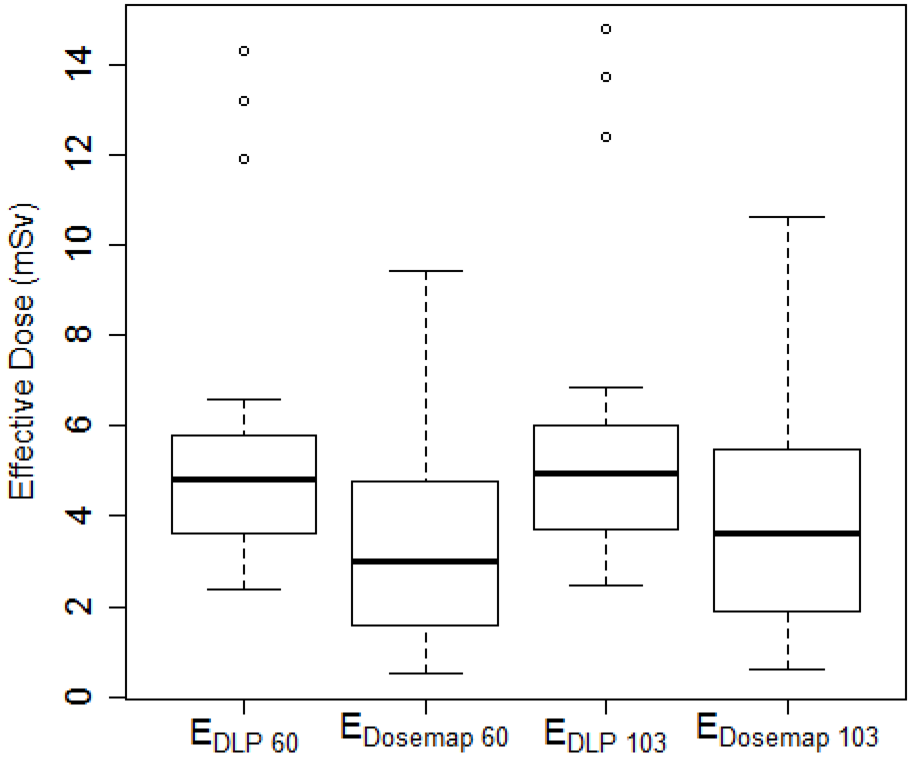

Figure 10.5**:** A box and whisker plot showing effective doses ($E_{DLP\ 60}$, $E_{DLP\ 103}$) estimated from the dose-length product using the standard conversion factor derived from the International Council on Radiation Protection [ICRP] publication 60 and updated ICRP publication 103 tended to be higher than those derived from dose maps ($E_{DoseMap\ 60}$,

$E_{DoseMap\ 103}$) using ICRP 60 and 103 weighting factors. The bottom and top of each box represent the 1st and 3rd quartiles, while the bold line represents the median. The whiskers extend to the most extreme data point which is no more than 1.5 times the interquartile range from the box and any points outside the whiskers' range (outliers) are represented by small circles

10.4 Discussion

E provides a means to express the amount of radiation a population receives from a specific CT procedure and compare that amount to radiation from other sources, both medical and non-medical. Our results showed that the standard DLP conversion method yielded higher dose estimates compared to the dose map method for estimating E in a population of obese adults. Although still different from 0, the mean dose difference decreased when updated ICRP 103 tissue weighting factors were used reflecting primarily an increase in dose map derived doses due to an increase in the tissue weighting factor for the breast from 0.05 to 0.12. Overestimation of E with the DLP method occurs in part because obese patients are larger than the 32-cm diameter phantom used to determine scanner-provided $CTDI_{vol}$ and DLP values and larger than the 70-kg reference phantom used to determine body region-specific conversion factors. Adjustments should, therefore, be applied to dose estimations for patient groups that deviate from these standard sizes.

Other groups have highlighted the dependency of DLP to E conversion factors on patient size. Deak et al derived sex-, age-, and tube potential- specific conversion factors for the chest using Monte Carlo methods to simulate scanning of mathematical phantoms representing children and non-obese adults on a 64-slice CT scanner. For a non-obese adult, the standard conversion factors for the chest ranged between 0.0135 and 0.0138 mSv × mGy^{-1} × cm^{-1} based on tissue- weighting factors from ICRP 60 and 0.0144 and 0.0147 mSv × mGy^{-1} × cm^{-1} based on factors from ICRP 103, close to the current single reference value of 0.014 mSv × mGy^{-1} × cm^{-1}. However, the appropriate conversion factor for the chest increased with decreasing patient size with values for newborns based on tissue-weighting factors from ICRP 60 to 103 ranging from 0.0634 to 0.0823 mSv × mGy^{-1} × cm^{-1}. Following the same logic, the appropriate conversion factor for the chest should decrease with increasing patient size. Using whole body computational phantoms created from clinical CT images of normal weight (n=3) and obese (n=3) adults, Li et al [104] demonstrated k factors used to estimate E for the chest should be reduced for obese compared to non-obese men and women and further noted that the appropriate conversion coefficients cannot be predicted using body diameter alone. Einstein et al further demonstrated the dependency of DLP to E conversion factors on the specific scanner technology and specific region-of-interest (e.g. cardiac versus chest) (19). Dose maps inherently account for differences in patient and organ sizes, scanner technology and irradiated organs and tissues.

The AAPM attempted to capture the dependency of patient dose on patient size by developing a patient size-based modification to the scanner-provided $CTDI_{vol}$ [2]. The report provided correction factors based on a patient’s estimated effective diameter [2]. Our patients had an average effective diameter of 36.5 cm, corresponding to an average normalized dose coefficient close to 1. This correction factor yielded SSDEs that were not significantly different from original CTDI_{vol} values, suggesting that improved dosimetry accuracy may not be realized for obese patients using this approach, perhaps because organ size and tissue differences are not taken into account. Although computation of SSDEs did not seem to account for size differences in our patients for thoracic CT, SSDE has been shown to account for patient size well in dose estimation for abdominopelvic CT [105].

MC methods using well-established cylindrical and physical phantoms, mathematical models (stylized) [68, 72, 94, 106-109], voxel models (tomographic) [67, 70, 71, 73, 81, 95, 100, 108, 110], and hybrid models [49, 51, 111, 112] have been used to estimate CT dose. However, mathematical models do not consider variabilities in patient size and organ size and shape; they contain fixed geometric anatomic shapes characterized by equations. The positions of organs in mathematical models can also be unrealistic [107] and contribute to overestimation or underestimation of doses. Inaccuracies in model dose estimates also stem from modeling body composition. Organ doses in adolescent patients assessed using stylized hermaphrodite phantoms and hybrid phantoms differed by up to 2-fold; hybrid phantoms permitted more accurate modeling of body composition [49].

Dose estimation is also possible from voxelized models of CT images [70, 71, 73, 78, 113]. Schmidt and Kalender [73] developed a MC method that yielded doses from voxelized CT images of anthropomorphic phantoms that differed < 5% from CTDI results obtained with a standard MC-based program (EGS4) and published organ dose conversion factors. DeMarco et al [71] showed good agreement between dose estimated from MC methods applied to voxelized images of cylindrical body and anthropomorphic phantoms compared with dose determined from physical phantoms using metal-oxide semiconductor field effect transistors (MOSFETs). Deak et al [70] found that calculated dose values from 3D dose distributions of voxelized phantom images were within 10% of phantom measurements (Alderson-Rando and cylindrical CTDI) using thermoluminescent dosimeters (TLDs). In our study, we created dose maps by voxelizing each patient's CT images, providing a more patient-specific approach compared to previous studies.

Individual organ doses also contribute to E and can be used to assess radiation risk from diagnostic imaging procedures. Unlike DLP-derived dose estimates, MC simulation permits organ dose estimation. However, differences between models and actual patients, as well as variations in scanner geometries and X-ray beam spectra, contribute to inaccuracies in organ dose estimation [74, 78]. Our approach is sensitive to these differences; we demonstrated variability in normalized absorbed doses to highly radiosensitive organs (breast and lung) across patients.

Our method of organ and E estimation did have limitations. A 400-HU threshold was used to classify highly attenuating tissue (including contrast-enhanced blood) as bone, and subsequent MC simulations and stoichiometry assumptions were based on this tissue classification. The significance of this on dose estimation is currently under investigation. Another limitation was manual organ segmentation. Automatic organ segmentation would reduce data analysis time and possibly produce more accurate organ doses through objective differentiation of organs and tissues based on a tissue classification rubric. Additionally, the method used to calculate equivalent dose to partially irradiated organs was limited by the need to assume a total length for the organ.

Also, a larger patient population could strengthen our conclusion; however, including additional patients is difficult because of the intensive MC calculations currently required to create patient-specific dose maps. Finally, only one clinical scanner was studied.

10.5 Conclusion

In conclusion, anatomic dose maps created from patient CT images enable more scanner- and patient-size specific estimation of organ and E and provide lower dose estimates for obese patients undergoing cardiovascular CT procedures than standard E estimation methods based on the scanner-provided DLP. Considering patient size, organ size, and the composition of irradiated tissue could lead to better metrics for CT dose management, particularly for obese patients

CHAPTER XI

CONTRAST STUDY

A Preliminary Study using Patient-specific Dose Maps to Quantify CT Radiation Dose in the Presence of Iodinated Contrast

11.1 Introduction

Administration of iodinated contrast media (CM) is a critical component of computed tomography angiography (CTA) because enhancement of the vessels allows angiographic visualization of the vessel luminal detail. The local x-ray absorption coefficient of a tissue or material is dependent on its electron density and effective atomic number (Z). Iodine (Z=53) is the optimal choice for water-soluble imaging agents because it forms soluble compounds with low toxicity and its high atomic number allows it to absorbs more x-rays, and thus, appears brighter on the CT image than soft tissue [13, 114].

Iodine can accumulate at different concentrations when injected in the body. The quantity of iodine accumulated in the great vessels and organs at the time of scan as well as organ shape, volume, and position within the body [3, 4] determines x-ray absorption during the CT scan. Unlike traditional dose descriptors (volume CT dose index [$CTDI_{vol}$], dose-length product [DLP]) , patient-specific dose maps generated from patient images using Monte Carlo simulations are sensitive to the presence of iodinated CM during a CT scan [3, 4]. Patient-specific dose maps display pixels with values representing the absorbed dose of corresponding tissue voxels.

The aim of this study was to determine if patient-specific dose maps demonstrate differences in absorbed dose to organs in the chest, abdomen, and pelvis before and after administration of iodinated CM. The methods used to quantify radiation dose in the presence of iodinated contrast are discussed along with preliminary results.

11.2 Materials and Methods

This study was approved by our institutional review board with waiver of informed consent and was compliant with the Health Insurance Portability and Accountability Act. Patients were randomly selected from a database of CT patients to represent men and women of different ages with a range of body sizes. The chest, abdomen, and pelvis of ten patients (37-86 years, 4 women) with body mass index (BMI) ranging from 24-38 kg/m^2 were imaged for evaluation before or after endovascular stent graft repair.

11.2.1 CT Imaging

Patients were imaged with a non-gated helical technique during a non-contrast, arterial, and venous phase. Arterial phase scanning was triggered when peak attenuation was reached in the descending aorta just after the administration of 80 mL of 350 mgl/mL CM (Omnipaque 350, Berlex, Montville, NJ). CTDI$_{vol}$ and DLP values provided by the scanner were recorded. Identical scan parameters were chosen for non-contrast and arterial phase scanning for a given patient; the tube current-time product was lowered during the venous phase. Images used for dose map creation were reconstructed with a full 500-mm field of view.

11.2.2 Attenuation Measurements

Average attenuation was measured by drawing a region of interest (ROI) on three consecutive CT slices for each patient in select organs (stomach, liver, pancreas, spleen, and kidneys) during each phase (non-contrast, arterial, and venous).

11.2.3 Dose Map Creation

Patient-specific dose maps were created from non-contrast and arterial phase patient datasets using a previously validated Monte Carlo simulation tool (Diagnostic Photon Simulation [DiPhos], Philips Research, Eindhoven, Netherlands). MC simulations modeled the entire imaging chain including the generation of x-rays, modification of x-rays through processes such as beam shaping and filtering, and the propagation of x-rays photons through the body.

A patient-specific virtual phantom was created by voxelizing each patient's non-contrast and arterial phase image sets. Each voxel was classified as one of 26 material types based on tube potential-specific, fixed Hounsfield Unit (HU) threshold values (Table 11.1). Stoichiometries and densities were modeled from chemistry and the appropriate International Commission on Radiation Units and Measurements (ICRU) body material recommendations. Although bone was included in the body material recommended, it was omitted from the tissue scheme because its tissue weighting factor is negligible. The new tissue scheme includes blood/contrast mixtures from 100% blood to 20% contrast + 80% blood.

Material Type	Attenuation Threshold at 100 kVp (HU)	Attenuation Threshold at 120 kVp (HU)
Air	-1000	-1000
Lung Tissue	-930	-930
Adipose Tissue	-200	-200
Water	-5	-5
Soft Tissue	5	5
Blood (100%)	62	60
Blood (99%) + Contrast media (CM) (1%)	137	125
Blood (98%) + CM (2%)	282	251
Blood (97%) + CM (3%)	427	377
Blood (96%) + CM (4%)	571	502
Blood (95%) + CM (5%)	715	627
Blood (94%) + CM (6%)	860	753
Blood (93% + CM (7%)	1005	879
Blood (92%) + CM (8%)	1150	1005
Blood (91%) + CM (9%)	1294	1130
Blood (90%) + CM (10%)	1439	1256
Blood (89%) + CM (11%)	1584	1381
Blood (88%) + CM (12%)	1727	1506
Blood (87%) + CM (13%)	1872	1632
Blood (86%) + CM (14%)	2017	1758
Blood (85%) + CM (15%)	2162	1884
Blood (84%) + CM (16%)	2307	2010
Blood (83) + CM (17%)	2451	2134
Blood (82) + CM (18%)	2596	2260
Blood (81) + CM (19%)	2741	2386
Blood (80) + CM (20%)	2884	2511

Table 11.1: Material classification scheme for voxelizing patient images for each tube potential

Stoichiometry was used to compute the mass attenuation coefficient for each material type and the applied x-ray spectrum. Each voxel was assigned a mass density estimate based on its measured HU value and calculated mass attenuation coefficient [84]. The mass of tissue within a given voxel was then computed from the mass density and voxel size. A specific organ's mass was determined by integrating over all voxels contained within the organ.

For each virtual phantom, the paths of individual X-ray photons through the irradiated tissue were modeled with MC methods based on known physical interactions (Rayleigh scattering, Compton effect, photoelectric effect) [85]. A large number of photon histories (50×10^6 photons per view with 1000 views) were simulated per scan to obtain precise estimates [85]. The energy deposited in each voxel was computed and tallied in a corresponding voxelized grid [85]. The energy imparted (Joules) was divided by the mass (kg) of the irradiated tissue to determine the $\mathrm{CTDI}_{\mathrm{vol}}$-normalized absorbed dose in each voxel. Normalized absorbed dose was multiplied by the scanner-provided $\mathrm{CTDI}_{\mathrm{vol}}$ (mGy) to obtain absorbed dose (mGy).

11.2.4 Organ Segmentation

Radiosensitive organs in the scan range were manually segmented from dose maps by two consulting observers (CT, PS) to determine the average absorbed dose for each organ. Segmented organs included skin, lungs, breasts, stomach, liver, esophagus, kidneys, pancreas, and spleen.

11.2.5 Effective Dose Estimation

Effective dose (E) in the non-contrast and arterial phases were calculated on the basis of updated International Council on Radiological Protection (ICRP) weighting factors from publication 103 (w_{103}) [103]. $E_{Dosemap\ 103}$ was determined by multiplying dose map-measured organ doses by the appropriate tissue-weighting factor (w_{103}) from ICRP 103 and summing over all organs:

$$E_{DoseMap\ 103} = \Sigma OD_i \times w_{103i}. \tag{11-1}$$

11.2.6 Statistical Analysis

E values calculated from the dose map method were compared in the non-contrast and arterial phase using a paired t-test. The absorbed dose to seven select organs was also compared in the non-contrast and arterial phases using a paired t-test. A significance level of 0.05 was used for all comparisons. A simple linear regression model, with the difference in $E_{Dose\ Map\ 103}$ between the arterial and non-contrast phases as a function of BMI was used to assess the influence of BMI on the difference in estimated dose between these two phases.

11.3 Preliminary Results

Attenuation increased for all evaluated organs in the arterial phase. The mean increase in attenuation was 11 HU in the stomach (95% CI: 3, 20 HU; $p=0.018$), 6 HU in the liver (95% CI: 2, 11 HU; $p=0.015$), 34 HU in the pancreas (95% CI: 22, 46 HU; $p<0.001$), 45 HU in the spleen (95% CI: 25, 65 HU; $p=0.001$), and 61 in the kidneys

(95% CI: 40, 81 HU; p<0.001). A higher attenuation is observed in the venous (Fig 11.1). Compared to the non-contrast phase, the mean increase in attenuation was 25 HU in the stomach (95% Cl: 17, 34 HU; p<0.001), 25 HU in the liver (95% Cl: 18, 32 HU; p<0.001), 30 HU in the pancreas (95% Cl: 17, 44 HU p=0.001), 30 HU in the spleen (95% Cl: 22, 38 HU p<0.001), and 88 HU in the kidneys (95% Cl: 65, 112 HU; p<0.001) during the venous phase.

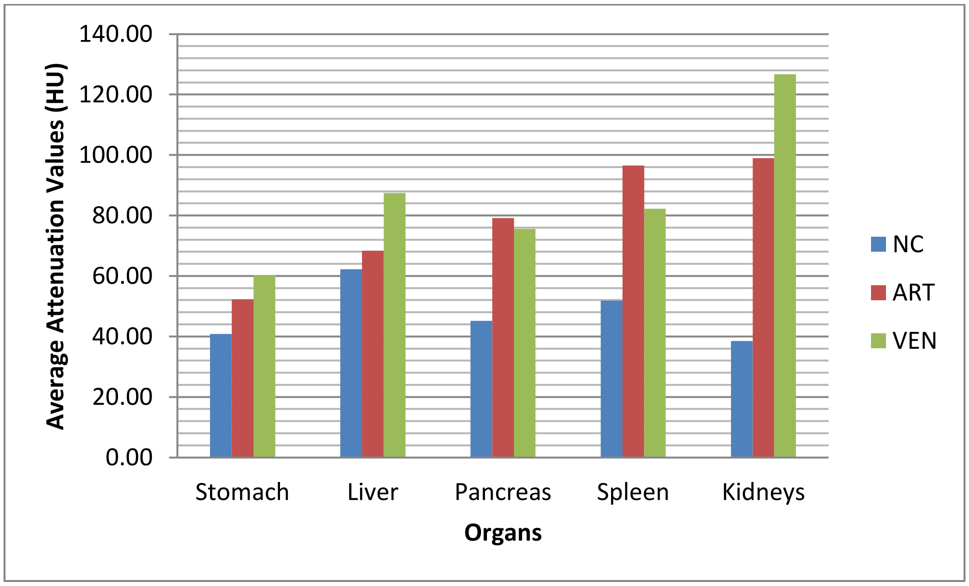

Figure 11.1: Average attenuation values (Hounsfield Units) in selected organs during non-contrast, arterial, and venous phases.

Out of five organs assessed (Table 11.2) only the kidneys and pancreas showed a significant difference in absorbed dose between non-contrast and the arterial phases: the dose absorbed by the kidneys (14.7 vs. 13.4 mGy; 95% CI for the difference: 0.36, 2.30; p=0.013) and pancreas (13.8 vs. 13.2 mGy; 95% CI for the difference: 0.17, 1.13; p=0.014) was significantly higher in the arterial phase. No significant correlation was observed between the difference in absorbed dose from the non-contrast to arterial phase and patient BMI (Fig 11.2).

Organ	Absorbed dose for non-contrast phase (mGy)	Absorbed dose for arterial phase (mGy)	Difference between phases	95% Confidence Interval	P value
Stomach	12.8	12.9	0.05	(-0.74, 0.84)	0.889
Liver	14.1	14.3	0.18	(-0.18, 0.54)	0.285
Kidneys	13.4	14.7	1.33	(0.36, 2.30)	0.013
Pancreas	13.2	13.8	0.65	(0.17, 1.13)	0.014
Spleen	15.8	17	1.24	(-0.39, 2.87)	0.119

Table 11.2: A comparison of mean absorbed dose for select organs in the non-contrast and arterial phases. A significant difference in dose between phases was only observed for the kidneys and pancreas.

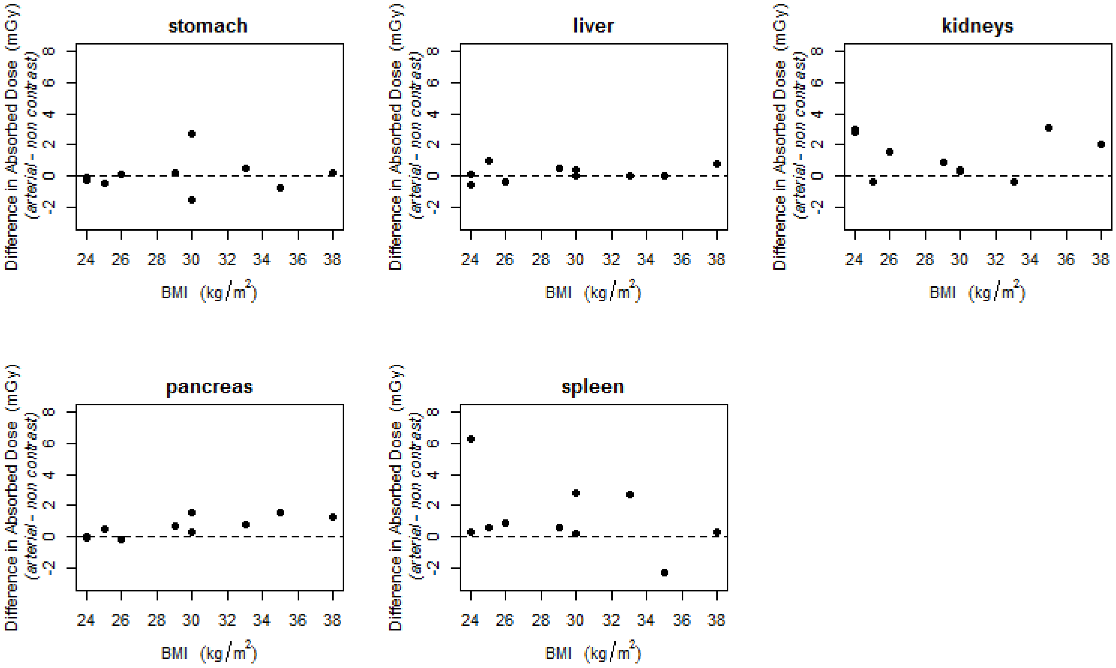

Figure 11.2: The difference in absorbed dose from the dose map method ($E_{\text{Dose Map 103}}$) between the arterial and non-contrast phases as a function of BMI (body mass index). The dotted line represents the dose difference that is equal to zero.

$E_{\text{DoseMap103}}$ was slightly higher during the arterial phase compared to the non-contrast phase (11.3 vs. 11.2 mSv; 95% CI for the difference: -0.35, 0.69; p=0.475). The difference in $E_{\text{DoseMap103}}$ between the non-contrast and arterial phases was not affected by patient size (slope: -0.01, p=0.862). (Fig 11.3)

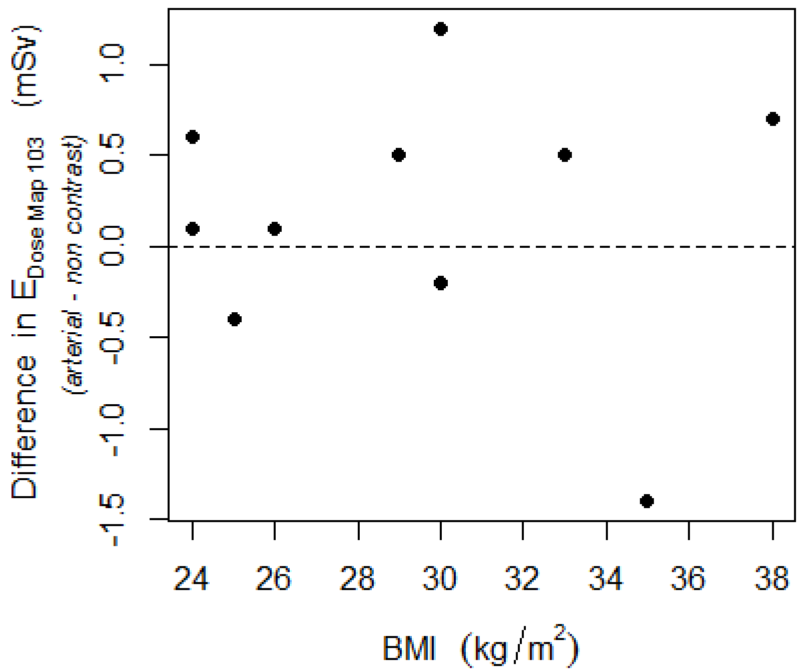

Figure 11.3: The difference in effective dose (E) between the arterial and non-contrast phases estimated using the dose map method ($E_{\text{DoseMap 103}}$) as a function of BMI (body mass index). The solid line (best fit line) represents the linear model of how the

difference in E between the two phases changes with BMI and the dotted line represents the dose difference that is equal to zero.

11.4 Discussion

Our results demonstrate that patient-specific dose maps can evaluate organ doses before and after administration of iodinated CM. E was marginally higher in the arterial phase compared to the non-contrast phase. This difference did not correlate with patient BMI.

Only the absorbed dose for the kidneys and pancreas were significantly higher in the arterial phase compared to the non-contrast phase. Measured attenuation differences between the non-contrast and venous phases suggest we might expect to see an increase in organ dose for the kidneys, liver, and stomach in the venous phase.

Amato et al [4] assessed the measured HU increase and the corresponding radiation dose increment in the organs of 40 patients who underwent CT before and after contrast administration during the venous phase. Results showed an average organ dose increase of 71% for kidneys, 41% for the thyroid, and 33% for the spleen and pancreas [4] which reflects the timing of the scan relative to CM injection. Iodinated CM was released 80 seconds after the start of contrast administration. The relationship between HU increment and radiation dose increase was derived from previous work where Monte Carlo (MC) methods were performed on an anthropomorphic phantom with iodinated organs [3]. Organs, characterized as ellipsoidal shapes were assumed for the geometrical input of the MC code.

Although, Hounsfield-based determination of radiation is simple and quick, the method only utilizes information from a region of interest in select organs. Dose maps assess the entire organ and account for organ size and shape as well as position within the body. Dose maps also account for the effect of nearby iodine filled vessels on organ dose.

Our study did have limitations. The patient population was small because of the intensive MC calculations required to create patient-specific dose maps. Also, we only evaluated a single time point, shortly after contrast was injected; venous phase dose maps were not evaluated because of differences in applied radiation. In our comparison of absorbed dose between non-contrast and arterial phases, we did not account for differences in the starting position of the x-ray tube which certainly influenced dose along with the differences in the presence of contrast. Our results may also have been limited by manual organ segmentation. Automatic organ segmentation might provide more consistency in segmentation between phases for an individual.

Future work should include creation and evaluation of arterial and venous phase dose maps with the same input parameters (e.g., x-ray tube starting angle and x-ray tube current) as the non-contrast phase. This should ensure that measured differences in dose are only the result of differences in the presence of contrast agent in the vessels and organs among scans.

11.5 Conclusion

Patient-specific dose maps may have an advantage over traditional dose descriptors ($CTDI_{vol}$ and DLP) because they account for the presence of contrast agent in the great vessels and organs during a CT exam. Dose maps evidenced increased dose during arterial phase imaging of the adult chest, abdomen, and pelvis compared to non-contrast phase imaging.

CHAPTER XII

CONCLUSIONS

The growth of CT over the last 15 years has led to improved patient outcomes for the diagnosis of a wide range of clinical indications [115]. Proper indication, appropriate protocols, and scanner technology have resulted in decreased radiation exposure for individual scans. However, providing accurate dose estimates from a CT exam is still a major concern for clinical researchers so a strong desire remains to quantify dose especially radiation exposure to radiosensitive organs.

The aim of this research was to evaluate the utility of patient-specific dose maps for CT exams. Patient-specific dose maps offers to overcome the current limitations of inaccurate dose estimation with standard dose descriptors. Standard dose descriptors do not take in account patient specific anatomy which leads to inaccurate dose estimates. It was shown that estimating dose will lead to either to an over -or underestimation especially for patients who are smaller or larger than 32-cm Plexiglas phantom. Patient size, individual organ size, and body composition should be accounted for to help improve the accuracy of dose estimation methods.

Computational phantoms offer a more realistic approach than physical phantoms. Voxel phantoms use the patient's own CT images to capture the anatomical and organ differences in patients by modeling complex attenuating volumes. MC methods provide a powerful computational tool that can be used to simulate ionizing radiation for dosimetry in computational phantoms using known probabilities of occurrence [using random sampling of probability density functions for each event] to model the system. Most importantly, MC methods are attractive because of the possibility to estimate physical parameters that are difficult or impossible to calculate using experimental measurements and physical phantoms. The benefits of using MC in radiation transport enables optimization of instrumentation design and estimation of absorbed dose distributions for diagnostic exams or radiation treatment [86].

Validation of a MC tool with an anthropomorphic phantom is a preferred approach because these phantoms allow direct dose assessment. Organ dose can be directly measured with either TLDs or MOSFETs. Although, TLDs and MOSFETs are both beneficial for direct dose assessment; the process can be costly and time-consuming. Chapter IX showed the validation of dose maps where MOSFETs proved to an excellent choice because of their high spatial resolution and immediate dose readouts. The accuracy of dose calculations were tested by using the MC (DiPhos) simulation tool performed on an anthropomorphic phantom compared to MOSFET dosimeters placed inside the phantom. Results showed radiation dose estimates from DiPhos were strongly correlated with MOSFETs measurements in a physical adult and infant anthropomorphic phantom for a range of CT protocols. However, the average ratio between MOSFET and MC results for female axial cardiac scans were about 5-10% higher than the expected value of 1.00 which possibly indicates a problem with the MC simulations. The source of the error is not readily apparent especially when we would expect to see a similar effect in the other protocols. Also, the infant chest/abdomen scans had a lower average ratio than expected but were correct in the head and shoulder region. It is believed that these errors are called systemic errors and stem from modeling of the scanning procedure. Additional measurements are required to identify the specific source of these errors.

E reflects the relative biological sensitivity of irradiated organs and tissues. It also allows comparison of the biological effect between specific CT exams. Computing E_{DLP} provides a generic approach to estimating E and it is especially apparent for obese patients as shown in Chapter X. Dose maps derived from patient CT images yielded lower E estimates than the DLP conversion method. This overestimation of E with the DLP method occurred in obese patients who are larger than the 32-cm diameter phantom that is used to determine scanner-provided $CTDI_{vol}$ and DLP values and also larger than the standard 70 kg reference phantom that is used to determine body region-specific conversion factors. Adjustments have to be made to dose estimation methods to account for patient groups that deviate from standard sizes. The introduction of SSDE was an improvement because it provided correction factors based on the estimated effective diameter of a patient. However, results showed that SSDE was not significantly different from original $CTDI_{vol}$ values suggesting that the improved dose descriptor might not be an option for obese patients because organ size and tissue differences are not taken into account. It is evident that these dose descriptors are poor indicators of dose. Dose maps provide a more accurate approach by enabling more scanner- and patient-size specific estimation of organ and effective doses which provided lower dose estimates for obese patients undergoing cardiovascular CT procedures.

Following the results in Chapter X, a new method that accounted for the presence of contrast media was used to create patient-specific dose maps. Results in Chapter XI showed that dose maps can account for to the presence of contrast agent in the great vessels and organs during scanning. The presence of contrast was shown to yield a slight increase in effective dose in the arterial phase compared to the non-contrast phase in an adult, chest, abdomen, and pelvis protocol. This sensitivity to the presence of contrast agent gives patient-specific dose maps an additional advantage over standard dose descriptors [4].

Overall, a couple of limitations hinder the clinical adoption of MC tools. One major limitation is the intensive computation required for MC methods to efficiently model a system. Another limitation is the statistical uncertainties in the estimates. One way to decrease the statistical uncertainty is to run MC simulations for a sufficiently long time to generate a large number of photon histories and use efficient variance reduction techniques [86].

The work presented in this dissertation has raised a couple of interesting research questions that should be addressed in the future. Will on-site patient-specific dose maps be a viable clinical option? As previously mentioned, the heavy burden of MC calculations is a limitation. This question is of great interest because MC methods provide an accurate and realistic evaluation of dose assessment. Graphics processing units (GPUs) are highly parallel coprocessors which functions to decrease the computational demand [113]. A large number of datasets can be processed in parallel to achieve high performance. One advantage of using multiple GPUs is the use of separate memory. One group developed a MC tool that provides on-site dose distributions using multiple GPUs [113]. Implementing multiple GPUs would enable on-site dose maps to be created from scout images. Obtaining faster dose maps would allow clinical scientists to use the information from dose maps to plan patient scanning. This provides a prominent solution to compensate for the intensive computations required to accurately model a CT system and patient.

Will dose maps have a significant role in pediatric dose estimation? This dissertation focused only on adult CT dose estimation, but it would be interesting to see what type of benefits the patient-specific dose maps could potentially provide for the pediatric population. Accurately estimating dose for this group is extremely important especially since they have a greater organ radiosensitivity and a longer lifespan [116].

In conclusion, this research has shown that patient-specific dose maps have the ability to characterize, estimate E, and organ dose to a patient, and also quantify radiation dose a patient receives from a contrast-enhanced CT exam. As more dose maps are created, the next step would entail creating a library of dose maps from other patients. Therefore, when a patient comes into the hospital to be scanned, the operator would find the best matched dose map (from the library) to the current patient. These options would allow dose maps to be used appropriately by adjusting the scan protocol without compromising image quality for patients of all sizes. Although initial results look promising, a larger patient population is necessary. Computation intensive MC is a limitation but incorporating multiples GPUs would allow faster computation of dose maps to be created from scout images of patients making it a clinical option in the near future.

REFERENCES

1. Kalra, M.K., et al., *Radiation exposure from chest CT: issues and strategies.* J Korean Med Sci, 2004. **19**(2): p. 159-66.
2. *American Association of Physicists in Medicine. Size-Specific Dose Estimates (SSDE) in Pediatric and Adult Body CT Examinations (Task Group 204)*. 2011, American Association of Physicists in Medicine: College Park, MD.
3. Amato, E., et al., *A method to evaluate the dose increase in CT with iodinated contrast medium.* Med Phys, 2010. **37**(8): p. 4249-56.
4. Amato, E., et al., *Can contrast media increase organ doses in CT examinations? A clinical study.* AJR Am J Roentgenol, 2013. **200**(6): p. 1288-93.
5. Bushberg, J.T., et al., *The Essential Physics of Medical Imaging*. Second ed. 2001, Philadephia: Lippincott Williams & Wilkins. 960.
6. Tonnessen, B.H. and L. Pounds, *Radiation physics.* J Vasc Surg, 2011. **53**(1 Suppl): p. 6S-8S.
7. Singh, S., et al., *Radiation dose optimization and thoracic computed tomography.* Radiol Clin North Am, 2014. **52**(1): p. 1-15.
8. Seibert, J.A. and J.M. Boone, *X-ray imaging physics for nuclear medicine technologists. Part 2: X-ray interactions and image formation.* J Nucl Med Technol, 2005. **33**(1): p. 3-18.
9. Halliburton, S.S., et al., *SCCT guidelines on radiation dose and dose-optimization strategies in cardiovascular CT.* J Cardiovasc Comput Tomogr, 2011. **5**(4): p. 198-224.
10. Goldman, L.W., *Principles of CT and CT technology.* J Nucl Med Technol, 2007. **35**(3): p. 115-28; quiz 129-30.
11. Hathcock, J.T. and R.L. Stickle, *Principles and concepts of computed tomography.* Vet Clin North Am Small Anim Pract, 1993. **23**(2): p. 399-415.
12. Halliburton, S., et al., *State-of-the-art in CT hardware and scan modes for cardiovascular CT.* J Cardiovasc Comput Tomogr, 2012. **6**(3): p. 154-63.
13. Harvey, C.J., *Principles of radiology.* Surgery (Oxford), 2008. **26**(6): p. 235-238.
14. Bae, K.T., *Intravenous Contrast Medium Administration and Scan Timing at CT: Considerations and Approaches.* Radiology, 2015. **256**(1): p. 32-61.
15. Bauhs, J.A., et al., *CT dosimetry: comparison of measurement techniques and devices.* Radiographics, 2008. **28**(1): p. 245-53.
16. Jessen, K.A., et al., *Dosimetry for optimisation of patient protection in computed tomography.* Appl Radiat Isot, 1999. **50**(1): p. 165-72.
17. McCollough, C.H., et al., *CT dose index and patient dose: they are not the same thing.* Radiology, 2011. **259**(2): p. 311-6.
18. Shope, T.B., R.M. Gagne, and G.C. Johnson, *A method for describing the doses delivered by transmission x-ray computed tomography.* Med Phys, 1981. **8**(4): p. 488-95.
19. Lee, C.H., et al., *Radiation dose modulation techniques in the multidetector CT era: from basics to practice.* Radiographics, 2008. **28**(5): p. 1451-9.
20. Suzuki, A. and M.N. Suzuki, *Use of a pencil-shaped ionization chamber for measurement of exposure resulting from a computed tomography scan.* Med Phys, 1978. **5**(6): p. 536-9.
21. *The Measurement, Reporting, and Managment of Radiation Dose in CT. Report of AAPM Task Group 23 of the Diagnostic Imaging Council CT Committee. Report No. 96*. 2008: College Part, MD. p. 1-28.
22. Gerber, T.C., B. Kantor, and C.H. McCollough, *Radiation dose and safety in cardiac computed tomography.* Cardiol Clin, 2009. **27**(4): p. 665-77.

23. Schoepf, U.J. and C. McCollough, *Radiation Dose From CT of the Heart*, in *CT of the Heart*. 2005, Humana Press. p. 63-68.

24. Shrimpton, P.C., *Assessment of Patient Dose in CT. Appendix C, European Guidelines for Multislice Computed Tomography. Funded by the European Commission; 2004. Contract No. FIGM-CT-2000-20078-CT-TIP.*

. 2004.

25. Brenner, D.J. and E.J. Hall, *Computed tomography--an increasing source of radiation exposure.* N Engl J Med, 2007. **357**(22): p. 2277-84.

26. *4. Overview of Existing CT-Dosimetry Methods.* Journal of the ICRU, 2012. **12**(1): p. 35-45.

27. McCollough, C.H., *Patient dose in cardiac computed tomography.* Herz, 2003. **28**(1): p. 1-6.

28. Huda, W. and F.A. Mettler, *Volume CT dose index and dose-length product displayed during CT: what good are they?* Radiology, 2011. **258**(1): p. 236-42.

29. Huda, W. and G.A. Sandison, *CT Dosimetry and Risk Estimates.* Radiat Prot Dosimetry, 1985. **12**(3): p. 241-249.

30. Angel, E., et al., *Dose to radiosensitive organs during routine chest CT: effects of tube current modulation.* AJR Am J Roentgenol, 2009. **193**(5): p. 1340-5.

31. Huda, W. and J.V. Atherton, *Energy imparted in computed tomography.* Med Phys, 1995. **22**(8): p. 1263-9.

32. Brady, Z., T.M. Cain, and P.N. Johnston, *Comparison of organ dosimetry methods and effective dose calculation methods for paediatric CT.* Australas Phys Eng Sci Med, 2012. **35**(2): p. 117-34.

33. *Chapter 3 Physiological data for reference man.* Annals of the ICRP/ICRP Publication, 1975. **23**(0): p. 335-365.

34. Caon, M., *Voxel-based computational models of real human anatomy: a review.* Radiat Environ Biophys, 2004. **42**(4): p. 229-35.

35. McCollough, C.H., J.A. Christner, and J.M. Kofler, *How effective is effective dose as a predictor of radiation risk?* AJR Am J Roentgenol, 2010. **194**(4): p. 890-6.

36. Goldman, L.W., *Principles of CT: radiation dose and image quality.* J Nucl Med Technol, 2007. **35**(4): p. 213-25; quiz 226-8.

37. Lee, C., et al., *Organ doses for reference adult male and female undergoing computed tomography estimated by Monte Carlo simulations.* Medical Physics, 2011. **38**(3): p. 1196-1206.

38. Hurwitz, L.M., et al., *Effective dose determination using an anthropomorphic phantom and metal oxide semiconductor field effect transistor technology for clinical adult body multidetector array computed tomography protocols.* J Comput Assist Tomogr, 2007. **31**(4): p. 544-9.

39. Winslow, J.F., et al., *Construction of anthropomorphic phantoms for use in dosimetry studies.* J Appl Clin Med Phys, 2009. **10**(3): p. 2986.

40. Einstein, A.J., et al., *Radiation dose from single-heartbeat coronary CT angiography performed with a 320-detector row volume scanner.* Radiology, 2010. **254**(3): p. 698-706.

41. http://www.cirsinc.com/products/modality/33/atom-dosimetry-verification-phantoms/. *ATOM Dosimetry Verification Phantoms*. [cited.

42. Han, E.Y., W.E. Bolch, and K.F. Eckerman, *Revisions to the ORNL Series of Adult and Pediatric Computational Phantoms for use with the MIRD Schema.* Health Phys, 2006. **90**(4): p. 337-356.

43. Lee, C. and J. Lee, *Computational anthropomorphic phantoms for radiation protection dosimetry: evolution and prospects.* NET, 2006. **38**(3): p. 239-250.
44. McCollough, C.H. and B.A. Schueler, *Calculation of effective dose.* Med Phys, 2000. **27**(5): p. 828-37.
45. Caon, M., G. Bibbo, and J. Pattison, *A comparison of radiation dose measured in CT dosimetry phantoms with calculations using EGS4 and voxel-based computational models.* Phys Med Biol, 1997. **42**(1): p. 219-29.
46. Zanki, M., *Methods for Assessing Organ Doses using Computational Models.* Radiat Prot Dosimetry, 1998. **80**(1-3): p. 207-212.
47. Bolch, W., et al., *Hybrid computational phantoms for medical dose reconstruction.* Radiat Environ Biophys, 2010. **49**(2): p. 155-68.
48. Zanki, M., *Computational Models Employed for Dose Assessment in Diagnostic Radiology.* Radiat Prot Dosimetry, 1993. **49**(1/3): p. 339-344.
49. Lee, C., et al., *Hybrid computational phantoms of the 15-year male and female adolescent: applications to CT organ dosimetry for patients of variable morphometry.* Med Phys, 2008. **35**(6): p. 2366-82.
50. Kim, K.P., et al., *Development of a database of organ doses for paediatric and young adult CT scans in the United Kingdom.* Radiat Prot Dosimetry, 2012. **150**(4): p. 415-26.
51. Hurtado, J.L., et al., *Hybrid computational phantoms representing the reference adult male and adult female: construction and applications for retrospective dosimetry.* Health Phys, 2012. **102**(3): p. 292-304.
52. DeWerd, L.A. and L.K. Wagner, *Characteristics of radiation detectors for diagnostic radiology.* Appl Radiat Isot, 1999. **50**(1): p. 125-36.
53. McNitt-Gray, M.F., *AAPM/RSNA Physics Tutorial for Residents: Topics in CT. Radiation dose in CT.* Radiographics, 2002. **22**(6): p. 1541-53.
54. Rothenberg, L.N. and K.S. Pentlow, *Radiation dose in CT.* Radiographics, 1992. **12**(6): p. 1225-43.
55. Wolbarst, A.B., *Physics of Radiology*. 1993, Norwalk Appleton & Lange.
56. Izewska, J. and G. Rajan, *Radiation Dosimeters*, in *Radiation Oncology Physics: A Handbook for Teachers and Students*, E.B. Podgorsak, Editor. 2005, International Atomic Energy Agency: Austria. p. 71-99.
57. Brady, S., et al., *Implementation of radiochromic film dosimetry protocol for volumetric dose assessments to various organs during diagnostic CT procedures.* Med Phys, 2010. **37**(9): p. 4782-92.
58. Brady, S.L. and R.A. Kaufman, *Establishing a standard calibration methodology for MOSFET detectors in computed tomography dosimetry.* Med Phys, 2012. **39**(6): p. 3031-40.
59. Gladstone, D.J. and L.M. Chin, *Automated data collection and analysis system for MOSFET radiation detectors.* Med Phys, 1991. **18**(3): p. 542-8.
60. Ramani, R., S. Russell, and P. O'Brien, *Clinical dosimetry using MOSFETs.* Int J Radiat Oncol Biol Phys, 1997. **37**(4): p. 959-64.
61. Peet, D.J. and M.D. Pryor, *Evaluation of a MOSFET radiation sensor for the measurement of entrance surface dose in diagnostic radiology.* Br J Radiol, 1999. **72**(858): p. 562-8.
62. Dong, S.L., et al., *Characterization of high-sensitivity metal oxide semiconductor field effect transistor dosimeters system and LiF:Mg,Cu,P thermoluminescence dosimeters for use in diagnostic radiology.* Appl Radiat Isot, 2002. **57**(6): p. 883-91.

63. Yoshizumi, T.T., et al., *Validation of metal oxide semiconductor field effect transistor technology for organ dose assessment during CT: comparison with thermoluminescent dosimetry.* AJR Am J Roentgenol, 2007. **188**(5): p. 1332-6.
64. Saltybaeva, N., et al., *Estimates of effective dose for CT scans of the lower extremities.* Radiology, 2014. **273**(1): p. 153-9.
65. Gerber, T.C., R.S. Kuzo, and R.L. Morin, *Techniques and parameters for estimating radiation exposure and dose in cardiac computed tomography.* Int J Cardiovasc Imaging, 2005. **21**(1): p. 165-76.
66. Morin, R.L., T.C. Gerber, and C.H. McCollough, *Radiation dose in computed tomography of the heart.* Circulation, 2003. **107**(6): p. 917-22.
67. van Straten, M., et al., *The effect of angular and longitudinal tube current modulations on the estimation of organ and effective doses in x-ray computed tomography.* Med Phys, 2009. **36**(11): p. 4881-9.
68. Khursheed, A., et al., *Influence of patient age on normalized effective doses calculated for CT examinations.* Br J Radiol, 2002. **75**(898): p. 819-30.
69. Koblinger, L. and P. Zarand, *Monte Carlo calculations on chest X-ray examinations for the determination of the absorbed dose and image quality.* Phys Med Biol, 1973. **18**(4): p. 518-31.
70. Deak, P., et al., *Validation of a Monte Carlo tool for patient-specific dose simulations in multi-slice computed tomography.* Eur Radiol, 2008. **18**(4): p. 759-72.
71. DeMarco, J.J., et al., *A Monte Carlo based method to estimate radiation dose from multidetector CT (MDCT): cylindrical and anthropomorphic phantoms.* Phys Med Biol, 2005. **50**(17): p. 3989-4004.
72. Deak, P.D., Y. Smal, and W.A. Kalender, *Multisection CT protocols: sex- and age-specific conversion factors used to determine effective dose from dose-length product.* Radiology, 2010. **257**(1): p. 158-66.
73. Schmidt, B. and W.A. Kalender, *A fast voxel-based Monte Carlo method for scanner- and patient-specific dose calculations in computed tomography.* Physica Medica, 2002. **18**(2): p. 43-53.
74. Li, X., et al., *Patient-specific radiation dose and cancer risk estimation in CT: part II. Application to patients.* Med Phys, 2011. **38**(1): p. 408-19.
75. Lee, C., et al., *Organ doses for reference pediatric and adolescent patients undergoing computed tomography estimated by Monte Carlo simulation.* Med Phys, 2012. **39**(4): p. 2129-46.
76. Christner, J.A., J.M. Kofler, and C.H. McCollough, *Estimating effective dose for CT using dose-length product compared with using organ doses: consequences of adopting International Commission on Radiological Protection publication 103 or dual-energy scanning.* AJR Am J Roentgenol, 2010. **194**(4): p. 881-9.
77. Hall, E.J. and D.J. Brenner, *Cancer risks from diagnostic radiology.* Br J Radiol, 2008. **81**(965): p. 362-78.
78. Turner, A.C., et al., *The feasibility of a scanner-independent technique to estimate organ dose from MDCT scans: using CTDIvol to account for differences between scanners.* Med Phys, 2010. **37**(4): p. 1816-25.
79. Huda, W., K.M. Ogden, and M.R. Khorasani, *Converting dose-length product to effective dose at CT.* Radiology, 2008. **248**(3): p. 995-1003.
80. Zhang, Y., et al., *Organ doses, effective doses, and risk indices in adult CT: comparison of four types of reference phantoms across different examination protocols.* Med Phys, 2012. **39**(6): p. 3404-23.

81. DeMarco, J.J., et al., *Estimating radiation doses from multidetector CT using Monte Carlo simulations: effects of different size voxelized patient models on magnitudes of organ and effective dose.* Phys Med Biol, 2007. **52**(9): p. 2583-97.
82. Geleijns, J., et al., *Comparison of two methods for assessing patient dose from computed tomography.* Br J Radiol, 1994. **67**(796): p. 360-5.
83. Huda, W., D. Magill, and W. He, *CT effective dose per dose length product using ICRP 103 weighting factors.* Med Phys, 2011. **38**(3): p. 1261-5.
84. ICRU, *Tissue Substitutes in Radiation Dosimetry and Measurement*. 1989, International Commission on Radiation Units and Measurements: Bethesda, MD.
85. Schneider, S.M., J.P. Schlomka, and G.L. Harding, *Coherent-Scatter Computed Tomography Applying a Fan-Beam Geometry* Proc. SPIE Medical Imaging, 2001. **4320**: p. 754-763.
86. Zaidi, H. and M.R. Ay, *Current status and new horizons in Monte Carlo simulation of X-ray CT scanners.* Med Biol Eng Comput, 2007. **45**(9): p. 809-17.
87. Jones, D.G. and P.C. Shrimpton, *Normalised organ doses for X-ray computed tomography using Monte Carlo techniques*, in *Document NRPB-SR250*. 1993, National Radiological Protection Board: Chilton, UK.
88. Geleijns, J., et al., *Radiation exposure to patients in a multicenter coronary angiography trial (CORE 64).* AJR Am J Roentgenol, 2011. **196**(5): p. 1126-32.
89. Kalender, W.A., et al., *Generating and using patient-specific whole-body models for organ dose estimates in CT with increased accuracy: Feasibility and validation.* Phys Med, 2014.
90. Goetti, R., et al., *Radiation doses from phantom measurements at high-pitch dual-source computed tomography coronary angiography.* Eur J Radiol, 2012. **81**(4): p. 773-9.
91. Kim, S., et al., *Estimation of absorbed doses from paediatric cone-beam CT scans: MOSFET measurements and Monte Carlo simulations.* Radiat Prot Dosimetry, 2010. **138**(3): p. 257-63.
92. *National Council on Radiation Protection and Measurements. Ionizing Radiation Exposure of the Population of the United States. Report No. 160.*, in *Report No. 160*. 2009, National Council on Radiation Protection and Measurements: Bethesda, MD.
93. Smith-Bindman, R., et al., *Radiation dose associated with common computed tomography examinations and the associated lifetime attributable risk of cancer.* Arch Intern Med, 2009. **169**(22): p. 2078-86.
94. Perisinakis, K., A. Tzedakis, and J. Damilakis, *On the use of Monte Carlo-derived dosimetric data in the estimation of patient dose from CT examinations.* Med Phys, 2008. **35**(5): p. 2018-28.
95. Zankl, M. and A. Wittmann, *The adult male voxel model "Golem" segmented from whole-body CT patient data.* Radiat Environ Biophys, 2001. **40**(2): p. 153-62.
96. Ding, A., et al., *Extension of RPI-adult male and female computational phantoms to obese patients and a Monte Carlo study of the effect on CT imaging dose.* Phys Med Biol, 2012. **57**(9): p. 2441-59.
97. CT-Dose. http://www.radiation-dose.com/. [cited.
98. ImPACT. http://www.impactscan.org/. [cited.
99. Stamm, G. and H.D. Nagel, *[CT-expo--a novel program for dose evaluation in CT].* Rofo, 2002. **174**(12): p. 1570-6.
100. Li, X., et al., *Patient-specific dose estimation for pediatric chest CT.* Med Phys, 2008. **35**(12): p. 5821-8.

101. *European Commission.European guidelines on quality criteria for computed tomography*. 1999: Brussels, Belgium.
102. *1990 Recommendations of the International Commission on Radiological Protection.* Ann ICRP, 1991. **21**(1-3): p. 1-201.
103. *The 2007 Recommendations of the International Commission on Radiological Protection. ICRP publication 103.* Ann ICRP, 2007. **37**(2-4): p. 1-332.
104. Li, X., et al., *Effects of protocol and obesity on dose conversion factors in adult body CT.* Med Phys, 2012. **39**(11): p. 6550-71.
105. Tian, X., et al., *Pediatric chest and abdominopelvic CT: organ dose estimation based on 42 patient models.* Radiology, 2014. **270**(2): p. 535-47.
106. Alonso, M., et al., *Monte Carlo estimation of absorbed dose to organs in computed tomography.* Health Phys, 2002. **82**(2): p. 233-9.
107. Castellano, I.A., D.R. Dance, and P.M. Evans, *CT dosimetry: getting the best from the adult Cristy phantom.* Radiat Prot Dosimetry, 2005. **114**(1-3): p. 321-5.
108. Jarry, G., et al., *A Monte Carlo-based method to estimate radiation dose from spiral CT: from phantom testing to patient-specific models.* Phys Med Biol, 2003. **48**(16): p. 2645-63.
109. Yanch, J.C., et al., *Increased radiation dose to overweight and obese patients from radiographic examinations.* Radiology, 2009. **252**(1): p. 128-39.
110. Angel, E., et al., *Monte Carlo simulations to assess the effects of tube current modulation on breast dose for multidetector CT.* Phys Med Biol, 2009. **54**(3): p. 497-512.
111. Lee, C., et al., *Hybrid computational phantoms of the male and female newborn patient: NURBS-based whole-body models.* Phys Med Biol, 2007. **52**(12): p. 3309-33.
112. Lee, C., J.L. Williams, and W.E. Bolch, *Whole-body voxel phantoms of paediatric patients--UF Series B.* Phys Med Biol, 2006. **51**(18): p. 4649-61.
113. Chen, W., et al., *Fast on-site Monte Carlo tool for dose calculations in CT applications.* Med Phys, 2012. **39**(6): p. 2985-96.
114. Pathe, C., et al., *The presence of iodinated contrast agents amplifies DNA radiation damage in computed tomography.* Contrast Media Mol Imaging, 2010. **6**(6): p. 507-13.
115. Keegan, J., et al., *Radiation dose metrics in CT: assessing dose using the National Quality Forum CT patient safety measure.* J Am Coll Radiol, 2014. **11**(3): p. 309-15.
116. Costello, J.E., et al., *CT radiation dose: current controversies and dose reduction strategies.* AJR Am J Roentgenol, 2013. **201**(6): p. 1283-90.

APPENDIX 1: Methods for CT Effective Dose Estimation in Adult and Pediatric Populations

A1.1 Introduction

Rising concerns about the risks of radiation exposure from computed tomography (CT) examinations (1) have motivated numerous federal agencies and accrediting bodies in the U.S. to suggest improvements in monitoring, recording and reporting of radiation dose on a patient level. The federal government requires accreditation of non-hospital facilities that provide medical imaging services to meet standards to participate in Medicare (2, 3). The US Food and Drug Administration (FDA) and American College of Radiology (ACR) assure these facilities are in compliance (2, 3). As the FDA monitors and informs CT manufacturers of their statutory duty to report adverse events related to CT scanning, they are also working with the International Commission on Radiological Protection (ICRP) to incorporate radiation protection principles into facility quality assurance. The International Atomic Energy Agency (IAEA), developed and initiated a Smartcard to track a patient's cumulative radiation exposure for individual procedures (4).

CT scanner manufacturers currently provide measures of scanner radiation output for each CT scan performed. Since patient dose depends on both scanner output and patient size, the adjustment of the scanner reported output on the basis of patient size has been proposed (5).

The stochastic risk from the radiation dose received is also patient-dependent and varies according to the distribution of dose to an individual's radiosensitive organs and patient age. The dose descriptor most commonly used to communicate radiation risk from a specific CT protocol is the effective dose (E). However, current methods for estimating E are patient-generic and appropriate only for population-level dosimetry because these methods do not account for age or overall body size and individual organ doses. This paper aims to discuss current methods for estimating E and a novel, more patient-specific method that accounts for patient-size and the radio-sensitivity of irradiated organs.

A1.2 Measurement of Radiation Output with Physical Phantoms

Physical phantoms are used to measure the radiation output from a CT scan. The volume computed tomography dose index ($CTDI_{vol}$) expressed in units of milligray (mGy) and the dose-length product (DLP) expressed in units of mGy x centimeter (cm) are determined for each CT scan based on scanning a cylindrical polymethyl methacrylate (PMMA) phantom. $CTDI_{vol}$ represents the average amount of radiation imparted to a defined volume (cross-section) of a CTDI phantom and provides a measure of scanner radiation output (6). $CTDI_{vol}$ values are obtained for different combinations of dose-impacting scan parameters (e.g., tube potential, tube current, gantry rotation time, detector configuration, pitch, beam filter) by scanning either a standard 32-cm or 16-cm CTDI phantom. The results are used to fill lookup tables for adult body protocols (32-cm phantom), adult head protocols (16-cm phantom), and pediatric protocols (16-cm phantom). For a given protocol, the appropriate look-up table is referenced and the $\mathrm{CTDI}_{\mathrm{vol}}$ corresponding to the programmed scan parameters is displayed. $\mathrm{CTDI}_{\mathrm{vol}}$ values are not intended to quantify patient dose but rather provide radiation output for a given scan protocol.

The DLP accounts for the scan length and represents the total amount of ionizing radiation imparted to a reference phantom during a single CT scan and is obtained by multiplying the $\mathrm{CTDI}_{\mathrm{vol}}$ and the irradiated scan length. Although the scan length is determined by a given patient’s anatomy, the DLP, like the $\mathrm{CTDI}_{\mathrm{vol}}$, still describes radiation dose to a phantom, not a patient, and is not intended to quantify patient dose (6).

The dose absorbed by standard CTDI phantoms is known to underestimate dose to patients smaller than the phantoms and overestimate dose to patients larger than the phantoms. Absorbed dose from standard CTDI phantoms leads to 40-70% underestimation of dose for smaller adults and pediatric patients (7-9) whose bodies are smaller than the phantoms and provide less insulating tissue to shield highly radiosensitive organs from x-rays (7, 8). Brady and Kaufman observed that $\mathrm{CTDI}_{\mathrm{vol}}$ values from a 32-cm diameter phantom was a good surrogate for absorbed dose for patients weighing 113 kg but would lead to 29-66% underestimation of dose in patients weighing between 36 and 100 kg (7). Kalendar et al predicted dose would be overestimated for larger patients by $\mathrm{CTDI}_{\mathrm{vol}}$ values measured with a 32-cm diameter phantom (10).

A dose quantity was proposed by the American Association of Physicists in Medicine (AAPM) that adjusts the scanner-reported $\mathrm{CTDI}_{\mathrm{vol}}$ according to patient-size. The AAPM suggests multiplying size-based correction factors determined from lateral (LAT) and anterior-posterior (AP) measurements from patient images with the $\mathrm{CTDI}_{\mathrm{vol}}$ to calculate a size-specific dose estimate (SSDE) expressed in units of mGy (5). The SSDE then effectively provides information about the amount of radiation absorbed by a cross-section of a reference phantom similar in size to a given patient.

A1.3 Simulation of Radiation Dose in Computational Phantoms

Monte Carlo (MC) methods simulate the transport of ionizing radiation through the body and the absorption of radiation energy during a variety of situations ranging from space travel to medical imaging by modeling every step in the radiation exposure process. Monte Carlo methods are applied to computational phantoms and used to simulate the radiation dose a patient would theoretically receive from a CT scan. The entire imaging chain is modeled including the generation of x-rays, modification of x-rays through processes such as beam shaping and filtering, and the propagation of x-ray photons through the body. Monte Carlo code incorporates Poisson statistics to track individual x-ray photon histories. Random distances which a photon travels between interactions such as from a source through a medium (e.g., skin) to the detector are generated (11, 12). The random interactions of the photons are assigned probability functions of the mass attenuation coefficients (13), and used to generate a statistically large number of particle histories (11, 12). This makes it possible to predict properties of the radiation field such as the particle fluence, energy deposition, and energy spectrum at particular points (11, 12). The absorption of radiation energy within the body can be estimated but typically only reflects direct primary exposure of organs to x-rays from a CT scanner. Monte Carlo simulations have been validated against actual measurement of organ doses during scanning of physical phantoms (CTDI, anthropomorphic, and computational) (13-19)**.**

Monte Carlo methods have been applied to computational phantoms including mathematical (stylized), voxel (tomographic), and hybrid phantoms used to represent actual patients for dose estimation. The greatest sources of error stem from the design of the computational dosimetry phantoms (Fig A1.1), specifically the shape and distribution of organs. Monte Carlo simulation data are typically based on a standardized mathematical model of a human body known as the reference man (20). The International Commission on Radiological Protection (ICRP) defines a reference man as a Caucasian man that is an inhabitant of Western Europe or North America weighing 70 kg with a height of 170 cm (20, 21). The dimensions were obtained in the 1970s and 80s (22). Mathematical phantoms (also called stylized) are inherently limited because these phantoms contain fixed geometric shapes (elliptical cylinders, spheres, and cones) characterized by three-dimensional surface equations to represent patient organs (22, 23). The first types of computational phantoms were developed in 1960s at the Oak Ridge National Laboratory (ORNL) for the Medical Internal Radiation Dosimetry (MIRD) Committee. This phantom was classified as a hermaphrodite adult. By the 1980s, a family of mathematical phantoms (newborn, 1-year, 5-year, 10- year, 15-year, and adult phantom) was developed at ORNL based on anthropological reference data of ICRP publication 23 (24). These mathematical phantoms are intended to represent entire populations (25). However, the use of a single reference model for a specific age group does not capture variations in human anatomy (26). Lee and colleagues reported organ dose errors up to 30% using Monte Carlo software to calculate absorbed dose when a mathematical reference (15-year old) phantom was used to represent overweight 15-year old patients (27). This error is expected to increase when the reference adult is used to represent overweight and obese adults. The errors in organ dose estimates are due to a significant amount of subcutaneous fat thickness observed in overweight and obese patients when compared to either a reference pediatric or adult phantom (27).

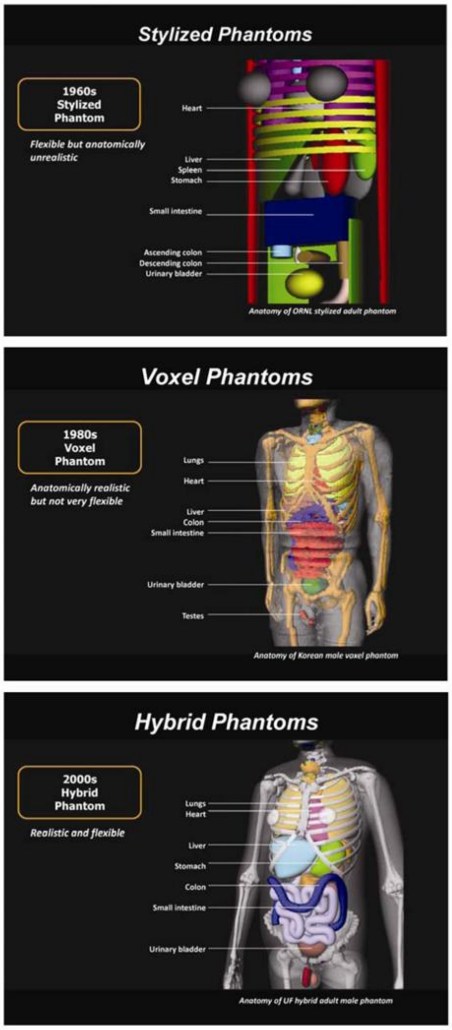

Stylized Phantoms

1960s Stylized Phantom

Flexible but anatomically unrealistic

Anatomy of ORNL stylized adult phantom

Voxel Phantoms

1980s Voxel Phantom

Anatomically realistic but not very flexible

Anatomy of Korean male voxel phantom

Hybrid Phantoms

2000s Hybrid Phantom

Realistic and flexible

Anatomy of UF hybrid adult male phantom

Figure A1.1: A comparison of computational phantoms: mathematical (stylized), voxel (tomographic), and hybrid phantoms (54). [permission granted for reprint]

Compared to mathematical phantoms, voxel (also called tomographic) models contain more realistic three-dimensional digital representations of the shape, volume, and composition of human organs (22, 28). Voxel models typically rely on either CT or magnetic resonance images from live volunteers or cadavers to provide three-dimensional representations of the human body (22, 29). Voxels dimensions are then scaled to match the body height and weight of the reference male. An improved approach is the creation of a voxelized phantom from a patient's own CT images. A patient's CT dataset can be voxelated by classifing each voxel as a particular tissue type based on fixed Hounsfield unit (HU) values (e.g, adipose tissue (-200 to -5 HU)) (30). Voxels are then assigned a molecular formula and a mass density estimate based on tissue type (30) (Fig A1.2).

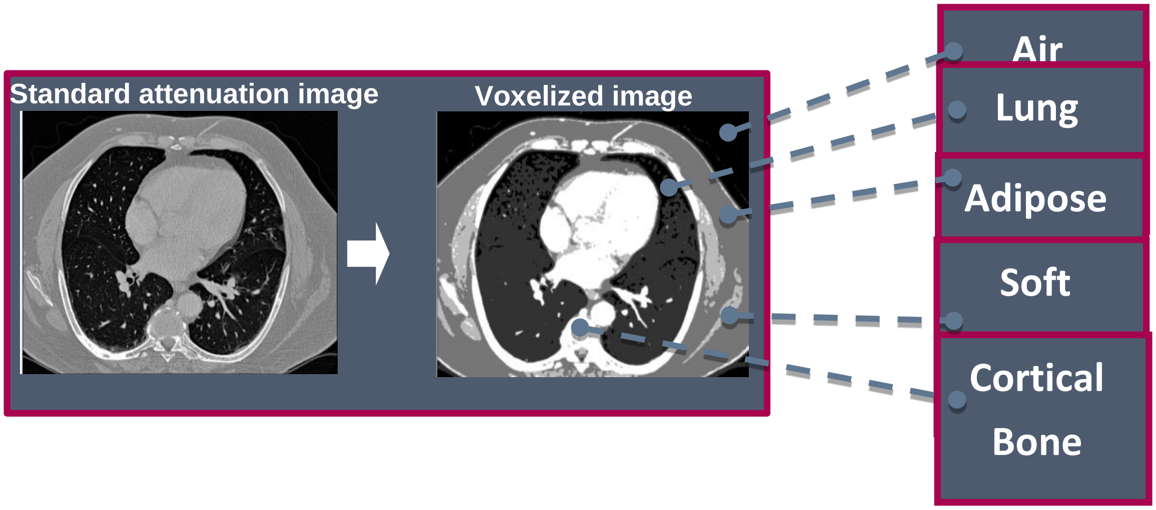

Figure A1.2: Creation of a patient-specific virtual phantom from a standard attenuation image. Each voxel is classified as a particular material type based on fixed Hounsfield unit (HU) values: air (-1000 to -930 HU), lung (-930 to -200 HU), adipose tissue (-200 to

-5 HU), water (-5 to -5 HU**)**, soft tissue (+5 to +40 HU), skeletal muscle (+40 to + 400 HU), cortical bone (> +400 HU) (30).

The most recent computational phantoms (hybrid) capture the advantages of both mathematical and voxel phantoms. Advanced mathematical descriptors, nonuniform rational B-spline (NURBS) and polygon mesh surfaces are used to characterize the boundaries of internal organs and exterior body surfaces along with the patient's segmented CT images (27, 31-35). These images are enhanced with the corresponding body dimensions and organ masses from the international reference data in ICRP 89 (31, 34, 36).

A1.4 Estimation of Effective Dose

A1.4.1 DLP conversion

The European Working Group for Guidelines on Quality Criteria in CT suggested a simple method for the estimation of effective dose: multiplication of the scanner-provided DLP, described above, with a standard body-region specific conversion factor (k-factor with units of mSv x mGy^{-1} x cm^{-1}) (37). The group published six k-factors representing broad regions of the human body (head and neck, head, neck, chest, abdomen and pelvis, trunk) at five phantom ages (0 year, 1 year, 5 years, 10 years, and adult). K-factors were derived from the family of mathematical phantoms using Monte Carlo methods as described in the ICRP 60 report (38-40). Data was averaged from MC simulations of scanning on many different single-slice scanner makes and models (41).

K-factors are limited because they fail to account for patient gender, age, body habitus, tissue composition, organ size or shape, nor specific scanner dosimetry, all known factors influencing the biological effect of radiation exposure.

A1.5 Monte Carlo Simulation using Reference Phantoms

More sophisticated approaches for the estimation of effective dose require CT dose estimation tools such as ImPACT patient dosimetry calculator (42-44) , CT-Expo (42, 45), and ImpactDose (42, 46) which apply MC techniques to reference phantoms (26). Absorbed doses in each organ and tissue are obtained by summing all energy depositions from primary and scattered photons in a given organ/tissue and dividing by the organ/tissue mass. In 1991, two comprehensive organ dose databases were developed; National Radiological Protection Board (NRPB) in London and National Research Center for Environment and Health (GSF) in Germany based on Monte Carlo simulations that exist in accordance to reference dimensions of the body and organs defined by the ICRP (31, 32). The NRPB organ dose database was originally based on a hermaphrodite adult stylized phantom and the National Research Center for Environment and Health (GSF) in Germany was based on male and female adult stylized phantoms (ADAM and EVA) as well as two pediatric (8 week old classified as BABY and a 7 year old classified as CHILD) voxel phantoms. ADAM and EVA, a modification of the hermaphrodite MIRD phantoms were an updated version of the original stylized phantoms developed at the ORNL in the 1960s. New MC simulations were performed on a few scanner models (Siemens DRH, GE 9800, and Philips LX) at NRPB for a complete family of six MIRD mathematical phantoms: a newborn, 1year, 5 years, 10 years, 15 years, and an adult (11) (Table A1.1). Meanwhile at GSF, a complete voxel family was also developed representing a range of patient sizes and ages from 8 weeks to 48 years of age including both male and female models (47) (Table A1.1). So, both databases have been updated to include both adult and pediatric phantoms.

Oak Ridge National Laboratory (ORNL)/ National Radiological Protection Board (NRPB) Mathematical Reference Phantoms				
Name	Gender	Age	Scanned Region	Weight
Newborn	hermaphrodite	Newborn	NA	3.5 kg
1 year		1 year	NA	9.9 kg
5 years		5 years	NA	18.5 kg
10 years		10 years	NA	32.5 kg
15 years		15 years	NA	55 kg
Adult		Adult	NA	70 kg
National Research Center for Environment and Health (GSF) Voxel Reference Phantoms				
Name	Gender	Age	Scanned Region	Weight
Baby	F	8 weeks	Whole body	4.2 kg
Child	F	7 years	Whole body	21.7 kg
Donna	F	40 years	Whole body	79 kg
Helga	F	26 years	Mid thigh and upwards	76.8 kg
Frank	M	48	Torso and head	65.4 kg
Golem	M	38	Whole body	68.9 kg
Visible Human	M	38	From knees and upwards	87.8 kg

Table A1.1: A complete family of mathematical reference phantoms and voxel reference phantoms that is used by the Oak Ridge National Laboratory (ORNL), National Radiological Protection Board (NRPB), and the National Research Center for Environment and Health (GSF) (8, 55, 56)

ImPACT uses 23 dosimetry datasets from 27 scanner models from the 1990s which are contained in the NRPB SR250 report (35, 40, 48). Modern scanners are matched according to dosimetry characteristics to one of the available datasets. CT-Expo and ImpactDose calculators incorporate most modern CT scanners (32, 35, 49, 50). Using scanner-specific information, these programs allow the user to estimate organ doses and effective dose for a wide range of scanner and examination parameters (39).

When MC methods are applied to a reference phantom, absorbed dose estimates are least accurate for patients smaller (pediatric) or larger (overweight or obese adult) than the reference phantoms highlighting the need for phantoms more representative of these groups(27). In order to provide more accurate dose estimates, overall patient size (51) and individual organ sizes should be considered or correction factors should be applied when scanning patients who deviate from the 70 kg reference phantom size or standard pediatric phantoms (42).

A1.6 Monte Carlo Simulation Using Patient Phantoms

Monte Carlo methods can be performed on voxelized image sets to produce patient-specific dose maps which assign each display a pixel value representing the absorbed dose of the corresponding tissue voxels. Monte Carlo simulation tools (Diagnostic Photon Simulation [DiPhos], Philips Research, Eindhoven, Netherlands and ImpactMC; CT Imaging, Erlangen, Germany) typically allow modeling of the specific scanner characteristics (e.g., CT scanner geometry, table geometry, beam collimation, bow-tie filter composition) used to obtain the images.

Dose to organs contained within the scan range are determined by segmenting the organ in the dose maps and summing over all pixel values contained within that organ (Fig A1.3). The total absorbed organ dose is multiplied with the appropriate tissue weighting factor defined by the ICRP (52, 53) to obtain an equivalent dose. Equivalent doses for all organs are summed to estimate effective dose. Effective dose calculated from the dose map method highlights the limitations inherent in the standard DLP method.

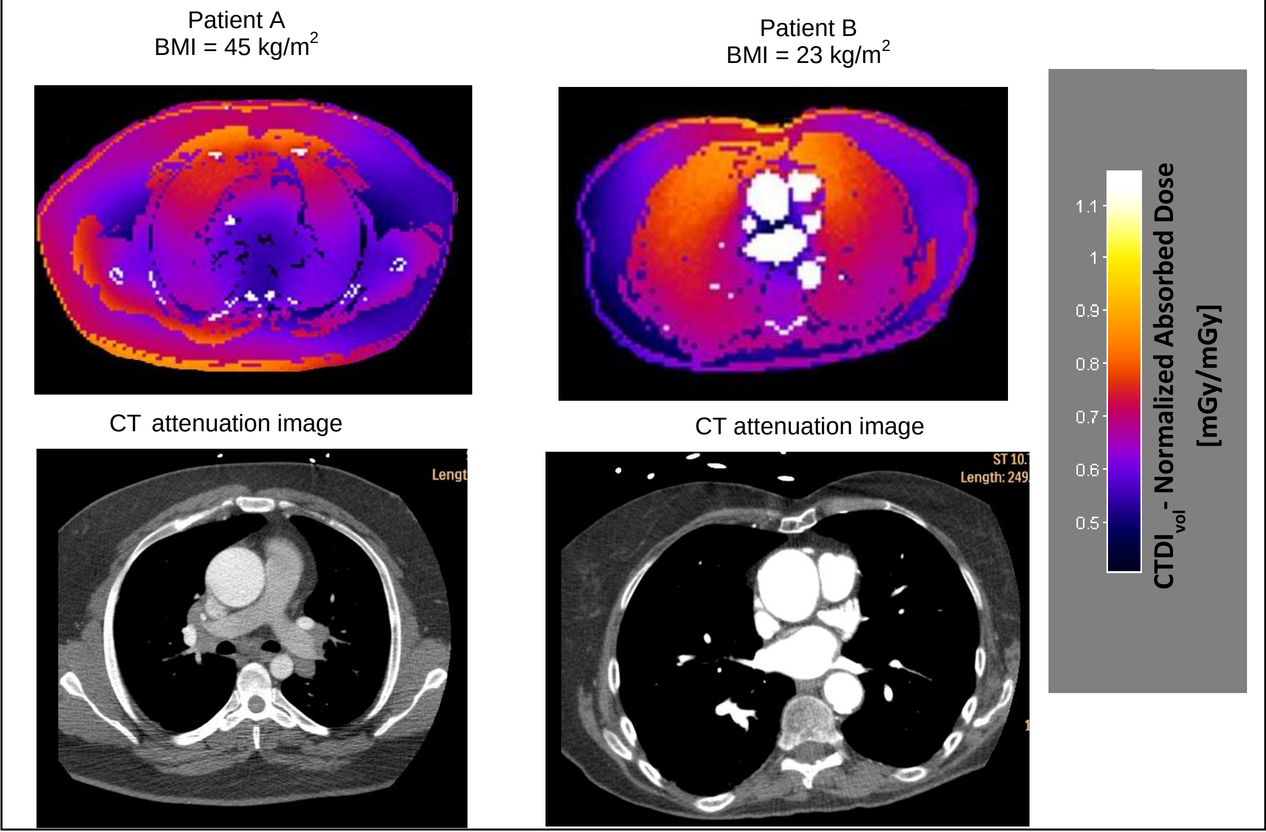

Figure A1.3: An example of axial CT attenuation images (bottom images) and the corresponding dose maps (top images) from two different patients for evaluation of thoracic aorta. Patient A (Male) with a BMI of 45 kg/m^2 was imaged with a prospective electrocardiogram-triggered axial technique at a tube potential of 120kVp. Patient B (Female) with a BMI of 23 kg/m^2 was imaged with a prospective electrocardiogram-triggered axial technique at a tube potential of 100 kV.

Unlike mathematical phantoms, voxelized patient phantoms contain all organs and tissues that are assigned a weighting factor by the ICRP. However, segmenting all the listed organs and tissues for each individual voxelized phantom is often impractical and typically effective dose is estimated by determining only dose to the most radiosensitive organs.

Appropriately accounting for dose to partially irradiated organs (organs that lie partly in and partly out of the reconstructed scan range) is challenging with voxelized phantoms based on patient images. Doses determined only from directly irradiated voxels contained within the scan range tend to overestimate dose to the partially irradiated organ because the weighting factor used to calculate equivalent dose assumes exposure to the entire organ. For partially irradiated organs, dose should be based on a weighted sum of dose to directly and indirectly irradiated regions. Dose to the indirectly irradiated region outside the scan range must be estimated based on assumptions about the total organ length and knowledge of dose falloff outside the prescribed scan range. Dose estimation to partially irradiated organs is not limited in this way with mathematical reference phantoms which represent the entire body (the cranial-caudal range is not limited to the reconstructed scan volume).

3D dose distribution maps created from patient images have the potential to account for variability (gender, body habitus, tissue composition, organ size, organ shape, specific scanner dosimetry) among patients not captured by reference phantoms and provide more patient-specific organ doses. However, estimation of effective dose requires multiplication with population based ICRP weighting factors. Still, estimation of effective dose from voxelized patient images is more patient- and scanner-specific in comparison to other methods used to compute effective dose

A1.7 Conclusion

Body size and patient specific anatomy are overlooked with the use of physical phantoms and mathematical phantoms. Mathematical phantoms cannot be used to calculate accurate organ doses because organs are characterized as geometric shapes. Organ doses are pertinent information to include in the calculation of effective dose. Effective doses based on a reference phantom are routinely used to describe the risk for a specific CT scan and to compare that risk to other CT scans or other sources of radiation exposure. Patient-specific dose maps are sensitive to scanner type, patient size, and organ size allowing estimation of organ and effective doses. Mathematical and voxels models that are based on reference man dimensions do not consider individuals who are smaller or larger than a 70 kg man. Whole body hybrid phantoms are advantageous for individuals that require a whole body CT or MRI scan but these models are scaled according to a various ICRP dimensions. Plus, modeling, segmentation is quite time consuming for hybrid phantoms. For individuals that required specific scanned region as in chest CT or chest, abdomen pelvis CT exams, patient-specific dose maps are ideal.

Use of more patient-specific methods to estimate organ and effective doses could lead to better metrics for CT dose management. Patient-specific organ doses can be estimated from patient image derived dose maps and used to determine more patient-specific effective dose values. However, any estimation of effective dose that uses population based ICRP weighting factors cannot be entirely patient-specific.

A1.8 References

1. Hess EP, Haas LR, Shah ND, Stroebel RJ, Denham CR, Swensen SJ. Trends in computed tomography utilization rates: a longitudinal practice-based study. J Patient Saf 2014; 10:52-58.
2. The Joint Commission Sentinel Event Alert: Radiation risks of diagnostic imaging;http://www.jointcommission.org/assets/1/18/SEA_47.pdf. 2011.
3. Harvey HB, Pandharipande PV. The federal government's oversight of CT safety: regulatory possibilities. Radiology 2012; 262:391-398.
4. Rehani MM, Frush DP, Berris T, Einstein AJ. Patient radiation exposure tracking: worldwide programs and needs--results from the first IAEA survey. Eur J Radiol 2012; 81:e968-976.
5. American Association of Physicists in Medicine. Size-Specific Dose Estimates (SSDE) in Pediatric and Adult Body CT Examinations (Task Group 204). In. College Park, MD: American Association of Physicists in Medicine, 2011.
6. Huda W, Sterzik A, Tipnis S, Schoepf UJ. Organ doses to adult patients for chest CT. Med Phys 2010; 37:842-847.
7. Brady SL, Kaufman RA. Investigation of American Association of Physicists in Medicine Report 204 size-specific dose estimates for pediatric CT implementation. Radiology 2012; 265:832-840.
8. Huda W, Vance A. Patient radiation doses from adult and pediatric CT. AJR Am J Roentgenol 2007; 188:540-546.
9. McCollough CH, Leng S, Yu L, Cody DD, Boone JM, McNitt-Gray MF. CT dose index and patient dose: they are not the same thing. Radiology 2011; 259:311-316.
10. Kalender WA. Dose in x-ray computed tomography. Phys Med Biol 2014; 59:R129-150.
11. Khursheed A, Hillier MC, Shrimpton PC, Wall BF. Influence of patient age on normalized effective doses calculated for CT examinations. Br J Radiol 2002; 75:819-830.
12. Koblinger L, Zarand P. Monte Carlo calculations on chest X-ray examinations for the determination of the absorbed dose and image quality. Phys Med Biol 1973; 18:518-531.
13. Deak P, van Straten M, Shrimpton PC, Zankl M, Kalender WA. Validation of a Monte Carlo tool for patient-specific dose simulations in multi-slice computed tomography. Eur Radiol 2008; 18:759-772.
14. Bostani M, McMillan K, DeMarco JJ, Cagnon CH, McNitt-Gray MF. Validation of a Monte Carlo model used for simulating tube current modulation in computed tomography over a wide range of phantom conditions/challenges. Med Phys 2014; 41:112101.
15. DeMarco JJ, Cagnon CH, Cody DD, et al. A Monte Carlo based method to estimate radiation dose from multidetector CT (MDCT): cylindrical and anthropomorphic phantoms. Phys Med Biol 2005; 50:3989-4004.

16. Jarry G, DeMarco JJ, Beifuss U, Cagnon CH, McNitt-Gray MF. A Monte Carlo-based method to estimate radiation dose from spiral CT: from phantom testing to patient-specific models. Phys Med Biol 2003; 48:2645-2663.
17. Kim S, Yoshizumi TT, Toncheva G, Frush DP, Yin FF. Estimation of absorbed doses from paediatric cone-beam CT scans: MOSFET measurements and Monte Carlo simulations. Radiat Prot Dosimetry 2010; 138:257-263.
18. Li X, Samei E, Segars WP, et al. Patient-specific radiation dose and cancer risk estimation in CT: part II. Application to patients. Med Phys 2011; 38:408-419.
19. Long DJ, Lee C, Tien C, et al. Monte Carlo simulations of adult and pediatric computed tomography exams: validation studies of organ doses with physical phantoms. Med Phys 2013; 40:013901.
20. Chapter 3 Physiological data for reference man. Annals of the ICRP/ICRP Publication 1975; 23:335-365.
21. ICRP. Basic anatomical and physiological data for use in radiological protection: reference values. A report of age- and gender-related differences in the anatomical and physiological characteristics of reference individuals. ICRP Publication 89. Ann ICRP 2002; 32:5-265.
22. Caon M. Voxel-based computational models of real human anatomy: a review. Radiat Environ Biophys 2004; 42:229-235.
23. Han EY, Bolch WE, Eckerman KF. Revisions to the ORNL Series of Adult and Pediatric Computational Phantoms for use with the MIRD Schema. Health Phys 2006; 90:337-356.
24. Lee C, Lee J. Computational anthropomorphic phantoms for radiation protection dosimetry: evolution and prospects. NET 2006; 38:239-250.
25. Zanki M. Methods for Assessing Organ Doses using Computational Models. Radiat Prot Dosimetry 1998; 80:207-212.
26. Castellano IA, Dance DR, Evans PM. CT dosimetry: getting the best from the adult Cristy phantom. Radiat Prot Dosimetry 2005; 114:321-325.
27. Lee C, Lodwick D, Williams JL, Bolch WE. Hybrid computational phantoms of the 15-year male and female adolescent: applications to CT organ dosimetry for patients of variable morphometry. Med Phys 2008; 35:2366-2382.
28. Zanki M. Computational Models Employed for Dose Assessment in Diagnostic Radiology. Radiat Prot Dosimetry 1993; 49:339-344.
29. Zankl M, Wittmann A. The adult male voxel model "Golem" segmented from whole-body CT patient data. Radiat Environ Biophys 2001; 40:153-162.
30. ICRU. Tissue Substitutes in Radiation Dosimetry and Measurement. In. Bethesda, MD: International Commission on Radiation Units and Measurements, 1989.
31. Kim KP, Berrington de Gonzalez A, Pearce MS, et al. Development of a database of organ doses for paediatric and young adult CT scans in the United Kingdom. Radiat Prot Dosimetry 2012; 150:415-426.
32. Lee C, Kim KP, Long D, et al. Organ doses for reference adult male and female undergoing computed tomography estimated by Monte Carlo simulations. Medical Physics 2011; 38:1196-1206.
33. Segars WP, Mahesh M, Beck TJ, Frey EC, Tsui BM. Realistic CT simulation using the 4D XCAT phantom. Med Phys 2008; 35:3800-3808.

34. Stabin MG, Xu XG, Emmons MA, Segars WP, Shi C, Fernald MJ. RADAR reference adult, pediatric, and pregnant female phantom series for internal and external dosimetry. J Nucl Med 2012; 53:1807-1813.
35. Zhang Y, Li X, Segars WP, Samei E. Organ doses, effective doses, and risk indices in adult CT: comparison of four types of reference phantoms across different examination protocols. Med Phys 2012; 39:3404-3423.
36. Lee C, Lodwick D, Hurtado J, Pafundi D, Williams JL, Bolch WE. The UF family of reference hybrid phantoms for computational radiation dosimetry. Phys Med Biol 2010; 55:339-363.
37. European Commission.European guidelines on quality criteria for computed tomography. In. Brussels, Belgium, 1999.
38. The Measurement, Reporting, and Managment of Radiation Dose in CT. Report of AAPM Task Group 23 of the Diagnostic Imaging Council CT Committee. Report No. 96. In. College Part, MD, 2008; 1-28.
39. McCollough CH, Christner JA, Kofler JM. How effective is effective dose as a predictor of radiation risk? AJR Am J Roentgenol 2010; 194:890-896.
40. Shrimpton PC. Assessment of Patient Dose in CT. Appendix C, European Guidelines for Multislice Computed Tomography. Funded by the European Commission; 2004. Contract No. FIGM-CT-2000-20078-CT-TIP. In, 2004.
41. Paul J, Banckwitz R, Krauss B, Vogl TJ, Maentele W, Bauer RW. Estimation and comparison of effective dose (E) in standard chest CT by organ dose measurements and dose-length-product methods and assessment of the influence of CT tube potential (energy dependency) on effective dose in a dual-source CT. Eur J Radiol 2012; 81:e507-512.
42. Huda W, Ogden KM, Khorasani MR. Converting dose-length product to effective dose at CT. Radiology 2008; 248:995-1003.
43. ImPACT. http://www.impactscan.org/. In.
44. Kalender WA, Saltybaeva N, Kolditz D, Hupfer M, Beister M, Schmidt B. Generating and using patient-specific whole-body models for organ dose estimates in CT with increased accuracy: Feasibility and validation. Phys Med 2014.
45. Stamm G, Nagel HD. [CT-expo--a novel program for dose evaluation in CT]. Rofo 2002; 174:1570-1576.
46. ImpactDose. http://www.ct-imaging.de/en/ct-software-e/impactdose-e.html.
47. DeMarco JJ, Cagnon CH, Cody DD, et al. Estimating radiation doses from multidetector CT using Monte Carlo simulations: effects of different size voxelized patient models on magnitudes of organ and effective dose. Phys Med Biol 2007; 52:2583-2597.
48. Huda W, Magill D, He W. CT effective dose per dose length product using ICRP 103 weighting factors. Med Phys 2011; 38:1261-1265.
49. Abdullah A, Sun Z, Pongnapang N, Ng KH. Comparison of computed tomography dose reporting software. Radiat Prot Dosimetry 2012; 151:153-157.
50. Lee E, Lamart S, Little MP, Lee C. Database of normalised computed tomography dose index for retrospective CT dosimetry. J Radiol Prot 2014; 34:363-388.

51. van Straten M, Deak P, Shrimpton PC, Kalender WA. The effect of angular and longitudinal tube current modulations on the estimation of organ and effective doses in x-ray computed tomography. Med Phys 2009; 36:4881-4889.
52. 1990 Recommendations of the International Commission on Radiological Protection. ICRP Publication 60. Ann ICRP 1991; 21:1-201.
53. The 2007 Recommendations of the International Commission on Radiological Protection. ICRP publication 103. Ann ICRP 2007; 37:1-332.
54. Bolch W, Lee C, Wayson M, Johnson P. Hybrid computational phantoms for medical dose reconstruction. Radiat Environ Biophys 2010; 49:155-168.
55. Lee C, Lee C, Staton RJ, et al. Organ and effective doses in pediatric patients undergoing helical multislice computed tomography examination. Med Phys 2007; 34:1858-1873.
56. Petoussi-Henss N, Zanki M, Fill U, Regulla D. The GSF family of voxel phantoms. Phys Med Biol 2002; 47:89-106.

APPENDIX 2: Presentations and publications resulting from dissertation work

- SS Halliburton, **CM Thompson**, SA Kuzmiak, J Wiegert, K Brown, TB Ivanc, ME Olszewski, JH Yanof, SD Flamm, P Schoenhagen, CT Dose Distribution Maps ("Dose Maps") in Cardiovascular CT Angiography: Patient-Specific Visualization of Absorbed Dose, Presented at the 6th Scientific Annual Meeting of the Society of Cardiovascular Computed Tomography, July 14-July 15, 2011, Denver, CO.

- DME Bardo, J Wiegert, DM Stevens, SS Halliburton, AC Dhanantwari, **CM Thompson**, P Ourednicek, D Pettersson, JH Yanof, Diagnostic CT Dose Distribution Maps Over a Range of Body Habitus & Dose Reduction Strategies: Patient-specific Visualization of Absorbed Dose in the Adult Population. Presented at the 97th Scientific Assembly and Annual Meeting of the Radiological Society of North America, November 27- December 2, 2011, Chicago, IL. **Cum Laude**.

- Schoenhagen P, **Thompson CM**, Halliburton SS. Low-Dose Cardiovascular Computed Tomography: Where are the Limits? Current Cardiology Reports. 2011

- **CM Thompson**, JH Yanof, J Wiegert, K Yaddanapudi, SS Halliburton, Patient-Specific Dose Maps for Cardiovascular CT Examinations: Estimating Variability in Normalized Breast and Lung Dose Among Patients. Presented at 7th Annual Meeting of the Society of Cardiovascular Computed Tomography, July 19-July 22, 2012, Baltimore, MD.

- **CM Thompson,** J Wiegert, SS Halliburton, JH Yanof. Comparison of Patient-Specific and Reference Methods for CT Dose Estimation in the Adult Population. Presented at the 97th Scientific Assembly and Annual Meeting of the Radiological Society of North America, November 25-November 30, 2012, Chicago, IL. **Cum Laude**.

- Estimating Effective Dose for Cardiac CT with Patient-Specific Dose Maps in Comparison with DLP Conversion ("k factor") Method

  Presented at European Congress of Radiology, March 7-11, 2013, Vienna, Austria

- Thompson CM, Yanof JH, Wiegert J, Bullen J, Obuchowski N, Yaddanapudi K, Halliburton SS. A pilot study of patient-specific Cardiovascular CT dose maps and their utility in estimating organ and effective doses in obese patients. J Cardiovascular Comput Tomogr., accepted, in revision

APPENDIX 3

Copyright Permission Letter for use of Figure 5.1

CIRS
Tissue Simulation & Phantom Technology

Monday, August 24, 2015

Carla Thompson

9500 Euclid Ave.

Cleveland, OH 44195

Dear Carla Thompson:

CIRS, Inc is pleased to grant you permission to reproduce images from our web page (http://www.cirsinc.com/products/modality/33/atom-dosimetry-verification-phantoms) in electronic and web formats for educational, non-profit use in your dissertation entitled “The Utility of Patient-Specific CT Dose Estimation Maps,” provided you give full credit to CIRS for use of the images.

This permission is a one-time, non-exclusive grant and is exclusively limited to the usage stated above.

We would kindly request that you send us a complimentary copy of your dissertation when available.

Sincerely,

Mark Devlin

President

COMPUTERIZED IMAGING REFERENCE SYSTEMS, INC.
2428 Almeda Avenue Suite 316 • Norfolk, Virginia 23513 • USA • Tel: (800) 617-1177 • (757) 855-2765 • Fax: (757) 857-0523
UL Registered Firm ISO 9001:2000 A4662 • www.cirsinc.com

APPENDIX 4

Copyright Permission for use of Figure 5.2

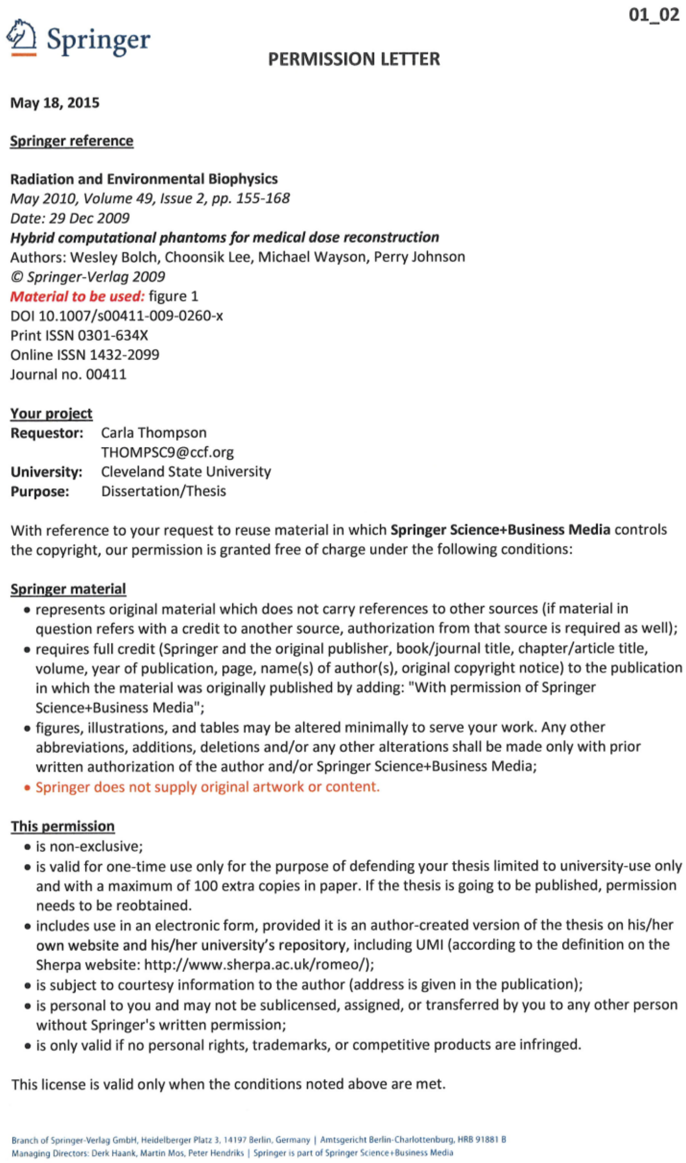

Springer

01_02

PERMISSION LETTER

May 18, 2015

Springer reference

Radiation and Environmental Biophysics
May 2010, Volume 49, Issue 2, pp. 155-168
Date: 29 Dec 2009
Hybrid computational phantoms for medical dose reconstruction
Authors: Wesley Bolch, Choonsik Lee, Michael Wayson, Perry Johnson
© Springer-Verlag 2009
Material to be used: figure 1
DOI 10.1007/s00411-009-0260-x
Print ISSN 0301-634X
Online ISSN 1432-2099
Journal no. 00411

Your project
Requestor: Carla Thompson
THOMPSC9@ccf.org
University: Cleveland State University
Purpose: Dissertation/Thesis

With reference to your request to reuse material in which **Springer Science+Business Media** controls the copyright, our permission is granted free of charge under the following conditions:

Springer material

- represents original material which does not carry references to other sources (if material in question refers with a credit to another source, authorization from that source is required as well);
- requires full credit (Springer and the original publisher, book/journal title, chapter/article title, volume, year of publication, page, name(s) of author(s), original copyright notice) to the publication in which the material was originally published by adding: "With permission of Springer Science+Business Media";
- figures, illustrations, and tables may be altered minimally to serve your work. Any other abbreviations, additions, deletions and/or any other alterations shall be made only with prior written authorization of the author and/or Springer Science+Business Media;
- Springer does not supply original artwork or content.

This permission

- is non-exclusive;
- is valid for one-time use only for the purpose of defending your thesis limited to university-use only and with a maximum of 100 extra copies in paper. If the thesis is going to be published, permission needs to be reobtained.
- includes use in an electronic form, provided it is an author-created version of the thesis on his/her own website and his/her university's repository, including UMI (according to the definition on the Sherpa website: http://www.sherpa.ac.uk/romeo/);
- is subject to courtesy information to the author (address is given in the publication);
- is personal to you and may not be sublicensed, assigned, or transferred by you to any other person without Springer's written permission;
- is only valid if no personal rights, trademarks, or competitive products are infringed.

This license is valid only when the conditions noted above are met.

Branch of Springer-Verlag GmbH, Heidelberger Platz 3, 14197 Berlin, Germany | Amtsgericht Berlin-Charlottenburg, HRB 91881 B
Managing Directors: Derk Haank, Martin Mos, Peter Hendriks | Springer is part of Springer Science+Business Media

APPENDIX 5

Copyright Permission Letter for use of Figure 8.1

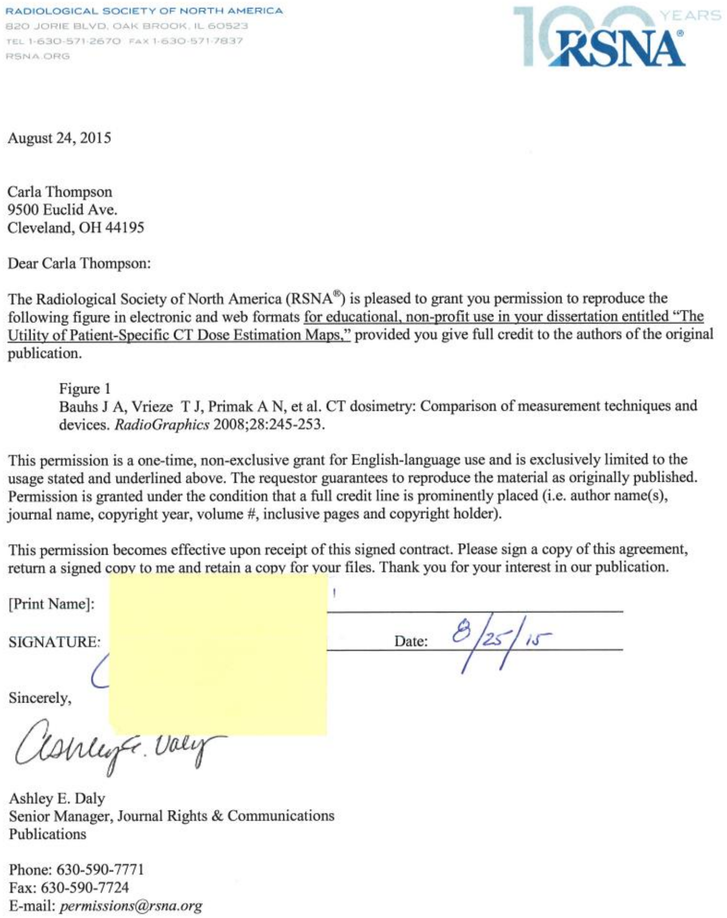

RADIOLOGICAL SOCIETY OF NORTH AMERICA
820 JORIE BLVD. OAK BROOK, IL 60523
TEL 1-630-571-2670 FAX 1-630-571-7837
RSNA.ORG

August 24, 2015

Carla Thompson
9500 Euclid Ave.
Cleveland, OH 44195

Dear Carla Thompson:

The Radiological Society of North America (RSNA$^{®}$) is pleased to grant you permission to reproduce the following figure in electronic and web formats for educational, non-profit use in your dissertation entitled "The Utility of Patient-Specific CT Dose Estimation Maps," provided you give full credit to the authors of the original publication.

> Figure 1
> Bauhs J A, Vrieze T J, Primak A N, et al. CT dosimetry: Comparison of measurement techniques and devices. *RadioGraphics* 2008;28:245-253.

This permission is a one-time, non-exclusive grant for English-language use and is exclusively limited to the usage stated and underlined above. The requestor guarantees to reproduce the material as originally published. Permission is granted under the condition that a full credit line is prominently placed (i.e. author name(s), journal name, copyright year, volume #, inclusive pages and copyright holder).

This permission becomes effective upon receipt of this signed contract. Please sign a copy of this agreement, return a signed copy to me and retain a copy for your files. Thank you for your interest in our publication.

[Print Name]: [redacted]

SIGNATURE: Date: 8/25/15

Sincerely,

Ashley E. Daly

Ashley E. Daly
Senior Manager, Journal Rights & Communications
Publications

Phone: 630-590-7771
Fax: 630-590-7724
E-mail: *permissions@rsna.org*